

Protein Electric Fields Enable Faster and Longer-Lasting Covalent Inhibition of β -Lactamases

Zhe Ji, Jacek Kozuch, Irimpan I. Mathews, Christian S. Diercks, Yasmin Shamsudin, Mirjam A. Schulz, and Steven G. Boxer*



Cite This: *J. Am. Chem. Soc.* 2022, 144, 20947–20954



Read Online

ACCESS |



Metrics & More

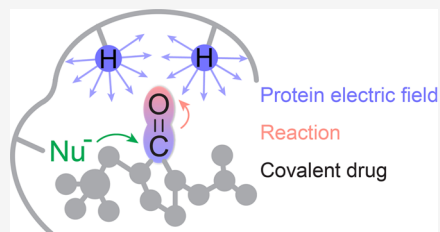


Article Recommendations



Supporting Information

ABSTRACT: The widespread design of covalent drugs has focused on crafting reactive groups of proper electrophilicity and positioning toward targeted amino-acid nucleophiles. We found that environmental electric fields projected onto a reactive chemical bond, an overlooked design element, play essential roles in the covalent inhibition of TEM-1 β -lactamase by avibactam. Using the vibrational Stark effect, the magnitudes of the electric fields that are exerted by TEM active sites onto avibactam's reactive C=O were measured and demonstrate an electrostatic gating effect that promotes bond formation yet relatively suppresses the reverse dissociation. These results suggest new principles of covalent drug design and off-target site prediction. Unlike shape and electrostatic complementarity which address binding constants, electrostatic catalysis drives reaction rates, essential for covalent inhibition, and deepens our understanding of chemical reactivity, selectivity, and stability in complex systems.



INTRODUCTION

The search for drugs that make covalent bonds to their targets has emerged as an important theme of drug discovery and development due to the advantages of increased potency and prolonged residence time.^{1–4} A typical covalent inhibitor bears an electrophilic warhead that, following specific binding to the target protein, is positioned to react rapidly with a proximal nucleophilic amino-acid residue, but minimally to off-target sites.^{5–7} Such selective reactivities are interpreted to be a combined consequence of using moderate electrophiles as the warhead, addressing protein residues that are highly nucleophilic and sterically accessible, and enforcing their proximity upon binding (Figure 1a).^{8,9} These design principles, based solely on intrinsic reactivity and atom locality, have limited power in predicting covalent inhibitors' potency of action. Given the same covalent inhibitor, what makes the bond formation fast at one site, yet slow or even futile at another? This question also cannot be simply answered by shape and electrostatic complementarity, which are widely used to optimize *binding constants* rather than *reactivity* (Figure 1b). Beyond discoveries from screening, a deeper understanding of covalent inhibition is missing.

We chose TEM-1 β -lactamase, a culprit of antibiotic resistance, as the model enzyme because it has been extensively studied as a target of covalent inhibition. TEM-1 β -lactamase rapidly hydrolyzes penicillin G (PenG), a β -lactam substrate, through a two-step mechanism.^{10,11} The hydroxy group of S70 attacks PenG's β -lactam carbonyl (C=O), generating an acyl-enzyme (Figure 2a), which is subsequently deacylated via hydrolysis for a catalytic turnover (Table S1). By contrast, a similar nucleophilic attack on the urea C=O of avibactam

(AVB) forms a carbamyl-enzyme stable to hydrolysis, thus trapping the enzyme in the covalent complex (Figure 2b).¹² The carbamylation is reversible through a slow recyclization reaction to reform the cyclic urea, making AVB a reversible covalent inhibitor.¹³ AVB has been identified as an effective covalent drug for targeting many serine β -lactamases,^{14,15} exhibiting desired kinetic parameters, including high rates of carbamylation (k_{cbm}) for fast action, low rates of recyclization (k_{rec}) for prolonged residence time, and small overall dissociation constants (K_i^*) for high affinity (Tables 1 and S2). We sought to find a unifying physical basis for the outstanding performance of AVB that may inform the design of covalent inhibitors in general.

The concept of electrostatic catalysis has been proposed¹⁶ and experimentally^{17–19} and computationally^{20,21} demonstrated to account for a substantial fraction of the remarkable proficiency of a number of enzymes. Different from externally applied electric fields in modulating reactivities,^{22–24} electric fields in enzyme active sites are exerted by the charges and dipoles organized by protein scaffolds and have been found to stabilize charge separation in transition states, thus lowering the free energy barrier (Figure 2c). To apply this concept beyond enzyme catalysis and use it to investigate covalent inhibition, we examined the electrostatic interactions in the

Received: September 15, 2022

Published: November 3, 2022



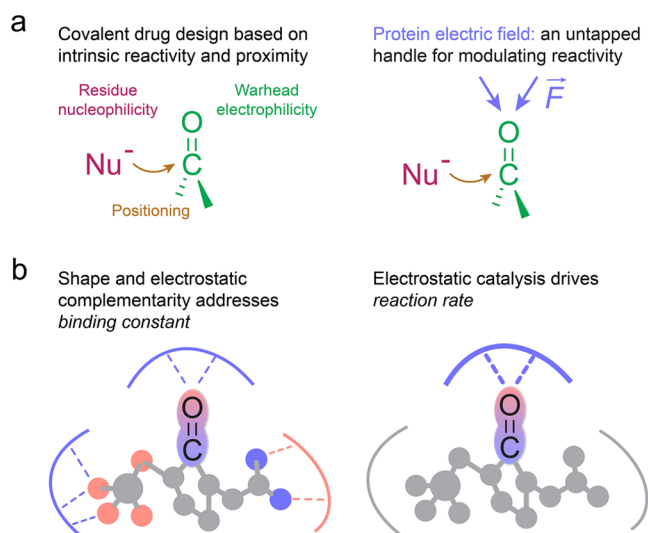


Figure 1. Electrostatic catalysis applied to covalent inhibition. (a) Common considerations for covalent drug design, using a carbonyl warhead as an example. This work presents a new design principle: the electric fields that are produced by protein dipoles and charged groups and act on chemical bonds undergoing reactions. (b) Shape and electrostatic complementarity in contrast to electrostatic catalysis. The former considers all of the protein–ligand interactions and thus largely determines K_M or K_i ; the latter focuses on the electric fields experienced by the reactive bond and therefore contributes to k_{cat} or k_{on} , as presented in this work.

TEM active sites for both the noncovalent complexes, denoted by TEM·PenG and TEM·AVB, and the covalent complex TEM–AVB (Figure 2a,b). The reactive C=O is engaged in two hydrogen bonds (H-bonds) with the backbone amides of A237 and S70. Such H-bonds are mostly electrostatic in nature and their effects can be energetically viewed as electric fields projected on the C=O.²⁵ For all three reactions: acylation, carbamylation, and recyclization, the C=O is transformed into oxyanion intermediates, whose preceding transition states experience charge separation with reaction difference dipoles, $\Delta\vec{\mu}_{rxn}$, along the C=O (Figure 2c). This dipole interacts with the electric fields imposed by the enzyme active site (\vec{F}) as $\Delta\Delta G^\ddagger = -\vec{F} \cdot \Delta\vec{\mu}_{rxn}$, where $\Delta\Delta G^\ddagger$ is the lowering of the free energy barrier.

Unlike enzymes where amino-acid side chains interact with the substrate and where site-directed mutagenesis is the standard method to probe enzyme/substrate interactions, amide backbone interactions are not readily modified. In this work, we perturbed the electrostatic interactions of the C=O by replacing the A237 backbone amide with a backbone ester (Figure 2d). The loss of the H-bond donor led to slower rates observed from kinetic studies (Table 1) and correspondingly lower magnitudes of electric fields measured using the vibrational Stark effect. This correlation allows us to quantify the contribution of the active site electric field, which enhances the rate of PenG acylation (k_{ac}) and AVB k_{cbm} by 8.6 and 7.5 orders of magnitude, respectively, making the bonding of the inhibitor almost as fast as that of the substrate. Avibactam, once bound, shifts its key carbonyl to a smaller-field environment, which relatively suppresses its dissociation, leading to a prolonged residence time from 13 s to 72 min and a decrease in K_i^* from 240 to 0.74 nM for tighter bonding. These large effects of electric fields provide an untapped handle for modulating the bonding potency of covalent

inhibitors and the residence time of reversible covalent inhibitors.

RESULTS

Removal of a Key H-Bond by Introducing a Backbone Ester.

We expressed TEM-1 (Table S3) and obtained crystal structures (Tables S4–S8) showing that the residue of A237 is largely solvent-exposed (Figure S1), suggesting the potential tolerance of the protein architecture to replacement of the methyl group with bulkier residues. The A237Y mutation yielded a similar protein structure overlapping well with that of the wild type (WT), except for the extra phenolic residue (Figure S2). Soaking TEM-1 crystals in AVB solutions resulted in TEM–AVB covalent complexes (Figure S3). The bound AVB forms a rich network of noncovalent interactions using its sulfate and amide groups (Figure S4) in addition to the two key H-bonds of the carbamate C=O (Figure 3a). The O–N distances between the C=O and the backbone amides of A237 and S70 are 2.98(12) and 2.69(12) Å, respectively (errors estimated using rearranged Cruickshank's formulae²⁶). The A237Y mutation preserves the conformation of AVB (Figures 3a and S5 and S6) with comparable O–N distances of 2.90(11) and 2.67(11) Å.

To replace the amide backbone of A237Y with an ester, we used amber suppression to site-specifically incorporate *p*-hydroxy-*L*-phenyllactic acid (HPLA) (Figure S7 and Table S9), a tyrosine analogue that bears the same phenolic residue but a hydroxy acid rather than an amino acid for making a backbone ester (Figure 3b).²⁷ The obtained ester protein (A237Y^e) shows a gain in mass by 1 Da captured by high-resolution mass spectrometry (MS), consistent with the extra mass carried by the O compared with the NH group in the original amide backbone (Figure 3b). The ester bond can be selectively hydrolyzed under alkaline conditions, generating two protein fragments of the expected masses (Figures 3b and S8), which confirms the position of the ester in the protein backbone. Their sum is larger than the mass of the intact ester protein by 18 Da, corresponding to the addition of water by hydrolysis. Although we did not obtain crystals of the A237Y^e mutant (Text S1 in the Supporting Information), ¹H NMR spectroscopy shows high similarity between the spectrum of A237Y and that of A237Y^e (Figure S9), including both the downfield amide/aromatic region (Figure S10) and the upfield aliphatic region (Figure S11). The consistent ¹H NMR fingerprints confirm that the ester protein adopts the same tertiary structure as the amide protein does.

Measurement of the Active-Site Electric Fields Experienced by the Reactive C=O in PenG and AVB.

To measure the electric fields at the active site, AVB's reactive C=O is not only a participant in the reactions but is also used as a vibrational (infrared) probe of the electric field it experiences.^{25,28,29} According to the linear vibrational Stark effect, vibrational frequencies shift in proportion to the magnitude of electric fields. The sensitivity of such frequency shifts to electric fields was determined by vibrational solvatochromism, molecular dynamics (MD) simulations, and vibrational Stark spectroscopy using molecular model compounds (Figures S12–S14 and Tables S10–S14). With the urea and the carbamate C=O probes calibrated, the readout of the vibrational frequency of the C=O can be mapped to the magnitude of electric fields projected onto the C=O for both TEM·AVB and TEM–AVB.

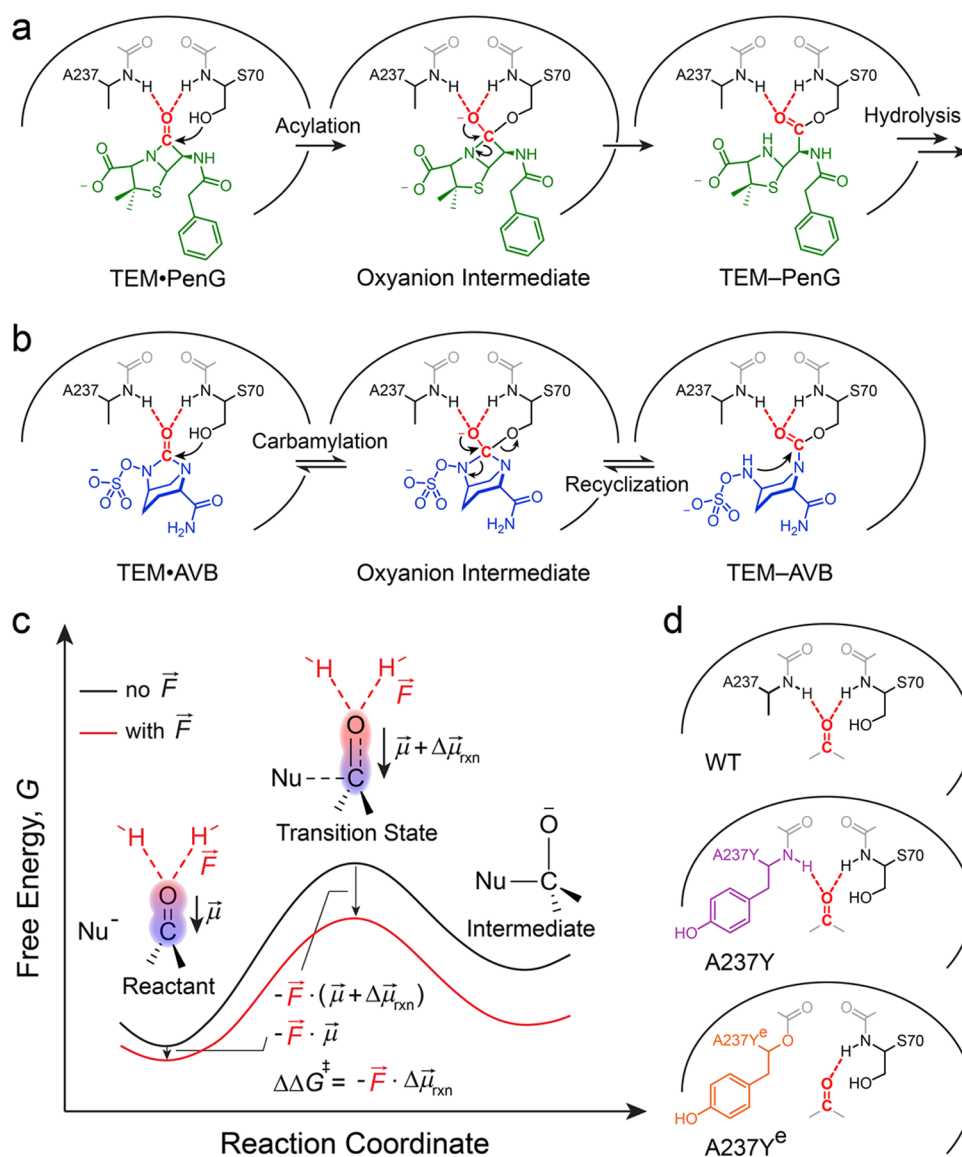


Figure 2. Reactions and key electrostatics in the active site of TEM β -lactamases. (a) Mechanism of acylation by PenG. The hydroxy residue of S70 acts as a nucleophile to attack PenG's β -lactam C=O, forming an oxyanion intermediate before turning into an acyl-enzyme complex, which is subject to hydrolysis (not shown). (b) Mechanism of covalent inhibition by AVB. A similar nucleophilic attack of AVB's urea C=O by S70 traps the enzyme in the carbamate complex without turnover. Recyclization, the reverse reaction of carbamylation, regenerates AVB, making it a reversible covalent inhibitor. Proton movement is omitted in the electron-pushing mechanism. (c) Model of electrostatic catalysis. The conversion of a C=O to an oxyanion intermediate passes through a transition state where charges are more separated between C and O atoms, generating a reaction difference dipole ($\Delta\vec{\mu}_{\text{rxn}}$), which interacts with the electric field in the enzyme active site \vec{F} to reduce the free energy barrier by $\Delta\Delta G^\ddagger$. (d) H-bond donated by the A237 backbone amide, a key contributor to the enzyme electric field in β -lactamases (and many other enzymes), can be perturbed by the A237Y mutation and even removed by replacing the amide with an ester in A237Y^e.

Samples of TEM•AVB for infrared spectroscopy were prepared by mixing AVB with TEM-S70G, a nucleophile-impaired mutant, which traps the noncovalent complex.¹¹ To extract the AVB C=O's vibrational peaks from the overwhelming protein background, we synthesized AVB with an isotope-labeled $^{13}\text{C}=\text{O}$ (Figures 3c and S15–S23), which displays the expected isotope redshift of 47 cm^{-1} with respect to $^{12}\text{C}=\text{O}$ (Figure S24 and Table S15). By subtracting the infrared absorption spectrum of TEM•AVB- ^{13}C from that of the unlabeled TEM•AVB, the protein background cancels out, leaving only $^{12}\text{C}=\text{O}$ peaks with positive intensities and the corresponding $^{13}\text{C}=\text{O}$ peaks with negative intensities (Figures 3d and S25 and Table S16). The observed peak multiplicity indicates that the vibration experiences a heterogeneous

electrostatic environment comprising a distribution of C=O orientations and H-bond lengths.¹¹ The electrostatic heterogeneity is also manifested in TEM–AVB samples (Figures 3e and S26 and Table S17). The ^{12}C – ^{13}C difference spectrum shows a peak envelope fitted to five pairs of positive–negative peaks (Text S2 in the Supporting Information). By contrast, the crystal structure of TEM–AVB shows only one conformation of AVB (Figures 3a and S27), whether measured at 100 K (1.72 Å) or room temperature (2.45 Å). Complete conformational sampling is rarely accessible from crystallography data (Figure S28),³⁰ but the associated local electrostatic effects can be sensitively probed by vibrational frequency shifts, and this is the likely origin of the multiple peaks we observe.

Table 1. Selected Kinetic Parameters for PenG Acylation and AVB Inhibition of TEM-1

	PenG acylation rate, k_{ac} (s ⁻¹) ^a	AVB carbamylation rate, k_{cbm} (s ⁻¹) ^b	AVB recyclization rate, k_{rec} (s ⁻¹) ^b
WT	4941 [4784, 5086]	23.1 ± 0.2	(2.3 ± 0.3) × 10 ⁻⁴
A237Y	2838 [2740, 2940]	6.19 ± 0.08	(1.7 ± 0.3) × 10 ⁻³
A237Y ^e (ester)	86.1 [69.2, 97.0]	(1.8 ± 0.1) × 10 ⁻³	(3.4 ± 0.1) × 10 ⁻⁷
A237E	5857 [5288, 6012]	4.63 ± 0.23	(8.7 ± 1.5) × 10 ⁻⁵
A237R	3265 [3137, 3396]	3.63 ± 0.03	(6.2 ± 0.9) × 10 ⁻⁴
A237W	1390 [1366, 1415]	3.31 ± 0.05	(6.7 ± 1.3) × 10 ⁻⁴

^a k_{ac} was derived from k_{cat} using steady-state mass spectrometry. k_{cat} was determined by fitting full-time kinetic data to the integrated Michaelis–Menten equation. Three independent repeats and a bootstrapping algorithm provided the medians with uncertainties at 68.25% confidence interval. See the Supporting Information for experimental details and full kinetic data (Figure S1). ^b k_{cbm} and k_{rec} were measured by inhibition experiments from which the rate of substrate turnover's initial value, final value, and decay rate were obtained. The errors were estimated based on the fitting results of 20–30 inhibition experiments with a series of AVB concentrations. See the Supporting Information for experimental details and full kinetic data (Figure S2).

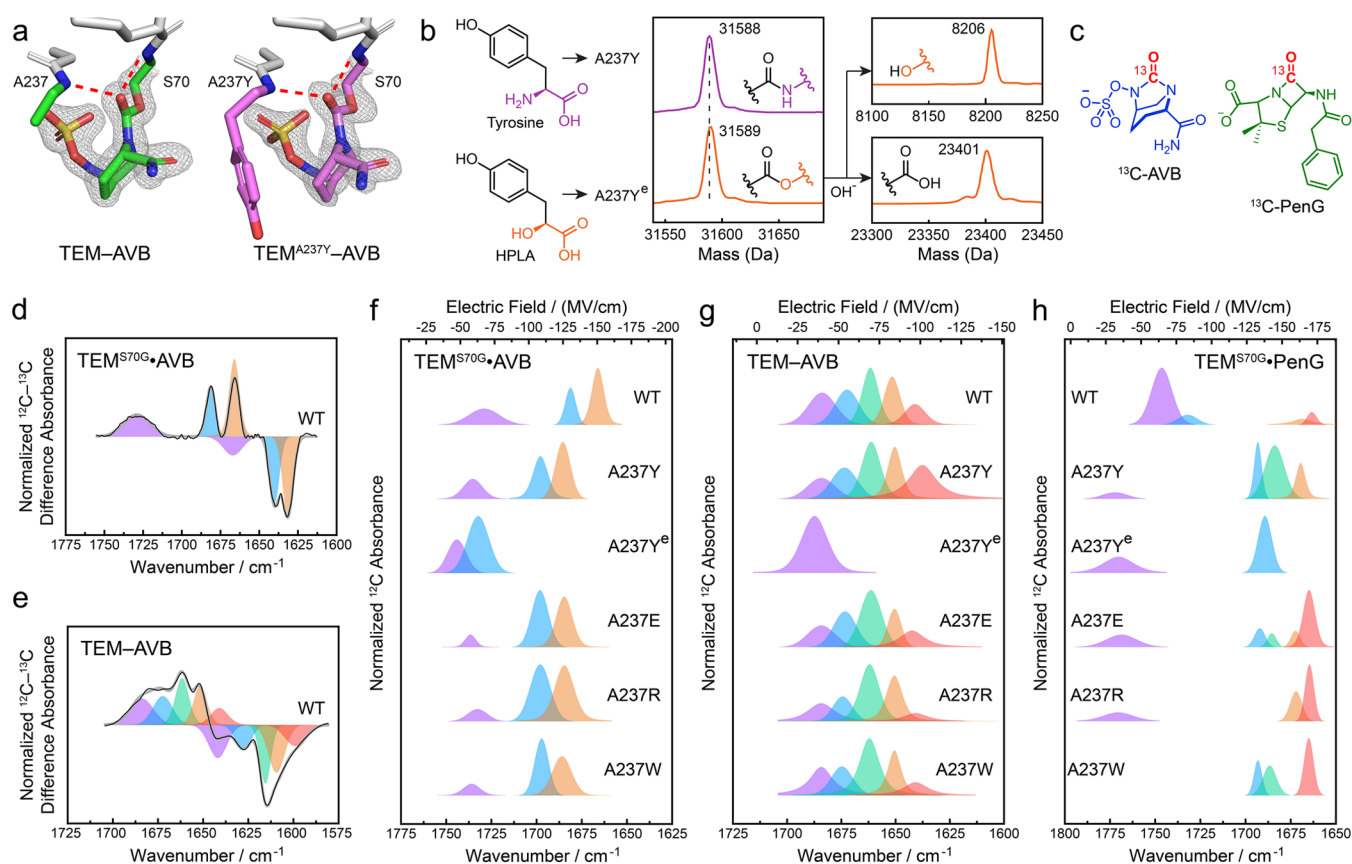


Figure 3. Electrostatic perturbation by A237 mutations measured using isotope-edited infrared spectroscopy. (a) Key active site residues in the WT and A237Y crystal structures of TEM-AVB (Figure S5). The two key H-bonds between the carbamate C=O and the backbone amides are highlighted as red dashed lines. The electron density maps of AVB (2mF_o - DF_c, 1.5σ) are depicted. (b) Substitution of a backbone amide to an ester by incorporation of *p*-hydroxy-L-phenylacetic acid (HPLA), the α -hydroxy acid counterpart of tyrosine, and the high-resolution MS of A237Y, A237Y^e, and the two protein fragments of hydrolyzed A237Y^e (Table S3). (c) ¹³C-labeled AVB and PenG. (d, e) ¹²C–¹³C difference infrared absorption spectra for TEM-AVB (trapped by the S70G mutation) (d) and TEM-AVB (e). The experimental curve (black) is fitted to a sum (gray) of ¹²C (positive) and ¹³C (negative) peaks (curve fitting details in Tables S16 and S17). Peaks belonging to the same positive–negative pair are filled with the same color. (f–h) Fitted ¹²C peaks in infrared absorption spectra for WT and A237 mutants of TEM-AVB (f), TEM-AVB (g), and TEM-PenG (h). The top electric field axes are mapped from the bottom frequency axes based on calibration results as detailed in the Supporting Information.

The ¹²C=O vibrational frequencies were translated into the magnitudes of electric fields projected onto the bond from the environment. To analyze the effects of mutation, we focus on each mutant's largest-field population because it is most electrostatically activated for the reactions (Text S3 in the Supporting Information). For TEM-AVB, a field as large as –150 MV/cm (the negative sign represents stabilization of the

bond dipole) was found (Figure 3f and Table S18). The A237Y mutation decreases the field to –125 MV/cm, which is remarkably further decreased to –63 MV/cm by the A237Y^e mutation. Additionally, A237E, R, and W mutants were expressed, showing similar results to A237Y (Figure 3f). For TEM-AVB, a similar ensemble of electric fields was observed among WT and A237Y, E, R, and W (Figure 3g) with the

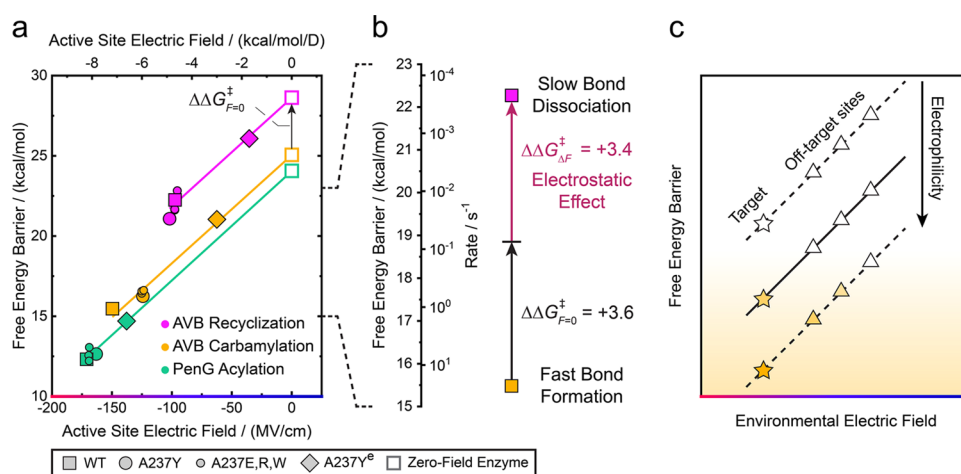


Figure 4. Role of electric fields in covalent inhibition and drug design. (a) Plot of free energy barrier (ΔG^{\ddagger}) against the magnitude of electric fields (F) projected on the reactive C=O for AVB carbamylation, recyclization, and PenG acylation. Expressing ΔG^{\ddagger} in kcal/mol and F in units of kcal/mol/D (top axis), the linear regression lines are $\Delta G^{\ddagger} = 1.40F + 25.0$ (AVB carbamylation), $\Delta G^{\ddagger} = 1.42F + 28.6$ (AVB recyclization), and $\Delta G^{\ddagger} = 1.42F + 24.0$ (PenG acylation). (b) Contribution of electrostatic catalysis, $\Delta\Delta G_{AF}^{\ddagger}$, to the ΔG^{\ddagger} gap between WT AVB carbamylation and recyclization. (c) Conceptual illustration of using two handles together—bond electrophilicity and environmental electric field—to tune the rate of covalent inhibition (illustrated by the shade of orange). Ideally, only the high-field target reaches high reactivity (filled in orange) while the low-field, off-target sites remain under-reactive (unfilled).

largest fields dropped to ca. -100 MV/cm compared with those in TEM-AVB, as recapitulated by polarizable MD simulations (Figure S29). A237Y^e was observed with only the smallest field (-35 MV/cm) (Figure 3g) due to inaccessibility of the electrostatic environments involving the H-bond donated by the backbone amide of A237.

We also measured the isotope-edited infrared absorption spectra for TEM-PenG (Figure S30 and Table S19) using ^{13}C -labeled PenG (Figure 3c).^{11,31} Similarly, a distribution of electric fields was observed (Figure 3h), and the A237Y^e mutation again diminished the field magnitude (Table S20 and Text S4 in the Supporting Information). Polarizable MD simulations show that PenG's β -lactam C=O is still properly loaded into the active site of A237Y^e albeit forming only one H-bond (Figure S31), a conformation likely enforced by many other noncovalent interactions. The calculated field magnitudes match well with experimentally measured ones (largest-field populations) and display an intimate correlation with H-bond number and length (Figure S31).

Electrostatic Catalysis of PenG Acylation, AVB Carbamylation, and AVB Recyclization. To correlate the magnitude of electric fields with free energy barriers, we carried out kinetic studies to obtain k_{ac} for PenG (Figures S32 and S33) and k_{cbm} and k_{rec} for AVB (Figures S34–S37 and Text S5 in the Supporting Information). Compared with A237Y, A237Y^e follows the same kinetic models but shows a decrease in k_{cbm} , k_{rec} , and k_{ac} by factors of 3.5×10^3 , 5.0×10^3 , and 33, respectively (Tables 1 and S1 and S2). Based on the obtained rates, the free energy barrier of these reactions was calculated using transition state theory (Tables S21 and S22) and plotted against the largest electric fields measured for each mutant (Figure 4a). Under the framework of electrostatic catalysis, and if we make a simplifying assumption that the electric field experienced by the C=O is the same for the reactant and transition state,¹⁷ linear fittings provide intercepts $\Delta G_{F=0}^{\ddagger} = 25.0$, 28.6, and 24.0 kcal/mol for AVB carbamylation, recyclization, and PenG acylation, respectively, where $\Delta G_{F=0}^{\ddagger}$ is the hypothetical activation barrier if there were no electric field in TEM active sites. These results indicate that without a

stabilizing electric field, AVB and PenG would have similar reactivity for bonding with S70 while AVB recyclization is less reactive than carbamylation by $\Delta\Delta G_{F=0}^{\ddagger} = 3.6$ kcal/mol (Figure 4a). We suggest this difference originates from three components: (1) the difference in intrinsic electrophilicity of the bonds, being a urea for carbamylation and a carbamate for recyclization, (2) the difference in nucleophilicity, and (3) the difference in nucleophile positioning (the nucleophile for recyclization is too far away as shown in Figure S38).

The slopes of the linear fittings are $|\Delta\vec{\mu}_{rxn}| = 1.40$, 1.42, and 1.42 D for AVB carbamylation, recyclization, and PenG acylation, respectively, showing that the three reactions have a similar increase in dipole moment upon passage from the reactant C=O to the transition states preceding the tetrahedral C–O[−] intermediates (Figure 2a,b). These $|\Delta\vec{\mu}_{rxn}|$ values are reasonably larger than that of the reaction in ketosteroid isomerase (1.05 D), where a C=O substrate is transformed to an enolate C=C–O[−] intermediate.¹⁷ $|\Delta\vec{\mu}_{rxn}|$ is also a measure of a reaction's sensitivity to electrostatic catalysis, indicating that the three reactions have similar "catalyzability" by an electric field.¹⁹ As a result, the very large field in WT TEM-PenG (-171 MV/cm) provides an enhancement of k_{ac} by 8.6 orders of magnitude, while a similarly large field in TEM-AVB (-150 MV/cm) enhances k_{cbm} by 7.5 orders of magnitude, making the bonding of the covalent inhibitor almost as fast as that of the substrate. The much smaller field in TEM-AVB (-97 MV/cm) only accelerates recyclization by 4.9 orders of magnitude. The $10^{2.6}$ -fold less acceleration corresponds to an electrostatic increase in the free energy barrier by $\Delta\Delta G_{AF}^{\ddagger} = 3.4$ kcal/mol (Figure 4b). This analysis provides a quantitative model to assess the role of electric field in impairing the recyclization reaction. If the C=O in TEM-AVB experienced the same magnitude of electric field as that in TEM-AVB, the recyclization would run 320-fold faster, shortening the residence time from 72 min to 13 s. Such an undesired enhancement in recyclization would substantially shift K_i^* from 0.74 to 240 nM. Our quantitative experimental evidence suggests an electrostatic gating effect in TEM active sites that

promotes the forward reaction but relatively suppresses the reverse reaction, making AVB a faster, tighter-binding, and longer-acting covalent inhibitor.

DISCUSSION

Our studies of TEM/AVB provide a new physical basis for understanding the working principles of covalent inhibition. Currently, the most exploited chemical tool for modulating the reactivity of covalent inhibitors is to tune the electrophilicity of warheads.⁸ The concept of electrostatic catalysis as we demonstrated in this work adds an additional axis to guide reactivity optimization (Figure 4c). If a target site provides large electric fields, it will be preferred for covalent bond formation against off-target sites with small fields even though the off-target sites are equally nucleophilic and positioned. The electrostatic effect can be coupled with electrophilicity tuning such that only the on-target reaction is promoted to a satisfactory level of pharmacodynamics while off-target sites are left with higher energy barriers and negligible rates (Figure 4c).

We see the importance of targeting protein sites that are not only nucleophilic but also surrounded by charges and dipoles that can facilitate electrostatic catalysis. Given recent advances in structure prediction³² from which electrostatic potentials can be readily computed, an analysis of protein electric fields could be a valuable screen both for target sites and to avoid unintended nucleophiles that happen to be in regions where the fields are large and in orientations²⁹ that are potentially reaction productive. To search for protein sites amenable to covalent bond formation, we propose the following workflow: (i) obtain the structure of the target protein, from either experimental data or structure prediction programs, (ii) generate an electrostatic potential map using MD simulations or more advanced theories (polarizable force fields appear to give more realistic results but at a considerable computational cost), (iii) convert the electrostatic potential map into an electric field map by taking the gradient, and (iv) rank protein sites based on (a) the magnitude of the electric field, (b) the nucleophilicity of the residues nearby, and (c) spatial accessibility/steric hindrance. We envision that protein electric fields can provide a general, quantitative descriptor to predict which site in a protein and which protein within a proteome is preferred for covalent bonding. This is fundamentally different from the concept of electrostatic complementarity (Figure 1b), which addresses all of the charges in a ligand, such as the sulfate and amide side groups of AVB, and thus largely affects the binding constants (K_M for substrates and K_I for inhibitors). Electrostatic catalysis focuses on the fields that are experienced only by the reactive bond and therefore drives reaction rates (k_{cat} for substrates, and k_{on} and k_{off} for covalent inhibitors).

Covalent inhibitors should be structurally designed to engage in electrostatic interactions through proper positioning of the warheads. AVB inhibition naturally utilizes the same large fields fashioned by the catalytic apparatus. But when targeting noncatalytic nucleophiles,³³ or when there is no such luxury of choosing from multiple candidate residues, a thorough examination of the vicinity of the chosen nucleophile to fully exploit polar residues, backbone amides, and structured water for their potential to exert electric fields may lead to new design options. An ideal configuration is to have a C=O (e.g., acryl) warhead not just be attacked by protein nucleophiles (e.g., cysteine and serine) from a perpendicular direction to the bond axis but also experience two coplanar, strong H-bonds. Indeed, H-bonded warheads are found in the crystal structures

of BTK1–ibrutinib (Figure S39),³⁴ KRAS-G12C–sotorasib (Figure S40),³⁵ DPP-IV–saxagliptin (Figure S41),³⁶ and NS3/4A–protease–telaprevir (Figure S42),³⁷ where electric fields may contribute to the efficacy of these covalent inhibitors, though this factor was not recognized. Given that more inhibitor warheads are not H-bonded even though potential H-bond donors are available, there exists a vast space for improving their selectivity. As illustrated in Figure 1a and with the results presented here as an example for TEM/AVB interactions, these four fundamental components—electrophilicity, nucleophilicity, nucleophile positioning with respect to electrophile, and environmental electric field—together provide a basis for understanding reactivity, selectivity, and relative stability.

ASSOCIATED CONTENT

Supporting Information

The Supporting Information is available free of charge at <https://pubs.acs.org/doi/10.1021/jacs.2c09876>.

Experimental details on protein expression and purification, mass spectrometry, crystallography, protein ¹H NMR, ¹³C-AVB synthesis, vibrational spectroscopy, enzyme kinetics, and covalent inhibition kinetics, as well as MD simulation methods and extended discussions (PDF)

Accession Codes

All X-ray density maps and atomic models for the proteins have been deposited in the Protein Data Bank. WT TEM-1, 7U6Q; A237Y TEM-1, 8DDZ; WT TEM–AVB, 8DE0; A237Y TEM–AVB, 8DE1; A237Y TEM–AVB at room temperature, 8DE2.

AUTHOR INFORMATION

Corresponding Author

Steven G. Boxer – Department of Chemistry, Stanford University, Stanford, California 94305, United States; orcid.org/0000-0001-9167-4286; Email: sboxer@stanford.edu

Authors

Zhe Ji – Department of Chemistry, Stanford University, Stanford, California 94305, United States; orcid.org/0000-0002-8532-333X

Jacek Kozuch – Department of Physics, Freie Universität Berlin, D-14195 Berlin, Germany; Research Building SupraFAB, 14195 Berlin, Germany; orcid.org/0000-0002-2115-4899

Irimpan I. Mathews – Stanford Synchrotron Radiation Lightsource, Menlo Park, California 94025, United States; orcid.org/0000-0001-6254-3519

Christian S. Diercks – Department of Chemistry, Scripps Research, La Jolla, California 92037, United States; orcid.org/0000-0002-7813-0302

Yasmin Shamsudin – Department of Chemistry-BMC, Uppsala University, 752 37 Uppsala, Sweden; orcid.org/0000-0002-6249-9877

Mirjam A. Schulz – Department of Physics, Freie Universität Berlin, D-14195 Berlin, Germany; Research Building SupraFAB, 14195 Berlin, Germany; orcid.org/0000-0003-4201-8092

Complete contact information is available at: <https://pubs.acs.org/doi/10.1021/jacs.2c09876>

Notes

The authors declare no competing financial interest.

ACKNOWLEDGMENTS

The authors thank C. Zheng, S. H. Schneider, and S. D. E. Fried for helpful discussions. They also thank P. Soumilion and P. G. Schultz for providing plasmids, T. McLaughlin and the Vincent Coates Foundation Mass Spectrometry Laboratory, Stanford University Mass Spectrometry core facility for the help with mass spectrometry, and S. Lynch from Stanford University NMR facility for assistance with ^1H protein NMR. This work was supported in part by NIH Grant GM118044. J.K. and M.A.S. were supported by German Research Foundation grant KO 5464/4. J.K. and M.A.S. thank the support of the SupraFAB research building (funded by Federal Government and the State of Berlin) and the ZEDAT for computational resources (Freie Universität Berlin). Y.S. was supported by the Knut and Alice Wallenberg Foundation. Y.S. thanks the Swedish National Infrastructure for Computing (SNIC) for computational resources. Use of the Stanford Synchrotron Radiation Lightsource, SLAC National Accelerator Laboratory, was supported by the US Department of Energy, Office of Science, Office of Basic Energy Sciences under Contract No. DE-AC02-76SF00515. The SSRL Structural Molecular Biology Program is supported by the DOE Office of Biological and Environmental Research and by the National Institutes of Health, National Institute of General Medical Sciences (P30GM133894). The contents of this publication are solely the responsibility of the authors and do not necessarily represent the official views of NIGMS or NIH.

ABBREVIATIONS

PenG	penicillin G
AVB	avibactam
WT	wild type
HPLA	<i>p</i> -hydroxy- <i>L</i> -phenyllactic acid
MS	mass spectrometry
MD	molecular dynamics
BTK	Bruton's tyrosine kinase
KRAS	a protein translated from the gene <i>KRAS</i> (Kirsten rat sarcoma virus)
DPP	dipeptidyl peptidase

REFERENCES

- (1) Singh, J.; Petter, R. C.; Baillie, T. A.; Whitty, A. The Resurgence of Covalent Drugs. *Nat. Rev. Drug Discovery* **2011**, *10*, 307–317.
- (2) Sutanto, F.; Konstantinidou, M.; Domling, A. Covalent Inhibitors: A Rational Approach to Drug Discovery. *RSC Med. Chem.* **2020**, *11*, 876–884.
- (3) Spradlin, J. N.; Zhang, E.; Nomura, D. K. Reimagining Druggability Using Chemoproteomic Platforms. *Acc. Chem. Res.* **2021**, *54*, 1801–1813.
- (4) Bradshaw, J. M.; McFarland, J. M.; Paavilainen, V. O.; Bisconte, A.; Tam, D.; Phan, V. T.; Romanov, S.; Finkle, D.; Shu, J.; Patel, V.; Ton, T.; Li, X.; Loughhead, D. G.; Nunn, P. A.; Karr, D. E.; Gerritsen, M. E.; Funk, J. O.; Owens, T. D.; Verner, E.; Brameld, K. A.; Hill, R. J.; Goldstein, D. M.; Taunton, J. Prolonged and Tunable Residence Time Using Reversible Covalent Kinase Inhibitors. *Nat. Chem. Biol.* **2015**, *11*, 525–531.
- (5) Alexander, J. P.; Cravatt, B. F. Mechanism of Carbamate Inactivation of FAAH: Implications for the Design of Covalent Inhibitors and in vivo Functional Probes for Enzymes. *Chem. Biol.* **2005**, *12*, 1179–1187.
- (6) Pan, Z.; Scheerens, H.; Li, S. J.; Schultz, B. E.; Sprengeler, P. A.; Burrill, L. C.; Mendonca, R. V.; Sweeney, M. D.; Scott, K. C.; Grothaus, P. G.; Jeffery, D. A.; Spoerke, J. M.; Honigberg, L. A.; Young, P. R.; Dalrymple, S. A.; Palmer, J. T. Discovery of Selective Irreversible Inhibitors for Bruton's Tyrosine Kinase. *ChemMedChem* **2007**, *2*, 58–61.
- (7) Ostrem, J. M.; Peters, U.; Sos, M. L.; Wells, J. A.; Shokat, K. M. K-Ras(G12C) Inhibitors Allosterically Control GTP Affinity and Effector Interactions. *Nature* **2013**, *503*, 548–551.
- (8) Gehringer, M.; Laufer, S. A. Emerging and Re-Emerging Warheads for Targeted Covalent Inhibitors: Applications in Medicinal Chemistry and Chemical Biology. *J. Med. Chem.* **2019**, *62*, 5673–5724.
- (9) Serafimova, I. M.; Pufall, M. A.; Krishnan, S.; Duda, K.; Cohen, M. S.; Maglathlin, R. L.; McFarland, J. M.; Miller, R. M.; Frodin, M.; Taunton, J. Reversible Targeting of Noncatalytic Cysteines with Chemically Tuned Electrophiles. *Nat. Chem. Biol.* **2012**, *8*, 471–476.
- (10) Frere, J. M. Beta-Lactamases and Bacterial Resistance to Antibiotics. *Mol. Microbiol.* **1995**, *16*, 385–395.
- (11) Schneider, S. H.; Kozuch, J.; Boxer, S. G. The Interplay of Electrostatics and Chemical Positioning in the Evolution of Antibiotic Resistance in TEM β -Lactamases. *ACS Cent. Sci.* **2021**, *7*, 1996–2008.
- (12) Stachyra, T.; Péchereau, M.-C.; Bruneau, J.-M.; Claudon, M.; Frère, J.-M.; Miossec, C.; Coleman, K.; Black, M. T. Mechanistic Studies of the Inactivation of TEM-1 and P99 by NXL104, a Novel Non- β -Lactam β -Lactamase Inhibitor. *Antimicrob. Agents Chemother.* **2010**, *54*, 5132–5138.
- (13) Ehmman, D. E.; Jahic, H.; Ross, P. L.; Gu, R. F.; Hu, J.; Kern, G.; Walkup, G. K.; Fisher, S. L. Avibactam is a Covalent, Reversible, Non- β -Lactam β -Lactamase Inhibitor. *Proc. Natl. Acad. Sci. U.S.A.* **2012**, *109*, 11663–11668.
- (14) Ehmman, D. E.; Jahic, H.; Ross, P. L.; Gu, R. F.; Hu, J.; Durand-Reville, T. F.; Lahiri, S.; Thresher, J.; Livchak, S.; Gao, N.; Palmer, T.; Walkup, G. K.; Fisher, S. L. Kinetics of Avibactam Inhibition against Class A, C, and D β -Lactamases. *J. Biol. Chem.* **2013**, *288*, 27960–27971.
- (15) Zhanel, G. G.; Lawson, C. D.; Adam, H.; Schweizer, F.; Zelenitsky, S.; Lagace-Wiens, P. R. S.; Denisuk, A.; Rubinstein, E.; Gin, A. S.; Hoban, D. J.; Lynch, J. P.; Karlowsky, J. A. Ceftazidime-Avibactam: A Novel Cephalosporin/ β -Lactamase Inhibitor Combination. *Drugs* **2013**, *73*, 159–177.
- (16) Warshel, A.; Sharma, P. K.; Kato, M.; Xiang, Y.; Liu, H. B.; Olsson, M. H. M. Electrostatic Basis for Enzyme Catalysis. *Chem. Rev.* **2006**, *106*, 3210–3235.
- (17) Fried, S. D.; Bagchi, S.; Boxer, S. G. Extreme Electric Fields Power Catalysis in the Active Site of Ketosteroid Isomerase. *Science* **2014**, *346*, 1510–1514.
- (18) Schneider, S. H.; Boxer, S. G. Vibrational Stark Effects of Carbonyl Probes Applied to Reinterpret IR and Raman Data for Enzyme Inhibitors in terms of Electric Fields at the Active Site. *J. Phys. Chem. B* **2016**, *120*, 9672–9684.
- (19) Fried, S. D.; Boxer, S. G. Electric Fields and Enzyme Catalysis. *Annu. Rev. Biochem.* **2017**, *86*, 387–415.
- (20) Vaissier, V.; Sharma, S. C.; Schaettle, K.; Zhang, T.; Head-Gordon, T. Computational Optimization of Electric Fields for Improving Catalysis of a Designed Kemp Eliminase. *ACS Catal.* **2018**, *8*, 219–227.
- (21) Welborn, V. V.; Head-Gordon, T. Fluctuations of Electric Fields in the Active Site of the Enzyme Ketosteroid Isomerase. *J. Am. Soc. Chem.* **2019**, *141*, 12487–12492.
- (22) Shaik, S.; Danovich, D.; Joy, J.; Wang, Z.; Stuyver, T. Electric-Field Mediated Chemistry: Uncovering and Exploiting the Potential of (Oriented) Electric Fields to Exert Chemical Catalysis and Reaction control. *J. Am. Chem. Soc.* **2020**, *142*, 12551–12562.
- (23) Aragonès, A. C.; Haworth, N. L.; Darwish, N.; Ciampi, S.; Bloomfield, N. J.; Wallace, G. G.; Diez-Perez, I.; Coot, M. L. Electrostatic Catalysis of a Diels-Alder Reaction. *Nature* **2016**, *531*, 88–91.

(24) Zang, Y.; Zou, Q.; Fu, T.; Ng, F.; Fowler, B.; Yang, J.; Li, H.; Steigerwald, M. L.; Nuckolls, C.; Venkataraman, L. Direct isomerization reactions of cumulenes with electric fields. *Nat. Commun.* **2019**, *10*, No. 4482.

(25) Fried, S. D.; Boxer, S. G. Measuring Electric Fields and Noncovalent Interactions Using the Vibrational Stark Effect. *Acc. Chem. Res.* **2015**, *48*, 998–1006.

(26) Blow, D. M. Rearrangement of Cruickshank's Formulae for the Diffraction-Component Precision Index. *Acta. Crystallogr. D* **2002**, *58*, 792–797.

(27) Guo, J. T.; Wang, J. Y.; Anderson, J. C.; Schultz, P. G. Addition of an α -Hydroxy Acid to the Genetic Code of Bacteria. *Angew. Chem., Int. Ed.* **2008**, *47*, 722–725.

(28) Fried, S. D.; Bagchi, S.; Boxer, S. G. Measuring Electrostatic Fields in both Hydrogen-Bonding and Non-Hydrogen-Bonding Environments Using Carbonyl Vibrational Probes. *J. Am. Chem. Soc.* **2013**, *135*, 11181–11192.

(29) Zheng, C.; Mao, Y. Z.; Kozuch, J.; Atsango, A.; Ji, Z.; Markland, T. E.; Boxer, S. G. A Two-Directional Vibrational Probe Reveals Different Electric Field Orientations in Solution and an Enzyme Active Site. *Nat. Chem.* **2022**, *14*, 891–897.

(30) Pemberton, O. A.; Noor, R. E.; Kumar, M. V. V.; Sanishvili, R.; Kemp, M. T.; Kearns, F. L.; Woodcock, H. L.; Gelis, I.; Chen, Y. Mechanism of Proton Transfer in Class A β -Lactamase Catalysis and Inhibition by Avibactam. *Proc. Natl. Acad. Sci. U.S.A.* **2020**, *117*, 5818–5825.

(31) Kozuch, J.; Schneider, S. H.; Boxer, S. G. Biosynthetic Incorporation of Site-Specific Isotopes in β -Lactam Antibiotics Enables Biophysical Studies. *ACS Chem. Biol.* **2020**, *15*, 1148–1153.

(32) Jumper, J.; Evans, R.; Pritzel, A.; Green, T.; Figurnov, M.; Ronneberger, O.; Tunyasuvunakool, K.; Bates, R.; Zidek, A.; Potapenko, A.; Bridgland, A.; Meyer, C.; Kohl, S. A. A.; Ballard, A. J.; Cowie, A.; Romera-Paredes, B.; Nikolov, S.; Jain, R.; Adler, J.; Back, T.; Petersen, S.; Reiman, D.; Clancy, E.; Zielinski, M.; Steinegger, M.; Pacholska, M.; Berghammer, T.; Bodenstein, S.; Silver, D.; Vinyals, O.; Senior, A. W.; Kavukcuoglu, K.; Kohli, P.; Hassabis, D. Highly Accurate Protein Structure Prediction with AlphaFold. *Nature* **2021**, *596*, 583–589.

(33) Singh, J. The Ascension of Targeted Covalent Inhibitors. *J. Med. Chem.* **2022**, *65*, 5886–5901.

(34) Bender, A. T.; Gardberg, A.; Pereira, A.; Johnson, T.; Wu, Y.; Grenningloh, R.; Head, J.; Morandi, F.; Haselmayer, P.; Liu-Bujalski, L. Ability of Bruton's Tyrosine Kinase Inhibitors to Sequester Y551 and Prevent Phosphorylation Determines Potency for Inhibition of Fc Receptor but Not B-Cell Receptor Signaling. *Mol. Pharmacol.* **2017**, *91*, 208–219.

(35) Canon, J.; Rex, K.; Saiki, A. Y.; Mohr, C.; Cooke, K.; Bagal, D.; Gaida, K.; Holt, T.; Knutson, C. G.; Koppada, N.; Lanman, B. A.; Werner, J.; Rapaport, A. S.; San Miguel, T.; Ortiz, R.; Osgood, T.; Sun, J. R.; Zhu, X.; McCarter, J. D.; Volak, L. P.; Houk, B. E.; Fakih, M. G.; O'Neil, B. H.; Price, T. J.; Falchook, G. S.; Desai, J.; Kuo, J.; Govindan, R.; Hong, D. S.; Ouyang, W.; Henary, H.; Arvedson, T.; Cee, V. J.; Lipford, J. R. The Clinical KRAS(G12C) Inhibitor AMG 510 Drives Anti-Tumour Immunity. *Nature* **2019**, *575*, 217–223.

(36) Metzler, W. J.; Yanchunas, J.; Weigelt, C.; Kish, K.; Klei, H. E.; Xie, D.; Zhang, Y.; Corbett, M.; Tamura, J. K.; He, B.; Hamann, L. G.; Kirby, M. S.; Marcinkeviciene, J. Involvement of DPP-IV Catalytic Residues in Enzyme-Saxagliptin Complex Formation. *Protein Sci.* **2008**, *17*, 240–250.

(37) Romano, K. P.; Ali, A.; Aydin, C.; Soumana, D.; Ozen, A.; Deveau, L. M.; Silver, C.; Cao, H.; Newton, A.; Petropoulos, C. J.; Huang, W.; Schiffer, C. A. The Molecular Basis of Drug Resistance Against Hepatitis C Virus NS3/4A Protease Inhibitors. *PLoS Pathog.* **2012**, *8*, No. e1002832.

Recommended by ACS

Alkaline State of the Domain-Swapped Dimer of Human Cytochrome *c*: A Conformational Switch for Apoptotic Peroxidase Activity

Haotian Lei, Bruce E. Bowler, *et al.*

NOVEMBER 08, 2022

JOURNAL OF THE AMERICAN CHEMICAL SOCIETY

READ 

Intramolecular C–C Bond Formation Links Anthraquinone and Eneidyne Scaffolds in Tiancimycin Biosynthesis

Chun Gui, Ben Shen, *et al.*

OCTOBER 24, 2022

JOURNAL OF THE AMERICAN CHEMICAL SOCIETY

READ 

Cooperative Weak Dispersive Interactions Actuate Catalysis in a Shape-Selective Abiological Racemase

Yujia Wang, Jay S. Siegel, *et al.*

FEBRUARY 04, 2022

JOURNAL OF THE AMERICAN CHEMICAL SOCIETY

READ 

Total Synthesis of (+)-Mutilin: A Transannular [2+2] Cycloaddition/Fragmentation Approach

Han Chen, Tuoping Luo, *et al.*

AUGUST 22, 2022

JOURNAL OF THE AMERICAN CHEMICAL SOCIETY

READ 

Get More Suggestions >

Supporting Information

Protein electric fields enable faster and longer-lasting covalent inhibition of β -lactamases

Zhe Ji¹, Jacek Kozuch^{2,3}, Irimpan I. Mathews⁴, Christian S. Diercks⁵, Yasmin Shamsudin⁶, Mirjam A. Schulz^{2,3} and Steven G. Boxer^{1,*}

¹Department of Chemistry, Stanford University, Stanford, CA 94305, USA.

²Department of Physics, Experimental Molecular Biophysics, Freie Universität Berlin, Arnimallee 14, D-14195 Berlin, Germany.

³Research building SupraFAB, Altensteinstr. 23a, 14195 Berlin, Germany.

⁴Stanford Synchrotron Radiation Lightsource, Menlo Park, CA 94025, USA.

⁵Department of Chemistry, Scripps Research, La Jolla, CA 92037, USA.

⁶Department of Chemistry-BMC, Uppsala University, 752 37 Uppsala, Sweden.

*Email: sboxer@stanford.edu

Table of Contents

Materials and Methods.....	4
Plasmid Construction.....	4
DNA Sequence.....	4
Protein Sequence.....	5
Protein Expression and Purification.....	5
Mass Spectrometry.....	7
Protein Crystallization and Crystallography.....	7
Protein ¹ H-NMR.....	8
Synthesis of Avibactam- ¹³ C.....	9
Calibration of Vibrational Stark Probes.....	12
Isotope-Edited FTIR Spectroscopy.....	14
Polarizable MD Simulations of Proteins.....	15
Kinetic Measurement on PenG Hydrolysis by β -Lactamases.....	16
Kinetic Measurement on AVB Inhibition of β -Lactamases.....	19
Supplementary Text.....	25
Text S1.....	25
Text S2.....	25
Text S3.....	26
Text S4.....	26
Text S5.....	26
Figure S1.....	27
Figure S2.....	28
Figure S3.....	29
Figure S4.....	30
Figure S5.....	31
Figure S6.....	32
Figure S7.....	33
Figure S8.....	34
Figure S9.....	35
Figure S10.....	36
Figure S11.....	37
Figure S12.....	38
Figure S13.....	39
Figure S14.....	40
Figure S15.....	41
Figure S16.....	42
Figure S17.....	43
Figure S18.....	44
Figure S19.....	45
Figure S20.....	46
Figure S21.....	47
Figure S22.....	48
Figure S23.....	49
Figure S24.....	50
Figure S25.....	51

Figure S26.....	52
Figure S27.....	53
Figure S28.....	54
Figure S29.....	55
Figure S30.....	56
Figure S31.....	57
Figure S32.....	58
Figure S33.....	59
Figure S34.....	60
Figure S35.....	61
Figure S36.....	62
Figure S37.....	63
Figure S38.....	64
Figure S39.....	65
Figure S40.....	66
Figure S41.....	67
Figure S42.....	68
Table S1.....	69
Table S2.....	70
Table S3.....	71
Table S4.....	72
Table S5.....	73
Table S6.....	74
Table S7.....	75
Table S8.....	76
Table S9.....	77
Table S10.....	78
Table S11.....	79
Table S12.....	80
Table S13.....	81
Table S14.....	82
Table S15.....	83
Table S16.....	84
Table S17.....	85
Table S18.....	86
Table S19.....	87
Table S20.....	88
Table S21.....	89
Table S22.....	90
Script 1.....	91
Script 2.....	97
Script 3.....	105
Script 4.....	107
Script 5.....	109
Script 6.....	111
Script 7.....	113

Materials and Methods

Plasmid Construction

The pBAD plasmid containing the gene for TEM-1 β -lactamase was generously provided by the Patrice Soumillion lab at the Université Catholique de Louvain^{1,2}. The pBAD vector is a derivative of pBAD/myc-HisB (Invitrogen), with the gene cloned between the *NcoI* and *XbaI* sites, carrying a tetracycline resistance gene. The TEM-1 gene contains a A184V stabilizing mutation. In our previous publication³, we have incorporated a thrombin cleavage site into the myc tag. This modified plasmid served as the starting point for studying mutants of this work. Point mutations were made using the QuikChange Lightning Site-Directed Mutagenesis Kit (Agilent) according to the manufacturer's protocols.

The site-specific incorporation of a backbone ester was achieved using an aminoacyl-tRNA synthetase (aaRS)⁴. A pUltra plasmid containing the aaRS gene was generously provided by the Peter G. Schultz lab at the Scripps Research Institute.

To make TEM-1 free of the His tag for crystallization, we redesigned the gene by moving the His tag from the C-terminus to the N-terminus, right after the signal peptide. A TEV protease cleavage sequence was incorporated after the His tag. We used M182T for protein stabilization rather than A184V because of M182T's higher stabilization effect⁵ and its wide use for the crystallization of TEM proteins. The gene was inserted between the *NcoI* and *XbaI* sites into the original pBAD vector provided by the Soumillion lab.

DNA Sequence

TEM-1-A184V-His \equiv TEM-1. Codon for S70 and A237 in bold

```
ATGGGTAGTCAACATTTCCGTGTCGCCCTTATTCCTTTTTTGCGGCATTTCCTTCCTGTTT
TTGCTCACCCAGAAACGCTGGTCAAAGTAAAGATGCTGAAGATCAGTTGGGTGCACGAGTGGG
TTACATCGAACTGGATCTCAACAGCGGTAAGATCCTTGAGAGTTTTCGCCCCGAAGAACGTTTT
CCAATGATGAGCACTTTTAAAGTTCTGCTATGTGGCGCGGTATTATCCCGTGTGACGCCGGGC
AAGAGCAACTCGGTCCGCATACACTATTCTCAGAATGACTTGGTTGAGTACTCACCAGTCAC
AGAAAAGCATCTTACGGATGGCATGACAGTAAGAGAATTATGCAGTGCTGCCATAACCATGAGT
GATAACACTGCGGCCAACTTACTTCTGACAACGATCGGAGGACCGAAGGAGCTAACCGCTTTTT
TGCACAACATGGGGGATCATGTAACCTCGCCTTGATCGTTGGGAACCGGAGCTGAATGAAGCCAT
ACCAAACGACGAGCGTGACACCACGATGCCTGTAGCAATGGCAACAACGTTGCGCAAACATTA
ACTGGCGAACTACTTACTCTAGCTTCCCGGCAACAATTAATAGACTGGATGGAGGCGGATAAAG
TTGCAGGACCACTTCTGCGCTCGGCCCTTCCGGCTGGCTGGTTTATTGCTGATAAATCTGGAGC
CGGTGAGCGTGGGTCTCGCGGTATCATTGCAGCACTGGGGCCAGATGGTAAGCCCTCCCGTATC
GTAGTTATCTACACGACGGGGAGTCAGGCAACTATGGATGAACGAAATAGACAGATCGCTGAGA
TAGGTGCCTCACTGATTAAGCATTGGGCTCTAGTACCAAGAGGCAGCTCAGAAGAGGATCTGAA
TAGCGCCGTCGACCATCATCATCATCATTGA
```

TEM-1-M182T-G25 ≡ TEM-1-native. Codon for S70 and A237 in bold

ATGGGTAGTCAACATTTCCGTGTCGCCCTTATTCCCTTTTTTTCGGCATTTCCTTCCTGTTT
TTGCTGCGCGTGAAACCCATCATCATCATCATGGCGCGGAAAACCTGTATTTTCAGGGCCA
CCCAGAAACGCTGGTGAAAGTAAAAGATGCTGAAGATCAGTTGGGTGCACGAGTGGGTACATC
GAACTGGATCTCAACAGCGGTAAGATCCTTGAGAGTTTTTCGCCCGAAGAACGTTTTCCAATGA
TG**AGC**ACTTTTTAAAGTTCTGCTATGTGGCGCGGTATTATCCCGTGTGACGCCGGGCAAGAGCA
ACTCGGTGCGCCGATACACTATTCTCAGAATGACTTGGTTGAGTACTCACCAGTCACAGAAAAG
CATCTTACGGATGGCATGACAGTAAGAGAATTATGCAGTGCTGCCATAACCATGAGTGATAACA
CTGCGGCCAACTTACTTCTGACAACGATCGGAGGACCGAAGGAGCTAACCGCTTTTTTGCACAA
CATGGGGGATCATGTAACCTCGCCTTGATCGTTGGGAACCGGAGCTGAATGAAGCCATAACCAAAC
GACGAGCGTGACACCACGACCCCTGCAGCAATGGCAACAACGTTGCGCAAATTAACCTGGCG
AACTACTTACTCTAGCTTCCCGGCAACAATTAATAGACTGGATGGAGGCGGATAAAGTTGCAGG
ACCACTTCTGCGCTCGGCCCTTCCGGCTGGCTGGTTTTATTGCTGATAAATCTGGAG**CC**GGTGAG
CGTGGGTCTCGCGGTATCATTGCAGCACTGGGGCCAGATGGTAAGCCCTCCCGTATCGTAGTTA
TCTACACGACGGGGAGTCAGGCAACTATGGATGAACGAAATAGACAGATCGCTGAGATAGGTGC
CTCACTGATTAAGCATTGGTGA

Protein Sequence

TEM-1-A184V-His ≡ TEM-1. S70 and A237 in bold; Signal peptide in purple

MGSQHFRVALI**PPFAAFCLPVFA**HPETLVKVKDAEDQLGARVGYIELDLNSGKILESFRPEERF
PMM**S**TFKVLVLCGAVLSRVDAGQEQLGRRIHYSQNDLVEYSPVTEKHLTDGMTVRELCSAAITMS
DNTAANLLLTIGGPKELTAFLHNMGDHSVTRLDRWEPELNEAIPNDERDTTMPVAMATTLRKL
TGELLTLASRQQLIDWMEADKVAGPLLRSAIPAGWFIADKSG**A**GERGSRGIIAALGPDGKPSRI
VVIYTTGSQATMDERNRQIAEIGASLIKHWALVPRGSSEEDLNSAVDHHHHHH

TEM-1-M182T-G25 ≡ TEM-1-native. S70 and A237 in bold; Signal peptide in purple;

Cleavable His tag in green

MGSQHFRVALI**PPFAAFCLPVFA****ARETHHHHHHGAENLYFQ**GHPELVKVKDAEDQLGARVGYI
ELDLNSGKILESFRPEERFPMM**S**TFKVLVLCGAVLSRVDAGQEQLGRRIHYSQNDLVEYSPVTEK
HLTDGMTVRELCSAAITMSDNTAANLLLTIGGPKELTAFLHNMGDHSVTRLDRWEPELNEAIPN
DERDTTTPAAMATTLRKLTLGELLTLASRQQLIDWMEADKVAGPLLRSAIPAGWFIADKSG**A**GE
RSGRGI AALGPDGKPSRIVVIYTTGSQATMDERNRQIAEIGASLIKHW

Protein Expression and Purification

The general protocol for TEM-1: The pBAD plasmid was transformed into chemically competent TOP10 *Escherichia coli* cells (Invitrogen) using selection with 15 µg/mL tetracycline (sigma) on Luria Broth (Fisher) agar plates. A single colony of transformed cells was grown into 1 mL culture for 8 h and further into 50 mL cultures overnight using Luria Broth with 15 µg/mL tetracycline at 37°C. 50 mL of an overnight culture was used to inoculate 1 L of Terrific Broth (Fisher) with 10 µg/mL tetracycline shaking at 200 rpm and 37°C until they reached an OD₆₀₀ ~ 0.6, at which point protein expression was induced with 2 g/L L-(+)-arabinose (Sigma), and grown for 6 h at 27°C. Cells were harvested by centrifugation at 6,000 × g for 20 mins and resuspended

in a lysis buffer (50 mM potassium phosphate (KPi), 20 mM imidazole, 500 mM NaCl, 10% (v/v) glycerol, pH 7.4). Cells were lysed with a homogenizer (Avestin EmulsiFlex-C3), and the lysate was centrifuged twice for 90 min each at $15,000 \times g$. The crude protein in the supernatant was filtered through a 0.45 μm filter membrane before being loaded onto a Ni-NTA affinity resin (QIAGEN) column equilibrated with the lysis buffer. The protein was purified using 6 column volumes of a washing buffer (50 mM KPi, 50 mM imidazole, 500 mM NaCl, pH 7.4) and 2 column volumes of an elution buffer (50 mM KPi, 200 mM imidazole, 500 mM NaCl, pH 7.4). Further purification was performed using anion exchange chromatography on a 5 mL HiTrap-Q HP (GE Healthcare) column and eluted using a 0-25% gradient of buffer A (25 mM Tris-HCl, 25 mM NaCl, pH 8.4) and buffer B (25 mM Tris-HCl, 1 M NaCl, pH 8.4) over 25 column volumes. Purified protein was exchanged into a cryoprotecting storage buffer (50 mM KPi, 100 mM NaCl, 10% (v/v) glycerol, pH 7.4) for long-term storage at -80°C . A typical yield is 5 mg of protein from 1 L of media. The identity and purity of all proteins were confirmed with mass spectrometry (MS). The expected and observed masses are summarized in Table S3.

A237Y^c: For the expression of A237Y^c, the genes *aspC* and *tyrB* in DH10B cells were knocked out by using phage λ -red recombinase, in order to impair their capability to metabolize the non-canonical hydroxy acid, *p*-hydroxy-L-phenyllactic acid (HPLA, AstaTech)⁴. The success of gene knockout was confirmed by testing the dependence of cell growth on an external tyrosine source. Cells failed to grow in a media depleted with tyrosine due to the removal of *tyrB* (Table S9). Furthermore, growing the modified DH10B cells with HPLA overnight after OD₆₀₀ had reached 0.6 led to a concentration drop of HPLA only from 1 mM to 0.7 mM in the media, as quantified by HPLC, while growing the native DH10B cells led to a final HPLA concentration of merely 0.04 mM (Figure S7). These results confirmed that the modified DH10B cells have lost the capability to metabolize HPLA, allowing for prolonged existence of HPLA in the media for protein expression.

The modified DH10B cells were made chemically competent and sequentially transformed with the aaRS plasmid (selection with 50 $\mu\text{g}/\text{mL}$ spectinomycin) and the pBAD plasmid (selection with 15 $\mu\text{g}/\text{mL}$ tetracycline). The protein expression was carried out in the same way except for additionally using 50 $\mu\text{g}/\text{mL}$ spectinomycin as antibiotics and using 1 mM isopropyl β -D-1-thiogalactopyranoside (IPTG, Santa Cruz Biotechnology) and 2 mM HPLA for induction. The protein purification was carried out in the same way except for using buffers of lower pH for anion exchange chromatography: buffer C (12.5 mM KPi, 6.25 mM NaCl, pH 7.4) and buffer D (50 mM KPi, 1 M NaCl, pH 7.4). The lower pH reduces the hydrolysis of the backbone ester. A similar yield of 5 mg of protein from 1 L of media can be achieved.

The incorporation of the backbone ester was confirmed first by a hydrolysis test. 0.1 mg of A237^c was incubated with 0.5 M NaOH for 1 h at room temperature (RT). The reaction mixture was neutralized by acetic acid before a MS measurement. MS spectra displayed a complete decomposition of A237Y^c into two peptide fragments, corresponding to the hydrolysis of the very backbone ester (Figures 3b and S8, and Table S3). High-resolution MS further characterized the extra mass carried by the backbone ester. The O atom is heavier than the NH group by 1 Da and this difference was captured (Figure 3b). The hydrolysis fragments were also measured by high-resolution MS and showed a gain in their total mass by 18 Da (Figure 3b), corresponding to the addition of H₂O associated with ester hydrolysis. The amide protein A237Y cannot be hydrolyzed

under the same conditions. The incorporation fidelity was estimated to be ~ 99% according to kinetic tests (Table S1).

TEM-1-native: For the expression of TEM-1-native proteins using the corresponding plasmids, protein expression and purification were carried out in the same way except for adding two extra steps. After the crude protein was collected from a Ni-NTA affinity column in the elution buffer, TEV protease (Gene and Cell Technologies) was added (0.2 mg TEV protease per 1 mg crude protein) for the cleavage of the His tag. Complete cleavage (> 95%) was observed after incubation at 30 min at RT by MS. The mixture was diluted 10 times by water before being loaded onto the Ni-NTA affinity column equilibrated with the same 10-fold dilution of the elution buffer. The column was washed with 2 column volumes of the washing buffer. All the solution that has flowed through the column by this point was collected and used for the anion exchange chromatography as described above. A similar final yield of 5 mg of protein from 1 L of media can be achieved.

Mass Spectrometry

Mass spectrometry (MS) was performed at the Stanford University Mass Spectrometry facility on a Waters Single Quadrupole Mass Spectrometer and Acuity H Class UPLC equipped with a reverse-phase C8 column (Zorbax 300SB-C8, Rapid Resolution 2.1 × 50 mm 3.5u with 300SB-C8 Narrow=Bore Guard column 2.1 × 12.5mm 5u). The LC mobile phases consist of 0.1% formic acid in water and 0.1% formic acid in acetonitrile. ESI was performed under standard cone voltage. The mass was recorded in ESI+ mode in the range of 50-2000 m/z. Data deconvolution and analysis was performed using the Intact Mass software (Protein Metrics).

High-resolution MS was performed at the Stanford University Mass Spectrometry facility on the Waters Acuity UPLC and Bruker MicroTOF-Q II. The column was a 2.1 x 100 mm, 3.5u Zorbax Stablebond 300-C8 column from Agilent, the temperature was 50°C, and the flow rate was 0.2ml/min. The injection volume was 2 µL. The LC mobile phases consist of 0.1% formic acid in water and 0.1% formic acid in acetonitrile. Spectra were collected in full scan MS mode with a mass range of 600-4000 Da and collision RF setting of 800 Vpp.

Protein Crystallization and Crystallography

Crystallization was carried out based on the hanging drop method using VDX Plates with sealant (Hampton Research). Each well was loaded with 0.5 mL reservoir solution. 1 µL of protein solution was added onto a Fisherbrand unbreakable cover slip (Fisher Scientific). This was repeated to form two initial drops. Into each drop was added 1 µL of reservoir solution. The cover slips were flipped and sealed onto the wells. The plates were left at RT (296 K). When seeding was implemented, the cover slip was unsealed after 20 h. Microcrystals in a seed stock were transferred using a cat whisker. The whisker was streaked through the two drops consecutively without reloading. Afterwards, the cover slip was re-sealed onto the well. Crystals grew at RT.

Seed- α : TEM-1-native solution was prepared in 50 mM KPi (pH 7.0) at a concentration of 20 mg/mL. The reservoir solution contains 0.1 M HEPES (pH 7.5) and 2.0 M ammonium sulfate.

Clusters of small needle crystals appeared after 2 days. The crystals were collected and fragmented using ceramic beads and diluted 1000-fold with the reservoir solution as the stock of seed-*a*.

Seed-*b*: TEM-1-native solution was prepared in 50 mM KPi (pH 7.0) at a concentration of 10 mg/mL. The reservoir solution contains 0.1 M HEPES (pH 7.0) and 1.8 M ammonium sulfate. The drops were seeded with **seed-*a***. Clusters of small needle crystals appeared after 7 days. The needle crystals disappeared, and thin plate crystals emerged after 14 days. The crystals were collected and fragmented using ceramic beads and diluted 1000-fold with the reservoir solution as the stock of seed-*b*.

Seed-*c*: TEM-1-native solution was prepared in 50 mM KPi (pH 7.0) at a concentration of 20 mg/mL. The reservoir solution contains 0.1 M HEPES (pH 7.0) and 1.6 M ammonium sulfate. The drops were seeded with **seed-*a***. Needle crystals appeared after 14 days. The crystals were collected and fragmented using ceramic beads and diluted 100-fold with the reservoir solution as the stock of seed-*c*.

WT: TEM-1-native solution was prepared in 10 mM HEPES (pH 7.0) at a concentration of 20 mg/mL. The reservoir solution contains 50 mM HEPES (pH 7.0), 50 mM KPi (pH 7.0) and 1.6 M ammonium sulfate. The drops were seeded with **seed-*b***. Thin plate crystals appeared after 1 month and were harvested for diffraction measurements.

A237Y: A better crystallization condition was found. TEM-1-native-A237Y solution was prepared in 10 mM HEPES (pH 7.0) at a concentration of 20 mg/mL. The reservoir solution contains 25% or 27.5% PEG3350 (Hampton Research). The drops were seeded with **seed-*c***. Thicker plate crystals appeared after 7 days and were harvested for diffraction measurements. This condition was also used to obtain WT crystals for AVB binding.

WT–AVB, A237Y–AVB: For obtaining structures with bound AVB, the crystals were soaked in reservoir solution containing 2 mM AVB for 24 h before dipping into the cryoprotectant.

Single crystals were looped and dipped into the cryoprotectant (reservoir solution supplemented with 28% ethylene glycol) before flash cooling in liquid nitrogen. The X-ray diffraction data were collected at 100 K at the Stanford Synchrotron Radiation Lightsource (Menlo Park, CA) at beamline BL12-2. The room-temperature structures were measured at beamline BL12-1. The data were indexed, reduced, and scaled using X-ray Detector Software (XDS)⁶. The structures were solved using the Molecular Replacement Module in PHENIX⁷, where the initial model was a published structure of the M182T mutant of TEM-1 (PDB: 1jwp)⁸. Several rounds of manual and automatic structure refinement were performed using COOT⁹ and PHENIX. The resulting data collection and refinement statistics are summarized in Tables S4-S8.

Protein ¹H-NMR

Protein samples of the A237Y and A237Y^c mutants of TEM-1 were prepared by exchanging 3 mg of the proteins into 500 μ L of a buffer containing 20 mM KPi at pH 6.0 with 10% D₂O. The protein concentration is \sim 0.2 mM. Proton nuclear magnetic resonance (¹H-NMR) spectra were

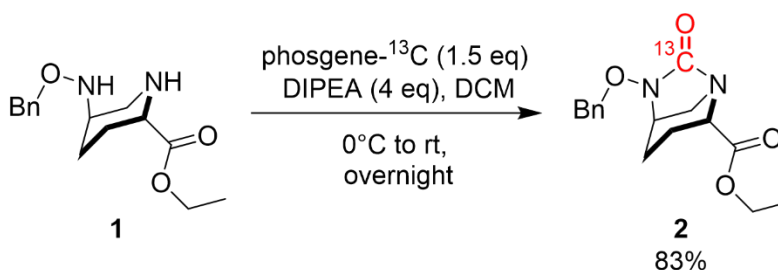
recorded on a Varian Inova 600 MHz spectrometer with a 5 mm Z-gradient HCN probe. The spectra were acquired at 15 °C. Water suppression was achieved using the WET method¹⁰. The data were processed with MestReNova software using a line-broadening parameter of 2 Hz. The spectra are shown in Figures S9-S11.

Synthesis of Avibactam-¹³C

(2*S*,5*R*)-Ethyl 5-((benzyloxy)amino)piperidine-2-carboxylate (**1**) oxalate was purchased from ChemScene LLC. *N,N*-Diisopropylethylamine, phosgene-¹³C solution (99 atom % ¹³C, 20% in toluene), anhydrous sodium sulfate, tetrahydrofuran, lithium hydroxide monohydrate, methanol-*d*₄ (99.8 atom % D), isobutyl chloroformate, palladium on carbon (10 wt.% loading), *n*-butyl acetate, acetic acid, and 4-methyl-2-pentone were purchased from Sigma-Aldrich. Dichloromethane (extra dry) and CDCl₃ (99.8 atom % D) were purchased from Acros Organics. Ethyl acetate, hexanes, phosphoric acid, sodium bicarbonate, sodium chloride, hydrogen chloride, ammonium hydroxide, methanol, isopropanol, and dichloromethane were purchased from Fisher Scientific. Triethylamine was purchased from Millipore. Sulfur trioxide trimethylamine complex was purchased from Matrix Scientific. Tetrabutylammonium acetate was purchased from Alfa Aesar.

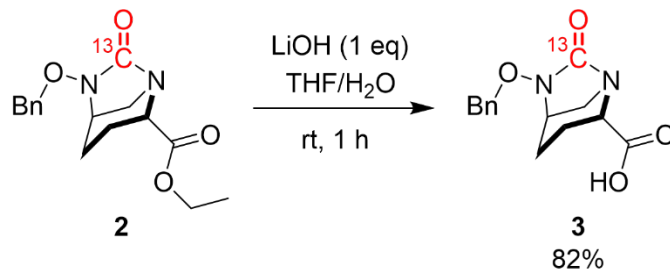
¹H-NMR spectra were recorded on a Varian VNMRS-400 MHz instrument and are reported in ppm using solvent as an internal standard (CDCl₃ at 7.26 ppm, CD₃OD at 3.31 ppm). Proton-decoupled carbon nuclear magnetic resonance spectra (¹³C-NMR) were recorded on a Varian VNMRS-400 MHz instrument and are reported in ppm using solvent as an internal standard (CDCl₃ at 77.16 ppm). Mass spectra were recorded on a Waters Single Quadrupole Mass Spectrometer at the Stanford University Mass Spectrometry facility. ESI was performed under a low cone voltage. The mass was recorded in both positive and negative modes in the range of 50-2000 *m/z*.

The overall synthesis route for AVB-¹³C is shown in Figure S15.

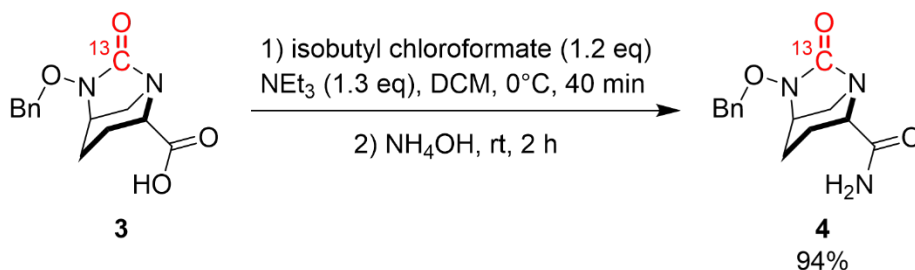


(2*S*,5*R*)-Ethyl 6-(benzyloxy)-7-oxo-1,6-diazabicyclo[3.2.1]octane-2-carboxylate-¹³C (**2**)¹¹: A solution of **1** oxalate (100 mg, 0.27 mmol) and *N,N*-diisopropylethylamine (188 μL, 1.08 mmol) in anhydrous dichloromethane (DCM, 2 mL) was cooled to 0°C under argon. A solution of phosgene-¹³C (20%, 99 atom% ¹³C) in toluene (234 μL, 0.41 mmol) was added dropwise. The reaction mixture was stirred at room temperature overnight, and the progress was monitored by thin layer chromatography (TLC) using EtOAc/hexanes (1:1, with 0.1% triethylamine). The

reaction mixture was washed with H₃PO₄ (10%) twice, sat. NaHCO₃ twice, and brine. The organic layer was dried over anhydrous Na₂SO₄, concentrated under reduced pressure, and dried under vacuum, affording **2** (69 mg, 83%) as a white solid. ¹H-NMR (400 MHz, CDCl₃) as shown in Figure S16: δ 7.40-7.31 (m, 5H), 5.01 (dd, *J* = 11.5, 2.8 Hz, 1H), 4.86 (dd, *J* = 11.5, 2.6 Hz, 1H), 4.20 (qd, *J* = 7.2, 2.3 Hz, 2H), 4.07-4.04 (m, 1H), 3.32-3.28 (m, 1H), 3.05-3.00 (m, 1H), 2.90 (ddd, *J* = 11.8, 6.4, 2.3 Hz, 1H), 2.09-2.01 (m, 2H), 2.00-1.97 (m, 1H), 1.68-1.59 (m, 1H), 1.28-1.23 (td, *J* = 7.2, 3.0 Hz, 3H); ¹³C-NMR (100 MHz, CDCl₃) as shown in Figure S17: δ 168.08 (strong), 168.05, 135.68, 129.20, 128.68, 128.48, 78.20, 61.60, 59.65, 58.22, 47.39, 21.12, 19.89, 14.12.

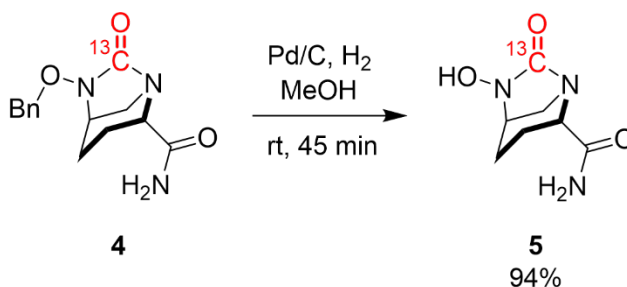


(2S,5R)-6-(benzyloxy)-7-oxo-1,6-diazabicyclo[3.2.1]octane-2-carboxylic acid-¹³C (3)¹¹: To a solution of **2** (150 mg, 0.49 mmol) in tetrahydrofuran (3 mL) was added dropwise LiOH·H₂O (20.6 mg, 0.49 mmol) in water (1 mL). The reaction mixture was stirred at room temperature and monitored by TLC using EtOAc/hexanes (1:1, with 0.1% triethylamine). After the precursor disappeared (~1 h), the reaction mixture was washed with EtOAc twice, and then the aqueous solution was adjusted to pH = 3 with 1N HCl. The resulting mixture was extracted with DCM three times. The combined organic layer was dried over anhydrous Na₂SO₄, concentrated under reduced pressure, and dried under vacuum, affording **3** (112 mg, 82%) as a white solid. ¹H-NMR (400 MHz, CDCl₃) as shown in Figure S18: δ 7.44-7.37 (m, 5H), 5.06 (d, *J* = 11.3 Hz, 1H), 4.91 (d, *J* = 11.3 Hz, 1H), 4.16 (d, *J* = 7.1 Hz, 1H), 3.42-3.38 (m, 1H), 3.18 (d, *J* = 11.8 Hz, 1H), 2.92 (dd, *J* = 11.9, 6.4 Hz, 1H), 2.26-2.21 (m, 1H), 2.11-2.01 (m, 2H), 1.72-1.63 (m, 1H); *m/z* (ESI-MS) 276.1 [M - H]⁻.

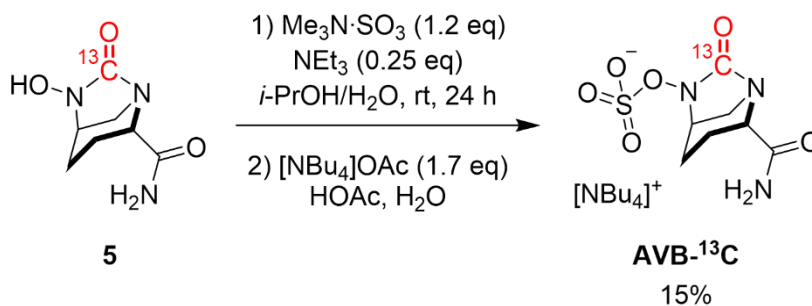


(2S,5R)-6-(Benzyloxy)-7-oxo-1,6-diazabicyclo[3.2.1]octane-2-carboxamide-¹³C (4)¹²: A solution of **3** (112 mg, 0.40 mmol) and triethylamine (74 μL, 0.53 mmol) in DCM (2 mL) was cooled to 0°C under argon. Isobutyl chloroformate (67 mg, 0.49 mmol) was added quickly to the mixture, followed by stirring at 0°C for 40 min. Aqueous ammonia (0.3 mL) was added slowly to the reaction mixture, followed by stirring at room temperature for 2 h. Subsequently, water (10

mL) was added, and the organic layer was separated and washed with water and brine. The organic layer was dried over anhydrous Na_2SO_4 and concentrated under reduced pressure. The residue was applied to silica gel column chromatography using methanol/DCM (1:20) to afford **4** (105 mg, 94%) as a white solid. $^1\text{H-NMR}$ (400 MHz, CDCl_3) as shown in Figure S19: δ 7.44-7.37 (m, 5H), 6.63 (s, 1H), 5.75 (s, 1H), 5.04 (dd, $J = 11.4, 0.3$ Hz, 1H), 4.89 (d, $J = 11.5$ Hz, 1H), 3.94 (d, $J = 7.6$ Hz, 1H), 3.32-3.27 (m, 1H), 3.02 (d, $J = 11.7$ Hz, 1H), 2.76 (dd, $J = 11.6, 6.4$ Hz, 1H), 2.33 (dd, $J = 13.9, 6.6$ Hz, 1H), 1.96-1.85 (m, 2H), 1.63-1.55 (m, 1H); $^{13}\text{C-NMR}$ (100 MHz, CDCl_3) as shown in Figure S20: δ 168.22, 167.48 (strong), 135.72, 129.36, 128.96, 128.71, 78.44, 60.57, 58.01, 47.92, 20.97, 17.39; m/z (ESI-MS) 277.2 $[\text{M} + \text{H}]^+$.



(2S,5R)-6-hydroxy-7-oxo-1,6-diazabicyclo-[3.2.1]octane-2-carboxamide- ^{13}C (5): To a solution of **4** (95 mg, 0.34 mmol) in methanol (3.5 mL) was added palladium on carbon (17 mg, 10 wt.% loading), followed by stirring under H_2 atmosphere. The reaction was monitored by TLC using methanol/DCM (1:20) and took ~45 min for the complete consumption of the precursor. The reaction mixture was filtered through celite, concentrated under reduced pressure, and dried under vacuum, affording **5** (60 mg, 94%) as a white solid. $^1\text{H-NMR}$ (400 MHz, CD_3OD) as shown in Figure S21: δ 3.85 (d, $J = 7.8$ Hz, 1H), 3.72-3.68 (m, 1H), 3.19-3.14 (m, 1H), 2.97 (dd, $J = 11.7, 6.4$ Hz, 1H), 2.27 (dd, $J = 15.0, 6.9$ Hz, 1H), 2.09-2.04 (m, 1H), 1.93-1.87 (m, 1H), 1.77-1.69 (m, 1H).



Tetrabutylammonium [(2S,5R)-2-Carbamoyl-7-oxo-1,6-diazabicyclo[3.2.1]octan-6-yl] Sulfate- ^{13}C (AVB- ^{13}C) 13 : **5** (60 mg, 0.32 mmol) was mixed with sulfur trioxide trimethylamine complex (53.6 mg, 0.39 mmol) in isopropanol (2 mL) and water (2 mL). Triethylamine (11.2 μL , 0.08 mmol) was added to the reaction mixture, followed by stirring at room temperature for 24 h. The reaction mixture was washed with *n*-butyl acetate, from which the aqueous phase was collected. A solution of tetrabutylammonium acetate (163 mg, 0.54 mmol) and acetic acid (2 μL)

in water (400 μ L) was prepared. Next, 300 μ L of the tetrabutylammonium acetate solution was added to the reaction mixture, which was then extracted with 2 mL of DCM. The remaining 100 μ L of the tetrabutylammonium acetate solution was added to the aqueous phase, which was then extracted with 2 mL of DCM. The organic extracts were combined, concentrated under reduced pressure, and dried under vacuum, affording a crude product (189 mg) containing ~42 wt.% AVB- 13 C (49% yield), the rest being tetrabutylammonium acetate and residual solvents. The crude product was recrystallized from 4-methyl-2-pentanone by cooling to 0°C to precipitate the desired product. The product was collected by filtration, washed with 4-methyl-2-pentanone, and dried under vacuum, affording white crystalline solids of AVB- 13 C (24 mg, 15%). 1 H-NMR (400 MHz, CDCl₃) as shown in Figure S22: δ 6.72 (s, 1H), 5.59 (s, 1H), 4.36 (s, 1H), 3.92 (d, J =7.8 Hz, 1H), 3.38 (d, J = 11.7 Hz, 1H), 3.32-3.27 (m, 8H), 2.87 (dd, J = 11.5, 6.5 Hz, 1H), 2.39 (dd, J = 15.0, 7.0 Hz, 1H), 2.20-2.14 (m, 1H), 1.92-1.82 (m, 1H), 1.71-1.62 (m, 9H), 1.49-1.40 (m, 8H), 1.00 (t, J = 7.4 Hz, 12H); 13 C-NMR (100 MHz, CDCl₃) as shown in Figure S23: δ 165.67 (strong), 60.61, 58.83, 57.93, 48.27, 24.08, 20.87, 19.83, 17.37, 13.81; m/z (ESI-MS) 508.8 [M + H]⁺, 265.0 [M – NBu₄]⁺; FTIR, see Figure S24.

Calibration of Vibrational Stark Probes

Overview: Instead of directly using AVB for probe calibration, we employed (2S,5R)-6-(Benzyloxy)-7-oxo-1,6-diazabicyclo[3.2.1]octane-2-carboxamide (BODAC), the counterpart of **4** without 13 C labeling, as a model compound which replaces the charged sulfate of AVB with a neutral benzyloxy group to avoid overestimation of electric fields in MD simulations (Figure S12, Tables S10 and S11)¹⁴. When AVB is covalently linked to S70, its urea C=O is converted to a carbamate C=O (Figure 2b), whose frequency sensitivity to electric field was separately calibrated using methyl piperidine-1-carboxylate (MPC), a simple, rigid carbamate, as an ideal model compound (Figures S13 and S14, Tables S12-S14).

In Figure 3f-h, the top electric field axes are mapped from the bottom frequency axes according to the calibration results: $\bar{\nu} = 0.76F + 1779.8$ (f) based on BODAC; $\bar{\nu} = 0.75F + 1714.0$ (g) based on MPC; $\bar{\nu} = 0.78F + 1796.8$ (h) based on penam¹⁴. $\bar{\nu}$ is the wavenumber (cm⁻¹) of the C=O vibrations, and F is the magnitude of active-site electric fields (MV/cm) projected on the C=O.

Materials: BODAC was purchased from Enovation Chemicals. MPC was purchased from AA Blocks. All organic solvents were obtained from Sigma-Aldrich (anhydrous and at > 99% purity). D₂O (99 atom % D) was obtained from Cambridge Isotope.

FTIR Spectroscopy—Vibrational Solvatochromism: BODAC and MPC were dissolved in organic solvents and D₂O at a concentration of 10 mM. In cases where solubility became a limiting factor, a saturated solution was prepared and diluted by a factor of least 2 before injection into the cell, in order to prevent solute aggregation. Six organic solvents of varying polarity were chosen: hexanes, dibutylether, tetrahydrofuran (THF), toluene, dimethylsulfoxide (DMSO), dichloromethane (DCM). The exception is that BODAC has only trace solubility in hexanes and no absorption peaks were obtained for this combination.

Infrared spectra were recorded using a Bruker Vertex 70 equipped with a liquid nitrogen-cooled mercury cadmium telluride detector and under constant purging of the sample chamber with dry air, similarly to previous works¹⁵. 20 μL of the samples were loaded into a demountable cell composed of two CaF_2 optical windows (19.05 mm diameter, 3 mm thickness, Lambda Research Optics). The windows were separated by two Teflon spacers, one 25 μm thickness and the other 50 μm . Before FTIR measurement, a 5 min delay was applied to purge gaseous CO_2 , and then 256 scans were acquired and averaged to obtain each transmission interferogram. Spectra were recorded in window of 4000–1000 cm^{-1} with 1 cm^{-1} resolution. Blank solvent spectra were recorded under the same condition and used as a reference for subtracting the background. Data collection and processing were performed using the software OPUS 5.0. Peak positions and the full width at half maximum (FWHM) were determined using the built-in programs PeakPick and CurveFit (combination of Lorentzian and Gaussian) in OPUS 5.0 (Tables S10 and S12).

Fixed-Charge MD Simulations: Fixed-charge MD simulations were carried out similarly to previous works^{14,16,17}. The molecule of interest was constructed in Gaussview 6.0, and the geometry was optimized by Density Functional Theory (DFT) in Gaussian 16 (ref.¹⁸) at the B3LYP/6-311++G(2d,2p) level. The resultant structure was then used for parameterization through the Antechamber program of AmberTools16 (ref.¹⁹) based on the GAFF force field. The force field parameters for organic solvents were taken from Caleman et al²⁰, and water was parameterized using the TIP3P model. All simulations were performed by GROMACS 2018 (ref.²¹). A single solute molecule was placed in the center of a cubic solvation box that has a size of $4 \times 4 \times 4 \text{ nm}^3$ filled with solvent molecules. Under periodic boundary conditions, the system was first energy minimized until the maximum force is less than 1000 kJ/mol/nm, followed by NVT and NPT equilibration runs (100 ps for each). MD production runs were performed over 1 ns with 2 fs steps, with a van der Waals cutoff of 10 \AA (with analytical VdW correction), an electrostatics cutoff of 10 \AA (using the particle mesh Ewald method), an SD (leap-frog stochastic dynamics) integrator, the Berendsen thermostat²² and the Parrinello-Rahman barostat²³. The electric field vectors on the relevant atoms (C and O) were obtained via dividing the electrostatic forces acting on these atoms by the corresponding atomic charges. To extract the solvent contributions to the electric fields, the MD frames obtained were recalculated with atomic charges on all solvent molecules zeroed out, providing the field contributions from the solute atoms themselves which were then subtracted from the electric field values obtained in the original production run. The electric field projections along the C=O directions are then evaluated using the following equation:

$$F_{\text{CO}} = \frac{1}{2} (\vec{F}_{\text{C}} \cdot \hat{r}_{\text{CO}} + \vec{F}_{\text{O}} \cdot \hat{r}_{\text{CO}})$$

where F_{CO} denotes the field projection along the C=O bond, \vec{F}_{C} and \vec{F}_{O} are the electric fields acting on the C and O atoms, respectively, and \hat{r}_{CO} refers to a unit vector along the direction of the C=O bond. The magnitudes of the fields projected on the C=O bond in BODAC and MPC are listed in Tables S11 and S13. The calibration of vibrational frequency against the calculated electric field is shown in Figures S12 and S13.

Vibrational Stark Spectroscopy: Vibrational Stark spectroscopy was carried out similarly to previous works^{24,25}. MPC was dissolved in 2-methyl tetrahydrofuran (Sigma-Aldrich), a glass-forming solvent, at a concentration of 50 mM. 10 μL of sample was injected into a Stark cell assembled using two offset CaF_2 optical windows (12.7 mm diameter, 1 mm thickness, FOCtek Photonics), which were coated with a 4.5 nm layer of nickel metal and separated by two Teflon

spacers ($\sim 26 \mu\text{m}$ thickness). The cell was immediately immersed into a custom-built cryostat²⁶ filled with liquid nitrogen. The Stark spectra were recorded by a Bruker Vertex 70 spectrometer at 1 cm^{-1} resolution for 64 scans in the presence and absence of an externally applied electric field, respectively. The external field ranged from 0.5 to 1.4 MV/cm, corresponding to 1.5 to 3.6 kV voltage, which was applied via a Trek 10/10 high-voltage power amplifier. Stark spectra were obtained by taking the difference between the field-on and field-off transmission spectra (Figure S14). The linear Stark tuning rates were obtained from the contribution of the second derivative of the low temperature absorbance spectrum to the Stark spectrum (Table S14)^{16,24}. The determined Stark tuning rate is reported as a product of the local field factor f , which reflects the difference between the applied electric field and the actual local electric field that is experienced by the vibrational probe, with the $|\Delta\mu|$ extracted from solvatochromism.

Isotope-Edited FTIR Spectroscopy

The TEM proteins were concentrated to a volume of 60 μL at a concentration of 2.3 mM using a 10,000 Da MWCO Amicon spin filter (Millipore). The proteins were then solvent exchanged with a D_2O buffer containing 100 mM NaCl and 50 mM KPi (pD 7.4) using Micro Bio-Spin P-6 gel column (Bio-Rad). The protein solution was allowed to sit at 4°C overnight for sufficient H-D exchange. Afterwards, the protein solution was solvent exchanged again with the D_2O buffer before splitting into two portions of equal volume ($\sim 30 \mu\text{L}$). The ligands (AVB or PenG), both ^{13}C -labeled and unlabeled, were prepared in the same D_2O buffer at a concentration of 25 mM, respectively. 4 μL of the ^{13}C -labeled and unlabeled ligand solution were added into each portion of the protein solution, respectively. The two samples were each mixed using pipette and spun down. For proteins of large K_M , 8 μL of the ligand solutions were used. The protein samples were directly used for FTIR measurements, except for A237Y^c-AVB, which was incubated at room temperature for 2 h, due to the slow formation of the covalent bond. Mass spectra were taken for samples of covalent complexes. These samples were quenched by using MeOH/ H_2O (1:1, v/v) both before and after the FTIR measurements, which confirmed the formation and stability of the covalent bonds (Table S3).

Infrared spectra were taken similarly to the protocol described in the section of *FTIR Spectroscopy—Vibrational Solvatochromism*, except for the following differences. The dry air purging was carried out for 10 min. 512 scans were acquired on the interferometer and averaged. Nine spectra were collected for each sample. For every three spectra, the sample cell mounted on the cell holder was rotated by 120° . The FTIR spectra of free AVB and Pen-G, both ^{13}C -labeled and unlabeled, were also collected for use as references, including AVB sodium (AVB-Na, Advanced ChemBlocks), AVB tetrabutylammonium (AVB-NBu₄, synthesized from BODAC using the same protocol in the section of *Synthesis of ^{13}C -Avibactam*), AVB- ^{13}C -NBu₄ (Figure S24 and Table S15), PenG sodium (Sigma Aldrich), and PenG- ^{13}C (ref.²⁷).

The procedure for data processing has been described in detail in previous works³. Briefly, the raw transmission spectra were converted to absorption spectra. To remove protein background, difference FTIR spectra were generated by subtracting the protein spectra of the ^{13}C -labeled ligand from that of the unlabeled one. A scaling factor close to unity was typically used to compensate for slight differences in sample concentration and pathlength. The resulting spectra were further

processed by removing the broad peaks associated with the unbound, free ligands, and the weak, broad peaks associated with protein amide backbone experiencing H-D (back) exchange. The latter were obtained by taking the difference from the 9 spectra of the same sample (either the ^{13}C -labeled or the unlabeled). Finally, the spectra were baselined guided by the offset ($35\text{-}55\text{ cm}^{-1}$) between the positive and negative peaks, the frequency shift due to ^{13}C -labeling. This process was repeated for the 9 spectra taken for each sample to ensure consistency. To deconvolve the difference spectra where positive ^{12}C peaks overlap with the negative ^{13}C peaks, the difference spectra was fitted into component peaks as Gaussian-Lorentzian sums²⁸, using a script we wrote (Script 1).

In parallel to the half-manual-half-automatic procedure, we further wrote a script (Script 2) that can perform the whole procedure from spectrum subtraction, baselining, all the way to peak fitting. In this way, human bias can be minimized, especially when peak fitting is sensitive to the choice of baselines. We used this script to analyze the spectra for TEM-AVB, which have high intensity of the difference spectra and thus are suitable for the fully automated data processing. All the nine ^{12}C spectra and nine ^{13}C spectra were loaded into the script, generating nine difference spectra, which are all used as the input for the fitting program. The fitting generated nine baselines, each for one difference spectra, and a single set of ^{12}C and ^{13}C peaks as Gaussian-Lorentzian sums.

Polarizable MD Simulations of Proteins

Protein and ligand preparation: A total of 5 protein/ligand complexes, WT TEM•AVB, WT TEM-AVB, WT TEM•PenG, A237Y TEM•PenG, and A237Y^e TEM•PenG were modeled for molecular docking and molecular dynamics simulations. We chose the crystal structure of AVB covalently bound to WT TEM-1-native (PDB: 8DE0) as the template. We used the Mutate Residue function in the Maestro²⁹ Build menu to introduce the T182M and A184V mutations to match the amino acid sequences of the models with those of the proteins measured by FTIR. To create the non-covalent complexes, the covalently bound AVB was deleted, followed by the S70G mutation. Non-covalently bound AVB was built using the 2D-builder in Maestro. Non-covalently bound PenG was extracted from the crystal structure 1FXV³⁰. Both ligands were minimized using the OPLS4 force field³¹ in Macromodel before docking. To make the A237Y^e mutant of TEM•PenG, atom point mutation was used to convert the corresponding amide in A237Y to an ester.

Molecular docking and fixed-charge molecular dynamics simulations: AVB and PenG were manually docked into the oxyanion hole in the TEM binding pockets, ensuring optimal distance between the carbonyl oxygen and the S70G and A237 or A237Y amides. To reduce steric clashes between the docked ligands and the proteins in both the non-covalently and the covalently bound complexes, they were minimized using Macromodel. The systems were then solvated with TIP3P waters and neutralized with Na^+ in an optimized truncated octahedron with a 10 Å buffer distance between protein and boundary. Each complex was subjected to minimization and heating according to the built-in protocol in Desmond, and five replicates of 100 ns molecular dynamics simulations using the OPLS4 force field and the NPT ensemble at 298 K.

The distances between carbonyl oxygen and amide nitrogen were measured and plotted for all simulation trajectories. Trajectories where these distances were stable throughout the

simulation were manually inspected and single frames were chosen as starting structures for the following simulations.

Polarizable molecular dynamics simulations: Polarizable molecular dynamics simulations were performed using Tinker9 (ref.³²) using the AMOEBA18 force field^{33,34}. The ligands, PenG and AVB, as well as the residues of A237Y^e, the glycine adjacent to A237Y^e, and the serine-AVB covalent adduct were parameterized using Polype2 (ref.³⁵). Electrostatic parameters were obtained from fitting the electrostatic potential of 6 conformers at the MP2/aug-cc-ptvz level, and torsion parameters were refined based on dihedral scans at the WB97x-d/6-311+g* level of theory with steps of 20–30° (depending on the number of parameters to be fit). The residues of A237Y^e, the glycine adjacent to A237Y^e, and the serine-AVB covalent adduct were capped using acetyl and dimethyl amine groups with parameters taken from the AMOEBA18 force field (kept fixed during the parameterization) to ensure compatibility with the force field. For the serine-AVB covalent adduct, AMOEBA18 parameters were used to describe the entire capped serine backbone, while the parameters for the sidechain were refined. To ensure that the residues of A237Y^e and the serine-AVB covalent adduct carry a total charge of 0 and -1, respectively, the charge of C α atoms was adjusted (by ca. ± 0.05). Structures from fixed-charge molecular dynamics were minimized and equilibrated as NVT (Bussi thermostat; Ewald and vdw cutoffs of 7 and 12 Å; induced dipole threshold of 10^{-4} D; 1 fs steps) and NPT (Monte Carlo barostat; otherwise, similar conditions) ensembles for 500 ps each. Three production runs were performed over 10 ns for each system. Electric fields along the β -lactam C=O bond were determined as the averaged fields on the C and O atoms projected along the C=O bond axis, as reported previously¹⁴.

Kinetic Measurement on PenG Hydrolysis by β -Lactamases

Overview: The rate of PenG acylation (k_{ac}) was determined by first fitting full-time kinetic data to the integrated Michaelis-Menten equation^{36,37} (Figure S32), followed by decoupling k_{ac} from k_{cat} using steady-state MS (ref.³) (Figure S33).

Full-Time Kinetics for Obtaining k_{cat} and K_M : Conventional Michaelis-Menten kinetic measurements require multiple steady-state reactions with varying substrate concentrations. For each reaction, only the initial slope is used, and the rest of the data is wasted. k_{cat} and K_M can be extracted from a single run of the reaction because the concentration vs time function is just the integrated form of the rate vs concentration function (see below), and thus also fully governed by k_{cat} and K_M (ref.^{36,37}). However, using the integrated function in an explicit form requires access to the Lambert function (W), which is only recently incorporated into data processing software such as Matlab³. A full-time kinetic measurement that runs all the way to completion, although seldomly used, offers great advantages over conventional Michaelis-Menten kinetics, including fewer reactions to be run and more robust data fitting³⁸ against hundreds of data points that can be easily collected by measuring the concentration over time. The only requirement of full-time kinetics is that the reaction has to start from a substrate concentration at least comparable to K_M and continues until the substrate is fully exhausted. Therefore, the reaction cannot be too slow (reasonable k_{cat}/K_M) so that the data can be collected in a practical period. In the following we recapitulate the derivation^{36,37} in order to define parameters that are derived and connect to the reactions described in this manuscript.

To derive the integrated form of the Michaelis-Menten equation, consider a typical enzymatic reaction:



where E is the enzyme, S is the substrate, E•S is the Michaelis complex, and P is the product. The rate of the reaction, v , can be expressed as:

$$v = -\frac{d[S]}{dt} = \frac{k_{\text{cat}}[E]_0[S]}{K_M + [S]} \quad \text{eq.2,}$$

where $[E]_0$ is the initial concentration of the free enzyme, t is time, K_M , the Michaelis constant, equals to k_{-1}/k_1 . If we integrate eq. 2, we will obtain:

$$K_M \ln \left(\frac{[S]_0}{[S]_t} \right) + [S]_0 - [S]_t - k_{\text{cat}}[E]_0 t = 0 \quad \text{eq. 3,}$$

where $[S]_0$ is the initial concentration of the substrate, and $[S]_t$ is the concentration of the substrate at time t . If we rearrange all the terms involving $[S]_t$ to the left side and t to the right side, we obtain:

$$\frac{[S]_t}{K_M} + \ln \frac{[S]_t}{K_M} = \ln \left(\frac{[S]_0}{K_M} e^{\frac{[S]_0 - k_{\text{cat}}[E]_0 t}{K_M}} \right) \quad \text{eq. 4.}$$

To solve $[S]_t$ as a function of t , we need to write this equation in a closed form. This requires using the Lambert function $W(x)$, which satisfies:

$$W(x) + \ln(W(x)) = \ln(x) \quad \text{eq. 5.}$$

If we let x to be the term in $\ln()$ on the right side of eq. 4, $W(x)$ becomes $[S]_t/K_M$:

$$[S]_t = K_M W \left(\frac{[S]_0}{K_M} e^{\frac{[S]_0 - k_{\text{cat}}[E]_0 t}{K_M}} \right) \quad \text{eq. 6.}$$

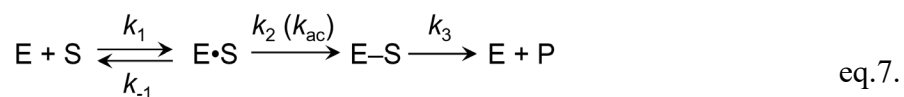
Now there is only one term involving $[S]_t$ on the left side, so $[S]_t$ can be determined at any t given known values of k_{cat} and K_M . Conversely, if we measure the change of substrate concentration ($[S]_t$) over time (t), we can fit the data to eq. 6 and obtain k_{cat} and K_M .

TEM-1 β -lactamases were prepared in 50 mM potassium phosphate (KPi, pH 7.0) and their concentrations were determined using the absorbance at 280 nm measured by a Lambda 365 (Perkin-Elmer) UV-Vis spectrometer. The extinction coefficients are listed in Table S3. The TEM-1 samples were then diluted into a reaction buffer containing 0.02% (w/v) bovine serum albumin (BSA) and 50 mM KPi (pH 7.0). The dilution fold was chosen such that the hydrolysis reactions to be run can finish in a suitable period (longer than 10 s but shorter than 10 min). BSA in the reaction buffer acts to passivate the surfaces of cuvettes and mixing tubing, thus minimizing the adhesion of the TEM-1 β -lactamases. PenG (Sigma-Aldrich) solutions were also prepared in the reaction buffer. The final concentration of PenG was chosen at least 2-fold higher than the estimated K_M .

The hydrolysis reaction was monitored on a Cary 6000i UV-Vis-NIR spectrometer equipped with a stopped-flow accessory (SFA-20 Rapid Mixing Accessory), which is not always necessary but makes fast reactions (< 1 min) convenient to measure. Prior to use, all cuvettes and mixing tubing were passivated with a solution containing 0.1% (w/v) BSA and 50 mM KPi (pH 7.0) for at least 30 min before washing with the reaction buffer. The TEM-1 solution and the PenG solution were loaded into the syringes of the stopped-flow accessory and quickly mixed in the cuvette. The consumption of PenG during the reaction was monitored at 232 nm ($\Delta\epsilon_{232} = -940 \text{ M}^{-1} \text{ cm}^{-1}$)³⁹ every 0.2 s until completion of the reaction. The experiment from mixing to monitoring was repeated 5 times.

With the measured time-dependent change in PenG concentration, k_{cat} and K_M were determined using the closed-form (explicit) solution to the integrated Michaelis-Menten equation (eq. 6), which utilizes the Lambert function. The corresponding Matlab script is presented in our previous work³. A modified script that automatically reads the initial substrate concentration and makes an initial guess for k_{cat} and K_M is provided in Script 3. Note that the final concentration of TEM-1 should be half of that of the prepared TEM-1 samples due to the 1:1 mixing with the PenG solutions. An example of data fitting for PenG hydrolysis by the WT is shown in Figure S32. The average and standard deviation are based on 5 repeats and presented in Table S1.

Steady-State Mass Spectrometry for Obtaining k_{ac} and k_3 : PenG hydrolysis by class A β -lactamases follows a two-step mechanism:



After formation of the Michaelis complex, TEM•PenG (E•S), PenG first acylates Ser70 in β -lactamases, producing a covalent acyl complex, TEM–PenG (E–S), which is then hydrolyzed to give the product and the regenerated β -lactamases. k_2 is the rate constant of acylation, also referred to as k_{ac} in the main text. k_3 is the rate constant of deacylation.

The relationship between k_2 , k_3 , and k_{cat} is:

$$k_{\text{cat}} = \frac{k_2 k_3}{k_2 + k_3} \quad \text{eq. 8.}$$

In steady state, the concentration of E–S stays constant, meaning that its formation and conversion have the same rate:

$$k_2[\text{E}\cdot\text{S}] = k_3[\text{E}-\text{S}] \quad \text{eq. 9.}$$

Bringing eq. 9 into eq. 8, we obtain:

$$k_2 = k_{\text{cat}} \left(1 + \frac{[\text{E}-\text{S}]}{[\text{E}\cdot\text{S}]} \right) \quad \text{eq. 10.}$$

To deconvolve k_{cat} into k_2 and k_3 , the molar ratio between E–S and E•S in steady state was measured using mass spectrometry (Figure S33). To prepare a steady state that can last long

enough for manual mixing and quenching (ideally > 20 s), the concentrations of TEM-1 and PenG were carefully chosen according to the determined k_{cat} values. For example, the WT was prepared in 500 mM KPi buffer (pH 7.0) at a concentration of 10 mg/mL. 5 μ L of the TEM-1 solution was diluted with 450 μ L of 500 mM KPi (pH 7.0), into which 450 μ L of 200 mM PenG in 500 mM KPi (pH 7.0) was quickly added and mixed by pipette. Immediately, 900 μ L of methanol was added into the reaction mixture to quench the steady state on time. A 1:1 (v/v) mixture of methanol and water is effective to rapidly denature TEM-1 and keeps it denatured without turning over PenG substrate. It is important to use a high concentration of PenG in a small volume rather than a low concentration in a big volume, because high concentrations minimize (1) the impact of diffusion and (2) the free enzyme's concentration which leads to overestimation of the non-covalent complex's concentration.

Afterwards, the mixture was diluted into 40 mL of methanol/water (1:1, v/v) and concentrated into a final volume of 50 μ L using a 3,000 Da MWCO Amicon spin filter (Millipore). The purpose of this step is to reduce the concentration of PenG in the final sample for mass spectrometry, because a high concentration of PenG enables the acylation of even denatured proteins during UPLC/ionization, leading to artificial enhancement of the covalent complex. The dilution before the concentration is necessary because it brings KPi's concentration down, otherwise the denatured proteins tend to leak through the spin filter membrane. Finally, the denatured proteins are in a suitable concentration (33 μ M) for mass spectrometry. Three independent samples were prepared for each mutant. The above protocol was optimized based on previous works^{3,40}.

In the deconvoluted mass spectra, the ratio between non-covalent and covalent complexes (mass listed in Table S3) was quantified based on their peak area in the deconvoluted mass spectra (Figure S33 as an example of WT) and averaged over three independent repeats. The bootstrapping method for determining the median and confidence intervals of k_2 and k_3 was presented in our previous work³ (see "RateDistribution.m") and the results are displayed in Table S1.

Kinetic Measurement on AVB Inhibition of β -Lactamases

Overview: k_{cbm} is for the first time determined separately from the second-order rate constant k_{cbm}/K_i by using the stopped-flow technique (Figure S34) to record the initial rate of substrate turnover in the inhibition assay^{41,42} (Figures S35-S37). k_{rec} was obtained from the final rate of substrate turnover when the formation of TEM-AVB reaches equilibrium, rather than being estimated by k_{off} as in prior literature⁴³ (Text S5).

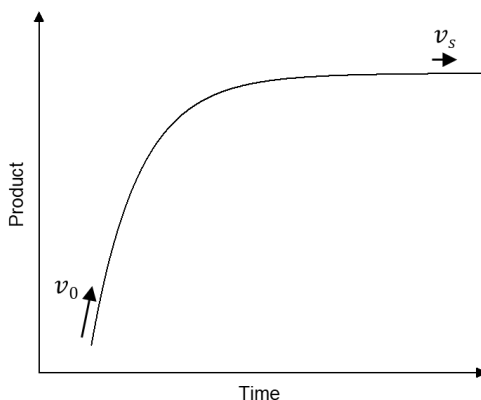
Mechanism of Covalent Inhibition: Avibactam (AVB) inhibits TEM β -lactamases by fast binding to the active site, forming a non-covalent complex, TEM•AVB (E•I, where I stands for the inhibitor), which is followed by slow formation of a covalent bond with S70. The generated carbamoyl complex, TEM-AVB (E-I), can undergo a reverse reaction to regenerate the non-covalent E•I complex; however, the equilibrium highly favors the covalent side. The mechanism can be written as:



where k_5 is the rate constant of carbamylation, equivalent to k_{cbm} used in the main text, and k_{-5} is the rate constant of recyclization, equivalent to k_{rec} used in the main text. The equilibrium constant for the non-covalent binding is K_i , following $K_i = k_{-4}/k_4$, similar to the K_i for non-covalent inhibitors and K_M for substrates. The overall dissociation constant, K_i^* follows:

$$K_i^* = \frac{[E][I]}{[E \cdot I] + [E-I]} = \frac{K_i k_{-5}}{k_5 + k_{-5}} \quad \text{eq. 12.}$$

The kinetics of covalent inhibition have been thoroughly studied in the literature⁴². Here we recapitulate the derivation and present the equations specific to the kinetic behavior of AVB. To measure AVB inhibition kinetics, a substrate is mixed with AVB sodium (Advanced ChemBlocks), and then together mixed with β -lactamases. The real-time rate of the substrate's conversion to product (eq. 1) characterizes the amount of the β -lactamases that has not been inhibited by AVB yet and is still available at that moment. The slowing down of product formation over time describes the progression of AVB inhibition:



The product-time trace can be written as⁴²

$$[P] = v_s t + \frac{(v_0 - v_s)(1 - e^{-k_{obs}t})}{k_{obs}} \quad \text{eq. 13,}$$

where v_0 stands for the initial rate and v_s for the final rate of product formation. The physical meaning of k_{obs} is clearer in the derivative form of eq.13:

$$\frac{d[P]}{dt} = v_s + (v_0 - v_s)e^{-k_{obs}t} \quad \text{eq. 14.}$$

Eq. 14 shows an exponential decay of the rate in product formation from the initial rate v_0 to the final rate v_s . k_{obs} is the constant for how fast the exponential decay is.

The initial rate v_0 is the highest rate during the reaction time course because no E-I has been generated. At that moment, the concentration of the total enzyme, $[E]_0$, is partitioned between that of E·I, E·S, and the free enzyme E. The proportion of E·S in the total enzyme dictates the rate in production formation:

$$v_0 = k_{cat}[E]_0 \frac{[E \cdot S]}{[E] + [E \cdot I] + [E \cdot S]} \quad \text{eq. 15.}$$

Given that:

$$\frac{[E \cdot S]}{[E] + [E \cdot I] + [E \cdot S]} = \frac{\frac{[S]}{K_M}}{1 + \frac{[I]}{K_i} + \frac{[S]}{K_M}} \quad \text{eq. 16,}$$

we obtain:

$$v_0 = k_{\text{cat}}[E]_0 \frac{\frac{[S]}{K_M}}{1 + \frac{[I]}{K_i} + \frac{[S]}{K_M}} \quad \text{eq. 17.}$$

The rate reaches the final rate v_s when the equilibrium between $E \cdot I$ and $E-I$ is established. Now the total enzyme has to be additionally partitioned into $E-I$, along with $E \cdot I$, $E \cdot S$, and the free enzyme:

$$v_s = k_{\text{cat}}[E]_0 \frac{[E \cdot S]}{[E] + [E \cdot I] + [E-I] + [E \cdot S]} \quad \text{eq. 18.}$$

Given that:

$$\frac{[E \cdot S]}{[E] + [E \cdot I] + [E-I] + [E \cdot S]} = \frac{\frac{[S]}{K_M}}{1 + \frac{[I]}{K_i^*} + \frac{[S]}{K_M}} \quad \text{eq. 19,}$$

We obtain:

$$v_s = k_{\text{cat}}[E]_0 \frac{\frac{[S]}{K_M}}{1 + \frac{[I]}{K_i^*} + \frac{[S]}{K_M}} \quad \text{eq. 20.}$$

The decay from v_0 to v_s therefore reflects the decrease of the enzyme that is available to form $E \cdot S$ due to the conversion from $E \cdot I$ to $E-I$. This conversion is first order, and that is why the decay takes an exponential form in eq. 14. This conversion is also reversible, so its rate constant k_{obs} is the sum of the reverse and the forward reaction rate constant, k_{-5} and k_5 , with the former modified by the proportion of $E \cdot AVB$ in total enzyme:

$$k_{\text{obs}} = k_{-5} + k_5 \frac{[E \cdot I]}{[E] + [E \cdot I] + [E \cdot S]} \quad \text{eq. 21.}$$

Given that:

$$\frac{[E \cdot I]}{[E] + [E \cdot I] + [E \cdot S]} = \frac{\frac{[I]}{K_i}}{1 + \frac{[I]}{K_i} + \frac{[S]}{K_M}} \equiv \Theta \quad \text{eq. 22,}$$

where Θ is defined as the partition ratio, we obtain:

$$k_{\text{obs}} = k_{-5} + k_5 \Theta \quad \text{eq. 23.}$$

The key to obtaining k_5 , K_i , and k_{-5} in this work is to measure v_0 , from which K_i is fitted using eq. 17. With the obtained K_i and Θ , k_5 is determined from eq. 23. In parallel, by measuring v_s , K_i^* is fitted using eq. 20. Finally, k_{-5} is obtained using K_i , k_5 , and K_i^* according to eq. 12. To accurately measure v_0 , we used the stopped-flow technique to capture early data points; in addition, the dead time was determined to precisely position t_0 on the product v s time trace.

Choice of the Substrate for Probing the Inhibition: We chose nitrocefin (Cayman Chemical) as the substrate for probing the inhibition of WT due to the large absorbance change in nitrocefin hydrolysis. Its $\Delta\epsilon_{486}$ was determined as $15217 \text{ M}^{-1} \text{ cm}^{-1}$ through complete hydrolysis of nitrocefin of known concentrations. The large $\Delta\epsilon_{486}$ allows for sensitive probing of the inhibition progression. The values of k_{cat} and K_{M} were measured as $1000 \pm 16 \text{ s}^{-1}$ and $65 \pm 1 \text{ }\mu\text{M}$ for the WT using full-time kinetics as described for PenG hydrolysis.

We chose PenG as the substrate for probing the inhibition of mutants other than the WT because their K_{M} for nitrocefin hydrolysis is too large. Therefore, nitrocefin is no longer a suitable substrate to use in these inhibition experiments.

Dead-Time Measurement for the Stopped-Flow Setup: To precisely fit the initial rate v_0 , it is important to know the delay in collecting the first data point. When solutions are mixed in the stopped-flow setup, there is a delay in the change of absorbance due to the mixing (Figure S34a). Such delay is the sum of the intrinsic dead time of the stopped-flow apparatus and the step of time in absorbance reading (every 33 ms on the Cary 6000i UV-Vis-NIR spectrometer). In analysis of absorbance-time traces, we started from the last data point that has not been affected by mixing (“-3” in Figure S34a) and count for another 3 data points forward as the arbitrarily chosen time zero (“0” in Figure S34a). To measure how much the time zero that we chose is delayed from the actual time zero, we developed an assay based on nitrocefin hydrolysis by the WT TEM-1.

The WT TEM-1 was prepared at a series of concentrations (0, 60, 120, 180, 240, and 300 nM) in a reaction buffer containing 0.02% (w/v) BSA and 50 mM KPi (pH 7.0). Nitrocefin was first prepared as a stock solution in DMSO at 160 mM and then diluted to a final concentration of 400 μM in the reaction buffer. The inhibition reaction was monitored on a Cary 6000i UV-Vis-NIR spectrometer equipped with a stopped-flow accessory. Prior to use, all cuvettes and mixing tubing were passivated with a solution containing 0.1% (w/v) BSA and 50 mM KPi (pH 7.0) for at least 30 min before washing with the reaction buffer. The TEM-1 solution and the nitrocefin solution were loaded into the syringes of the stopped-flow accessory and quickly mixed in the cuvette. The hydrolysis of nitrocefin was monitored at 486 nm ($\Delta\epsilon_{486} = 15217 \text{ M}^{-1} \text{ cm}^{-1}$) every 33 ms.

Compared with the blank control (0 WT concentration), other absorbances at the first data point are larger because the hydrolysis of nitrocefin has already taken place for the period of the deadtime. Such excess absorbance can be converted into the concentration of the initial product. The concentration of initial product varies between experiments because they were run with varying $[\text{E}]_0$. The different $[\text{E}]_0$ is manifested by the different initial rates, which were obtained as the slope of the linear fitting of the first 7 data points. The higher the $[\text{E}]_0$, the faster the initial rates. Instead of $[\text{E}]_0$, we directly used the initial rates for the following analysis. We drew a linear correlation between the initial product concentration and the initial rates and obtained the dead time as the slope (Figure S34b), which is 58 ms.

General Protocol of the Inhibition Experiment: Let us first use the WT as an example to demonstrate the inhibition experiments. The WT was prepared at a concentration of 20 nM in a reaction buffer containing 0.02% (w/v) BSA and 50 mM KPi (pH 7.0). Nitrocefin was first

prepared as a stock solution in DMSO at 160 mM and then diluted to a final concentration of 400 μM in the reaction buffer. In this way, the final concentration of DMSO in the reaction mixture is only 0.12%, minimizing its effect on the kinetics. AVB was added into the nitrocefin solutions at a series of concentrations of 10, 20, 30, 40, 50, 60, and 70 μM . In addition, a blank control without AVB was prepared. In total, there are 8 nitrocefin samples containing varying concentrations of AVB.

The inhibition reaction was monitored on a Cary 6000i UV-Vis-NIR spectrometer equipped with a stopped-flow accessory. Prior to use, all cuvettes and mixing tubing were passivated with a solution containing 0.1% (w/v) BSA and 50 mM KPi (pH 7.0) for at least 30 min before washing with the reaction buffer. The TEM-1 solution and the nitrocefin solution were loaded into the syringes of the stopped-flow accessory and quickly mixed in the cuvette. The hydrolysis of nitrocefin was monitored at 486 nm ($\Delta\epsilon_{486} = 15217 \text{ M}^{-1} \text{ cm}^{-1}$) every 33 ms until the absorbance increases linearly and enough data points have been collected in the linear region. The experiment from mixing to monitoring was repeated 5 times. The same procedure was repeated for all the 8 nitrocefin samples. A representative product vs time trace of each [I] is shown in Figure S35a,b.

To analyze the experimental data, which consist of product vs time traces at each [I], we first used Script 4 to fit the inhibition features, including v_0 , k_{obs} and v_s , according to eq.13 (Figure S35a,b). With the obtained v_0 and k_{obs} , we then used Script 5 to fit K_i and k_5 , according to eq. 17 and eq. 23, respectively (Figure S35c,d). Not all the obtained values of v_0 were used for fitting K_i . Those obtained from experiments using high [I] and exhibiting large k_{obs} could be unreliable, evidenced by a large variance at the same [I], and these values of v_0 are not used for fitting K_i . Note that $[\text{E}]_0$, [S], and [I] should be half of those in preparation of the samples due to the 1:1 mixing of two solutions in the stopped-flow apparatus. The script only allows for using a constant $[\text{E}]_0$, therefore the product concentration can be normalized against the same $[\text{E}]_0$ if multiple $[\text{E}]_0$ values are used, as described later for A237Y. In parallel, using the obtained v_s from Script 4, we run Script 6 to fit K_i^* based on eq. 20, and finally to calculate k_{-5} from k_5 , K_i , and K_i^* based on eq. 12 (Figure S35e). The results for all the mutants are listed in Table S2.

Choice of Concentration: The concentrations of the WT, nitrocefin, and AVB are judiciously chosen. In order to use eq. 17 to fit K_i , $[\text{I}]/K_i$ should be large enough compared with $[\text{S}]/K_M$ to cause measurable changes of v_0 by varying [I]. The side effect of having a large $[\text{I}]/K_i$ is an accompanying large k_{obs} , according to eq. 21, especially when k_5 is large. This means that the product vs time trace will quickly enter the linear region and only limited data are collected for fitting k_{obs} . Therefore, $[\text{I}]/K_i$ should be designed to vary in a suitable range, which is large enough to change v_0 (by $> 5\%$) but not too large such that k_{obs} remains $< 3 \text{ s}^{-1}$. To help satisfy the former requirement, $[\text{S}]/K_M$ should avoid being too large. But [S] cannot be too low, otherwise the substrate consumption cannot be neglected, disallowing the treatment of [S] as a constant, which is a key assumption. In our experiments, the final [P] never exceeds 5% of [S]. This requirement can also be met by using a low $[\text{E}]_0$. However, $[\text{E}]_0$ should also be large enough to produce a sizable v_s , otherwise a prolonged accumulation of data in the linear region is necessary. Along this line, a variation of the above protocol is to use a series of $[\text{E}]_0$ for different nitrocefin samples. For those nitrocefin samples with a low [I], a low $[\text{E}]_0$ is used to avoid a high [P]; for those with a high [I], a high $[\text{E}]_0$ is used to produce a sizable v_s . In addition, $[\text{E}]_0$ should always be $\ll [\text{I}]$.

When the inhibition constants (K_i , k_5 , and k_{-5}) were unknown, we started with an estimation of their values based on other mutants or simply by guessing. Then we tried out $[E]_0$, $[S]$, and $[I]$ using Script 7 that simulates the corresponding $[P]$, v_0 , k_{obs} and v_s . If we were satisfied with the simulated $[P]$, v_0 , k_{obs} and v_s , we would proceed to use the $[E]_0$, $[S]$, and $[I]$ for carrying out kinetic measurements. From the experimental data, we used Scripts 4-6 to obtain the fitted K_i , k_5 , and k_{-5} . If there is a big deviation from our guess, we may have used unsuitable values of $[E]_0$, $[S]$, and $[I]$ for the experiments. In such cases, the data may not be able to provide an estimation of K_i , k_5 , and k_{-5} , but at least some hints on the range of their values. We then made new guesses based on the hints from the last experiment and repeated this process until we arrived at a suitable $[E]_0$, $[S]$, and $[I]$, and the experimental data allowed for reliable fitting of K_i , k_5 , and k_{-5} . In our experience, no more than two rounds were required to obtain the final results.

Using PenG as the Substrate: For mutants that use PenG as the substrate to probe their inhibition kinetics, all the procedures are the same, except for monitoring the reaction at 232 nm ($\Delta\epsilon_{232} = -940 \text{ M}^{-1} \text{ cm}^{-1}$). Due to the small $\Delta\epsilon_{232}$, the targeted v_0 and v_s should be correspondingly larger. Here is an example. The A237Y mutant was prepared in the reaction buffer containing 0.02% (w/v) BSA and 50 mM KPi (pH 7.0) at a series of concentrations of 0.5 (for blank control), 1, 2, 3, 4, 5, and 6 μM . PenG was prepared at a concentration of 10 mM in the reaction buffer, into which AVB was added at a series of concentrations of 0 (blank control), 100, 200, 300, 400, 500, and 600 μM , respectively. In total, there are 7 solutions of A237Y and 7 solutions of PenG containing varying concentrations of AVB. They are used in pairs for mixing in the stopped-flow apparatus. A representative product *vs* time trace for each $[I]$ and the fitting of the whole data is shown in Figure S36.

A237Y^e Inhibition Experiment: The ester protein exhibits relatively slow kinetics for AVB inhibition. Therefore, rather than waiting for the equilibrium of E-I formation, we performed its kinetic measurements in two separate experiments. The first experiments only monitored the first 1 h of the product *vs* time trace, allowing us to collect enough data for fitting k_{obs} and v_0 using Script 4 (conditioned that $v_s = 0$), which are in turn used for the fitting of K_i and k_5 using Script 5. The results are shown in Figure S37a-c. A separate set of experiments was performed on samples that contain various concentrations of $[I]$ and were equilibrated for 2 days before the addition of PenG and the measurement of product *vs* time trace. A linear fitting produced v_s , which was subsequently used for fitting K_i^* and k_{-5} using Script 6. The results are shown in Figure S37d.

Supporting Text

Text S1. Attempts to crystallize the A237Y^e mutant of TEM-1

We expressed the A237Y^e variant of TEM-1-native and found this protein is very susceptible to the hydrolysis of the backbone ester. Incubation at pH 7.0 overnight led to >50% protein fragmentation at the site of the ester, as characterized by HPLC-MS. To use a stable protein for crystallization, we expressed the E166N mutant of TEM-1-native-A237Y^e, which showed <1% hydrolysis of the backbone ester under the same incubation condition. We tried to crystallize this protein using both crystallization conditions (using ammonium sulfate and PEG3350 as precipitants, respectively) as described in the section *Protein Crystallization and Crystallography* but did not obtain crystals. We further tried to co-crystallize this protein with 5 mM AVB, which forms a covalent complex, but obtained no crystals. We noticed that E166N-A237Y^e is not thermally stable enough for crystallization at room temperature. After being left at room temperature for two days, it cannot react with AVB any more as measured by mass spectrometry. We also tried to grow the crystal at 4°C using the above conditions and to vary the pH between 6.0 and 7.0 but still obtained no crystals.

E166N is a general destabilizing mutation for TEM proteins. The A237Y^e mutation is more destabilizing than A237Y given the success in crystallizing E166N-A237Y. This makes sense because the ester backbone not only cannot act as a H-bond donor, but also becomes a weaker H-bond acceptor compared to a normal amide backbone. This impacts the two H-bonds from G244 and R243 to the 237 backbone, leading to an overall destabilization/conformational flexibility of the A237Y^e mutant. For this reason, we chose to use ¹H NMR as an alternative to characterize the structure of A237Y^e.

Text S2. Rich conformational heterogeneity for TEM-AVB

An envelope of five ¹²C=O peaks were observed in the isotope-edited infrared spectra of TEM-AVB covalent complexes, while there are only three peaks for TEM•AVB. This is a counterintuitive observation because covalently bound ligands might be expected to be more conformationally rigid than the noncovalently bound counterparts. Although the covalent linkage is an anchor that limits the movement of AVB, it is not the only anchor through which AVB interacts with the protein active site. The sulfate and amide side groups in AVB are the other two anchors, forming significant noncovalent interactions whose contribution to the binding energy is essential. Due to competition among the anchors, multiple local minima are possible.

Comparing TEM-AVB with TEM•AVB, it is also interesting to see that the sulfate group in AVB becomes more flexible in TEM-AVB. As shown in Figure 2b, the sulfate is connected to the ring through a flexible NH bridge which was part of the rigid ring in TEM•AVB. The extra flexibility of the sulfate anchor may also lead to heterogenous positioning of the C=O.

Comparing TEM-AVB with TEM-PenG, we found that PenG experiences less conformational heterogeneity evidenced by fewer ¹²C=O peaks present in the isotope-edited infrared spectrum of WT TEM-PenG (ref.³). We posit that the three anchors can act more synergistically, favoring the same conformations. This is a reasonable hypothesis because TEM

proteins have evolved for billions of years to become a PenG-hydrolysis specialist⁴⁴, while AVB is a human-made compound less optimized to sit in the active site as described above.

Text S3. Largest field contributes dominantly to rate enhancement

When multiple ¹²C=O peaks are found, the peak of the lowest frequency was used for analyzing the electric field's contribution to catalysis, because the lowest frequency corresponds to the largest electric field and thus contributes the most to the lowering of free energy barrier. Consider a field lower than the largest field by 20 MV/cm, or in a more relevant unit, 1 kcal/mol/D. Given a reaction difference dipole of 1.4 D, this field provides a lowering of free energy barrier 1.4 kcal/mol smaller than that by the largest field. Accordingly, the rate enhancement conferred by this field is only 0.09-fold of that by the largest field. That means the population of C=O that experiences this field can only react 0.09-fold as fast as that experiencing the largest field. Therefore, the largest field plays a dominant role in promoting reactions.

A more rigorous treatment is to sum the contribution of each observed field population. However, the weight of each field population is not simply their peak area because the C=O bond in different electrostatic environments may have somewhat different transition dipole moments for the vibration⁴⁵. The peak area analysis may be further complicated by the baselining of the difference spectra. Therefore, we chose to only pick the largest field for a more straightforward data analysis.

Text S4. Change in magnitude of electric field due to the ester mutation

Compared with A237Y, A237Y^e is found to exert electric fields onto the C=O that are smaller in magnitude by 61 MV/cm for TEM•AVB and by 67 MV/cm for TEM–AVB. However, for TEM•PenG, the field decrease due to the ester backbone is only 25 MV/cm. The remaining field (-138 MV/cm) is still very large. To explain this observation, we hypothesize that the remaining large fields arise from not only the H-bond from S70 backbone amide but also oriented dipoles across the whole enzyme scaffold whose preorganization has been optimized through evolution. This hypothesis is supported by polarizable MD simulations on TEM•PenG where frames displaying no H-bonds for PenG's β-lactam C=O are still calculated with electric fields more negative than -100 MV/cm (Figure S31d-f).

Text S5. Comparison with previous kinetic studies of AVB inhibition

Previous kinetic studies on AVB inhibition used eq. 22 & 23 to determine the value of k_{cbm}/K_i , but not their individual values, as exemplified by the original work⁴³. Also, k_{rec} has never been measured, but instead k_{off} has been a common target of measurement. k_{off} is often measured as the value of k_{obs} in eq. 22 & 23 when [I] is very low, such as that in a jump-dilution experiment. However, the contribution from k_{cbm} still cannot be neglected when $k_{cbm} \gg k_{rec}$, which is exactly the case here. Therefore, the k_{off} values reported in the literature are not a good approximation of k_{rec} , but rather depend on how low [I] is in a specific experiment.

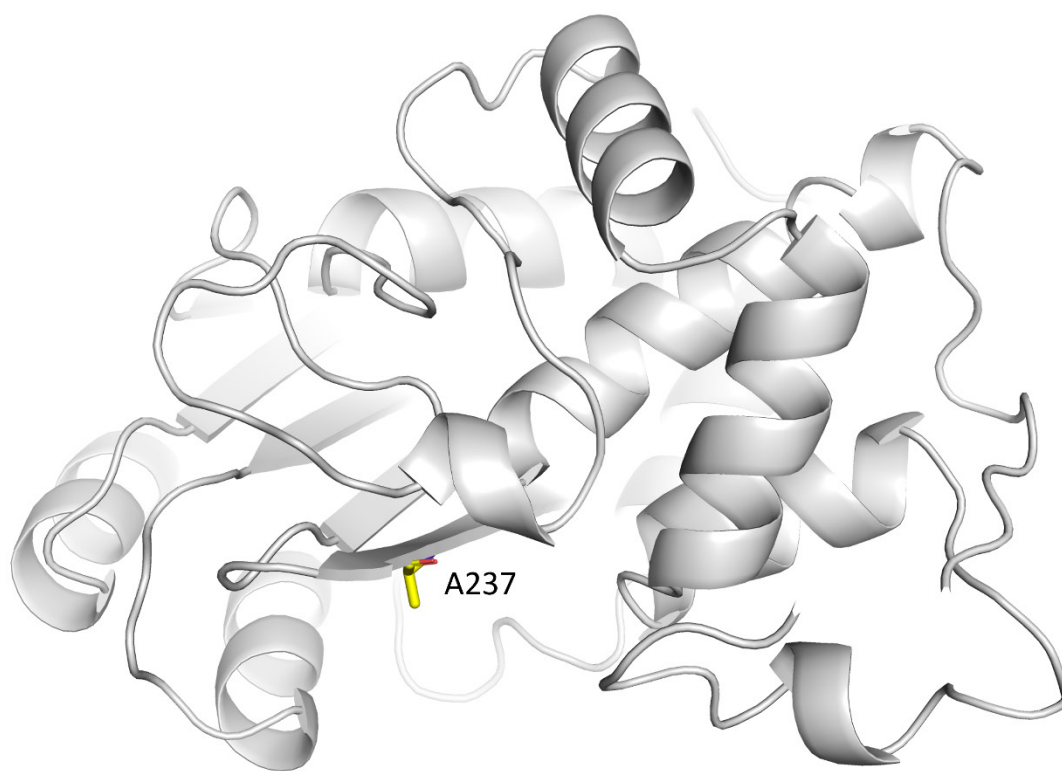


Figure S1. Crystal structure of WT TEM-1 (PDB: 7U6Q) with A237 highlighted. The methyl group of A237 is largely exposed to solvent.

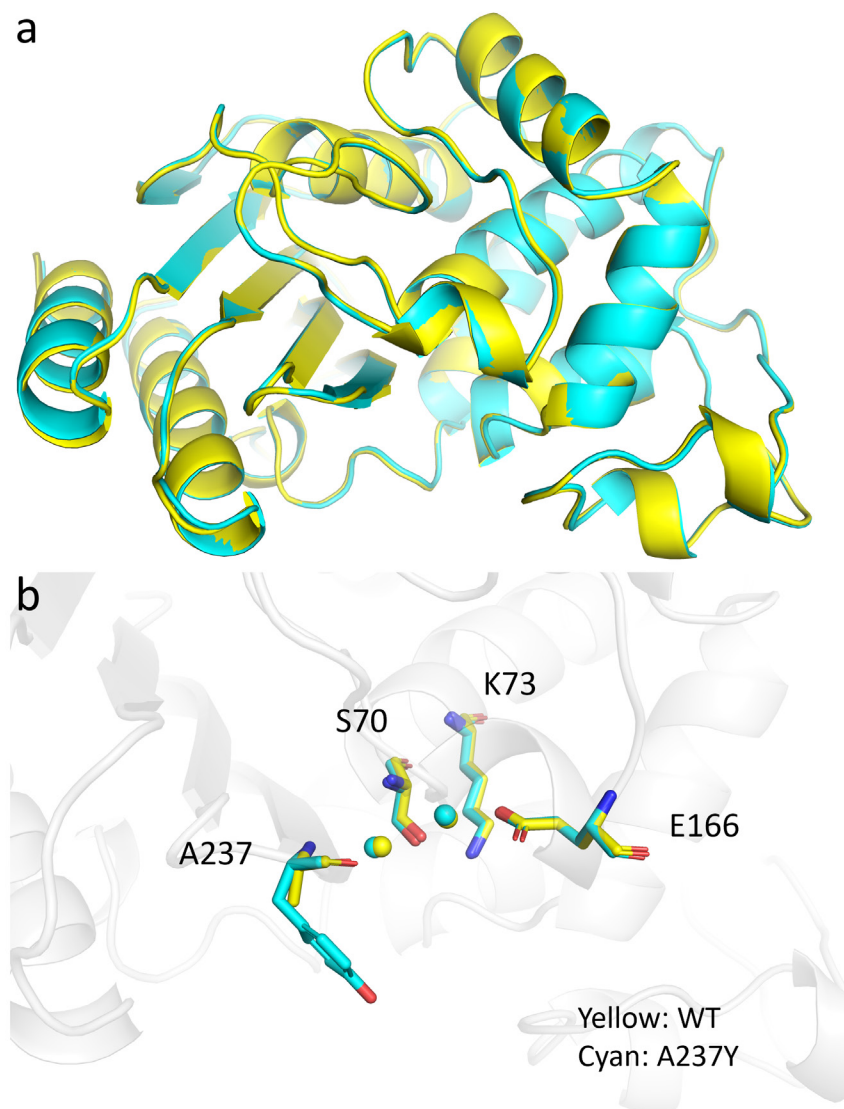


Figure S2. Overlays of the crystal structures of WT (yellow, PDB: 7U6Q) and A237Y (cyan, PDB: 8DDZ) TEM-1. (a) Global structures. (b) Key amino acids and structured water molecules in the active sites. The position of the A237 residue is slightly perturbed, with the methylene group in A237Y shifted away from the original methyl group in WT.

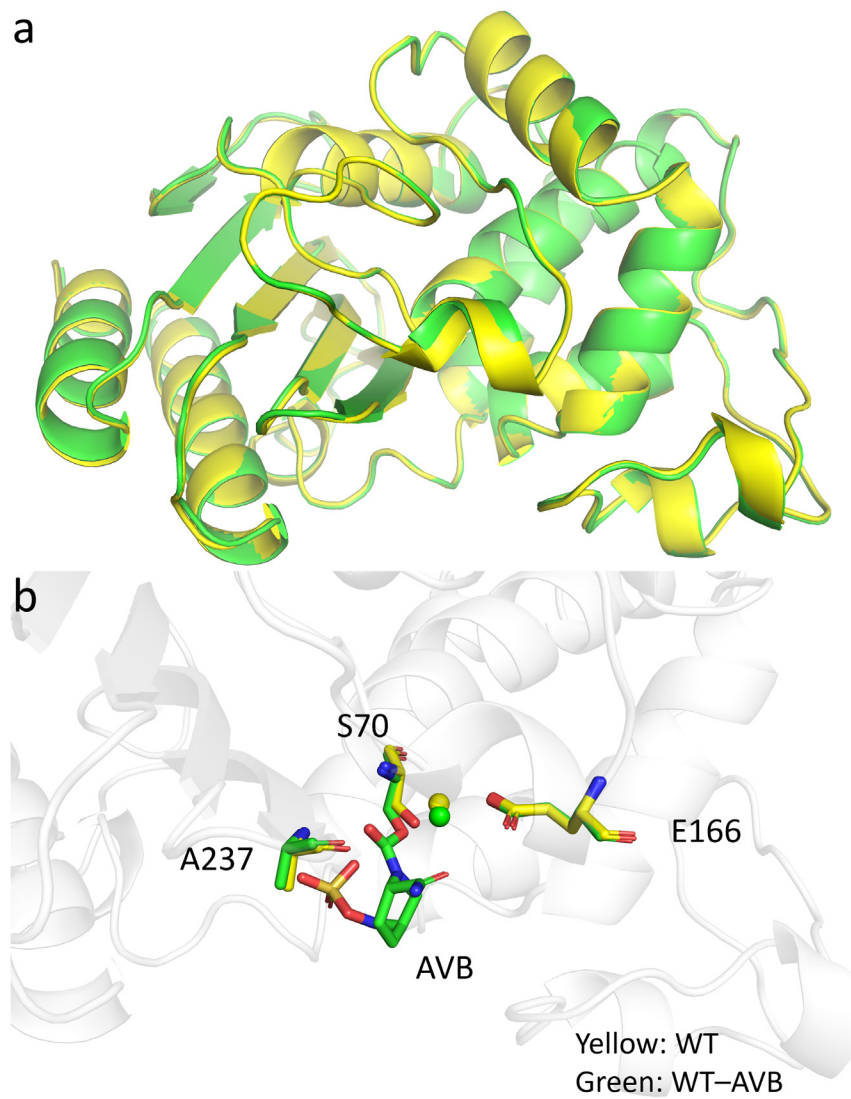


Figure S3. Overlays of the crystal structures of WT TEM-1 (yellow, PDB: 7U6Q) and TEM-AVB (green, PDB: 8DE0). (a) Global structures. (b) AVB, key amino acids, and structured water molecules in the active sites.

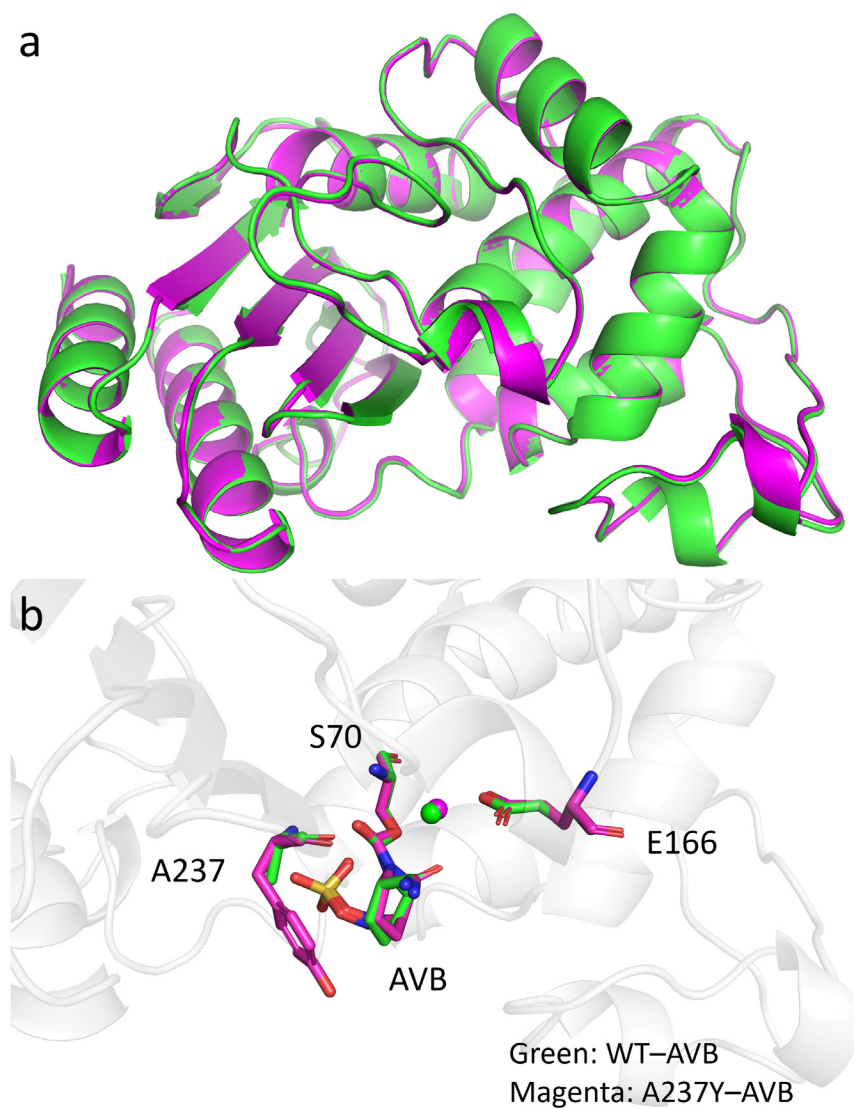


Figure S5. Overlays of the crystal structures of WT (green, PDB: 8DE0) and A237Y (magenta, PDB: 8DE1) TEM-AVB. (a) Global structures. (b) AVB, key amino acids, and structured water molecules in the active sites.

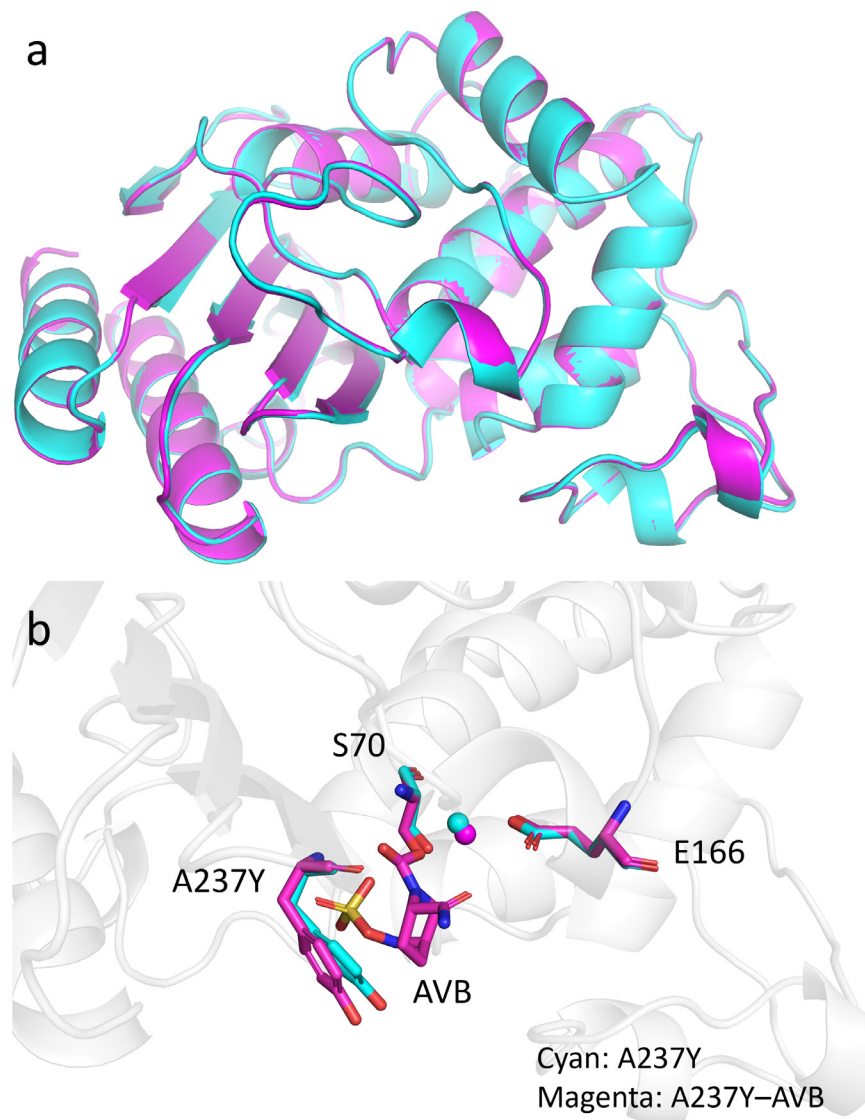


Figure S6. Overlays of the crystal structures of A237Y TEM (cyan, PDB: 8DDZ) and TEM-AVB (magenta, PDB: 8DE1). (a) Global structures. (b) AVB, key amino acids, and structured water molecules in the active sites.

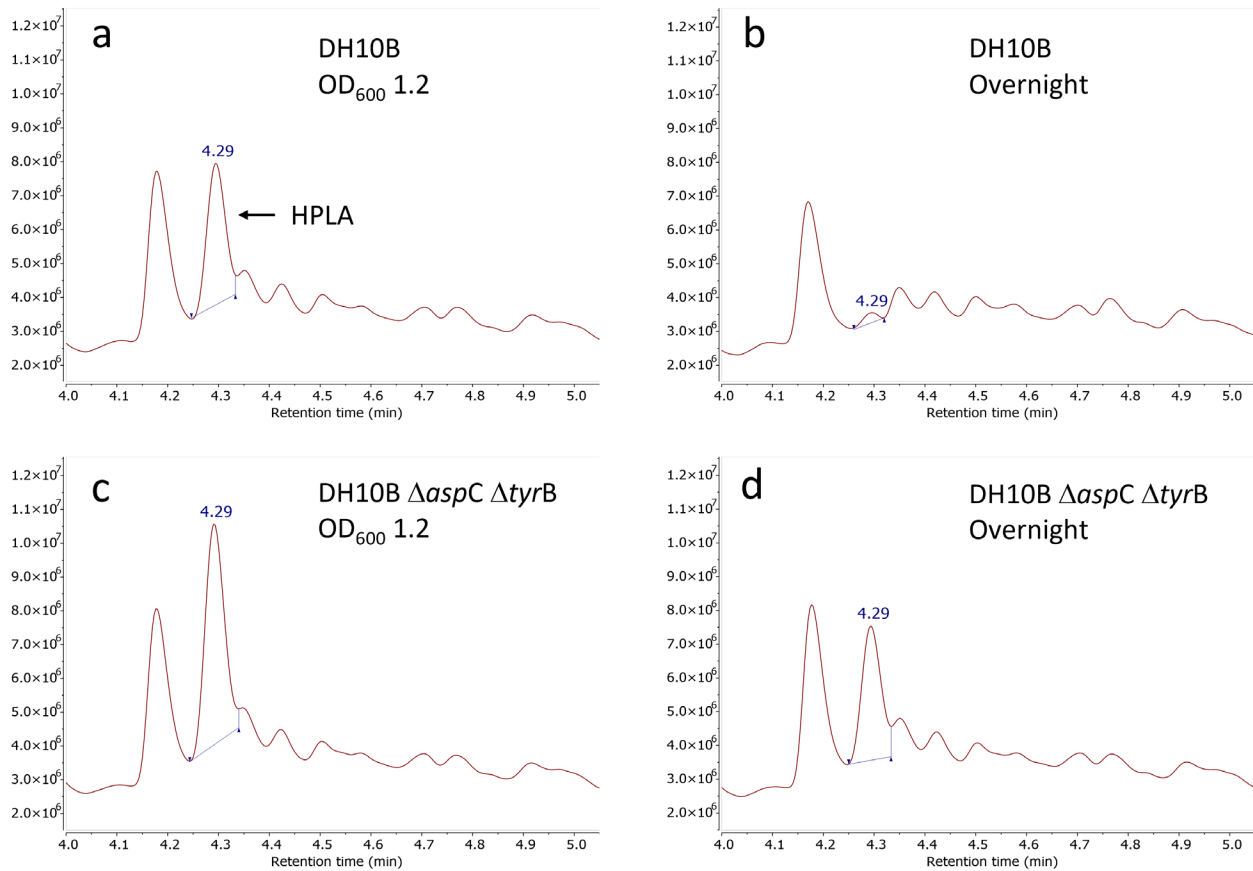


Figure S7. HPLC chromatograms of *E. coli* lysates for testing the metabolism of HPLA (starting from 1 mM). (a) DH10B cells were incubated at 37°C until OD₆₀₀ 1.2 before cell lysis. The peak area gives a HPLA concentration of 0.684 mM. (b) DH10B cells were incubated at 20°C overnight before cell lysis. The peak area gives a HPLA concentration of 0.039 mM. (c) DH10B $\Delta aspC \Delta tyrB$ cells were incubated at 37°C until OD₆₀₀ 1.2 before cell lysis. The peak area gives a HPLA concentration of 1.078 mM. (d) DH10B $\Delta aspC \Delta tyrB$ cells were incubated at 20°C overnight before cell lysis. The peak area gives a HPLA concentration of 0.657 mM. The method of HPLC is the same as described for HPLC-MS. The peak area of HPLA is calibrated by using HPLA solutions of known concentrations.

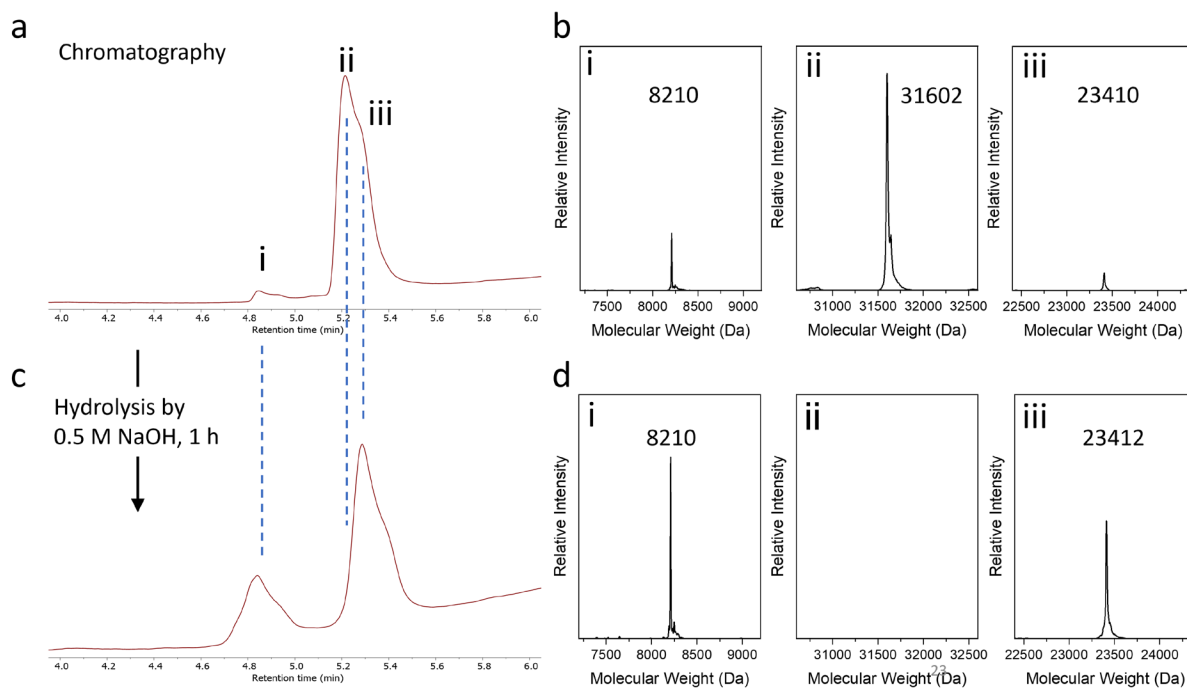


Figure S8. Characterization of A237Y^c using HPLC-MS (lower resolution). (a) HPLC chromatogram showing three components. (b) MS spectra of the three components, with i being the smaller fragment, ii being the whole protein, and iii being the larger fragment. The formation of the fragments is due to the hydrolysis of the ester bond during protein purification. (c,d) The ester bond is completely hydrolyzed by treating the protein with 0.5 M NaOH for 1 h, evidenced by the disappearance of the whole protein peak in the chromatogram (c) and the MS spectra (d).

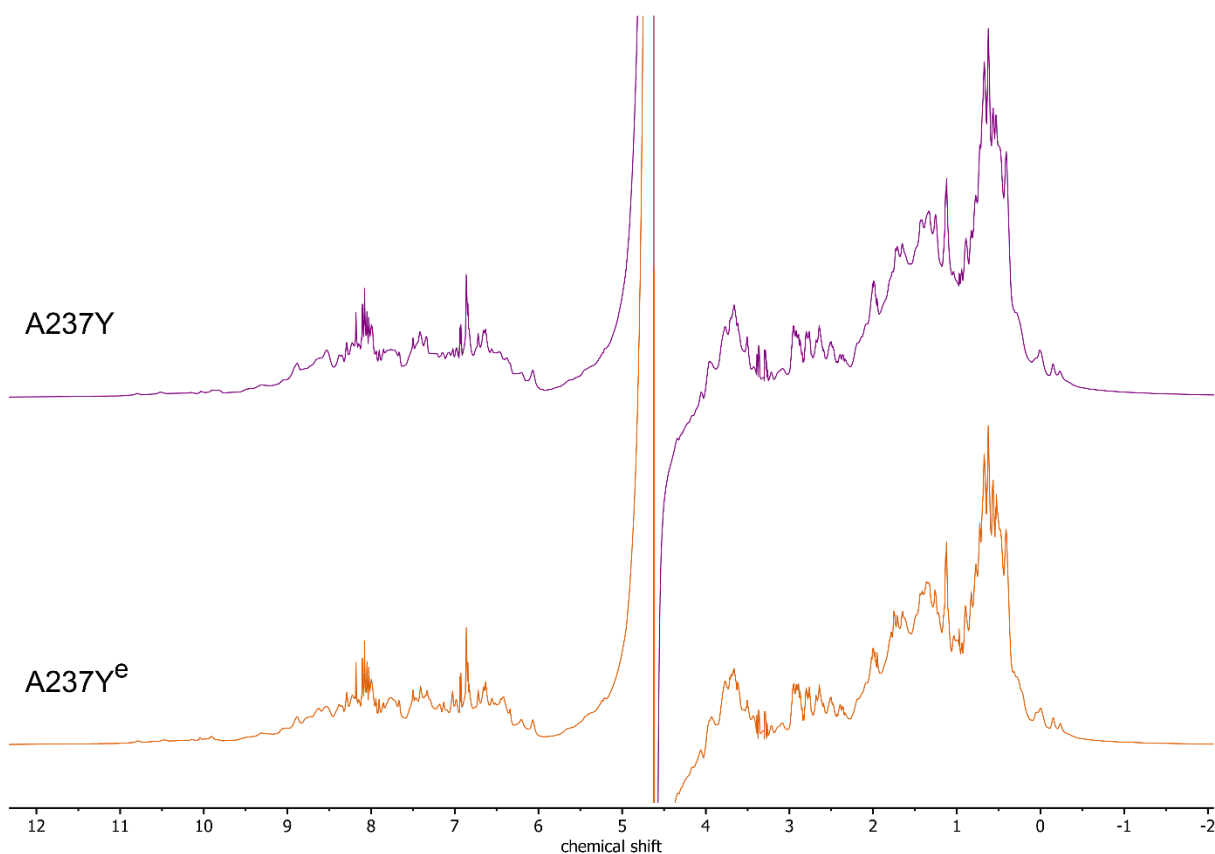


Figure S9. ¹H NMR spectra of the A237Y and A237Y^e mutants of TEM-1 (0.2 mM) in 20 mM potassium phosphate (pH 6.0, 10% D₂O, 15°C). Water suppression was achieved using the WET method¹⁰. These spectra and the enlarged versions of the aromatic and aliphatic regions (Figures S10 and S11, respectively) are nearly identical in every detail suggesting that the solution structure of A237Y^e is very similar to A237Y for which a crystal structure was obtained (see Figure S2).

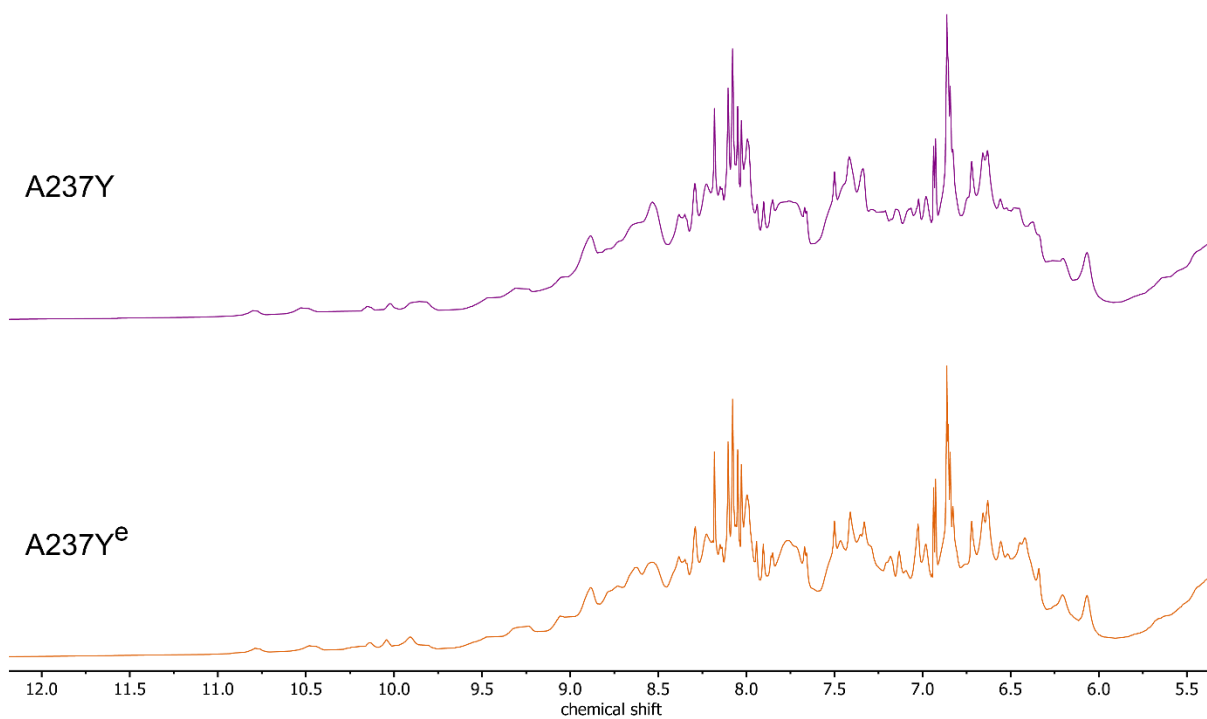


Figure S10. Downfield amide/aromatic region of ¹H NMR spectra of the A237Y and A237Y^e mutants of TEM-1. See Figure S9 caption for experimental details.

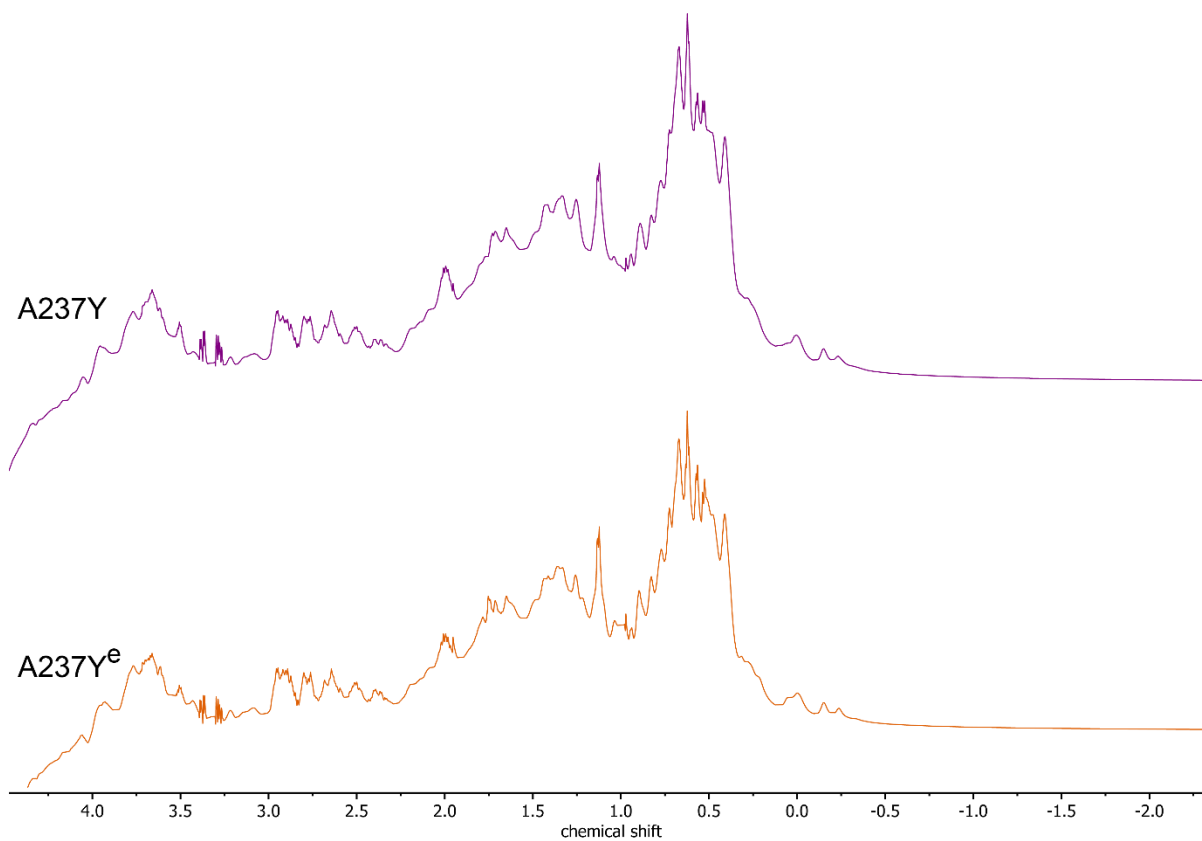


Figure S11. Upfield aliphatic region of ¹H NMR spectra of the A237Y and A237Y^e mutants of TEM-1. See Figure S9 caption for experimental details.

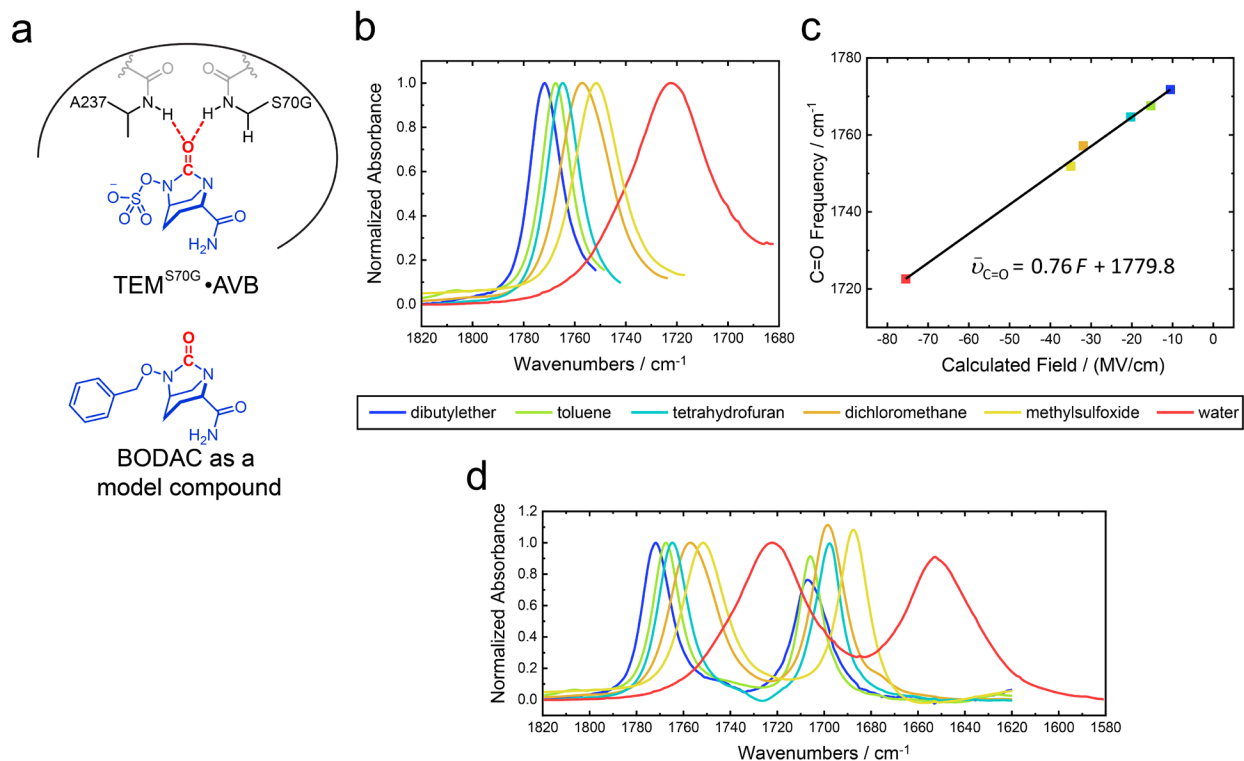


Figure S12. Calibration of BODAC as a vibrational Stark probe. (a) Structural analogue between TEM•AVB and BODAC. The charged sulfate group is replaced with a neutral benzyl group to avoid complicated MD simulations and to allow a broad range of solubility. (b) Infrared spectra of the urea C=O in BODAC dissolved in solvents of varying polarity. (c) Urea C=O infrared frequencies (by peak picking) plotted against the calculated electric fields based on MD simulations. A linear correlation provides the sensitivity of frequency shift to field (slope) as $0.76 \pm 0.02 \text{ cm}^{-1}/(\text{MV}/\text{cm})$ and the vibrational frequency in vacuum (intercept) as $1779.8 \pm 0.8 \text{ cm}^{-1}$. (d) A wider range of the infrared spectra of BODAC dissolved in solvents of varying polarity. The peaks at lower frequencies come from the vibration of the C=O in the side amide group. The peak intensities were normalized based on the intensities of the urea C=O.

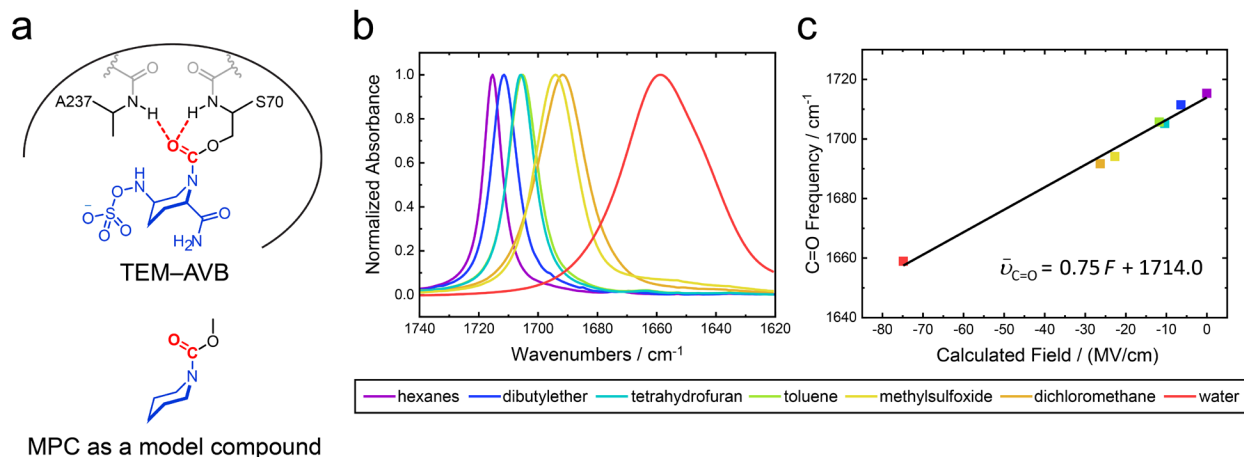


Figure S13. Calibration of MPC as a vibrational Stark probe. (a) Structural analogue between TEM–AVB and MPC. The charged sulfate group is removed to avoid complicated MD simulations and to allow a broader range of solubility. The amide side group is also removed for simplification. (b) The infrared spectra of MPC dissolved in solvents of varying polarity. (c) C=O infrared frequencies (by peak picking) were plotted against the calculated electric fields based on MD simulations. A linear correlation provides the sensitivity of frequency shift to field (slope) as $0.75 \pm 0.03 \text{ cm}^{-1}/(\text{MV}/\text{cm})$ and the vibrational frequency in vacuum (intercept) as $1714.0 \pm 1.1 \text{ cm}^{-1}$.

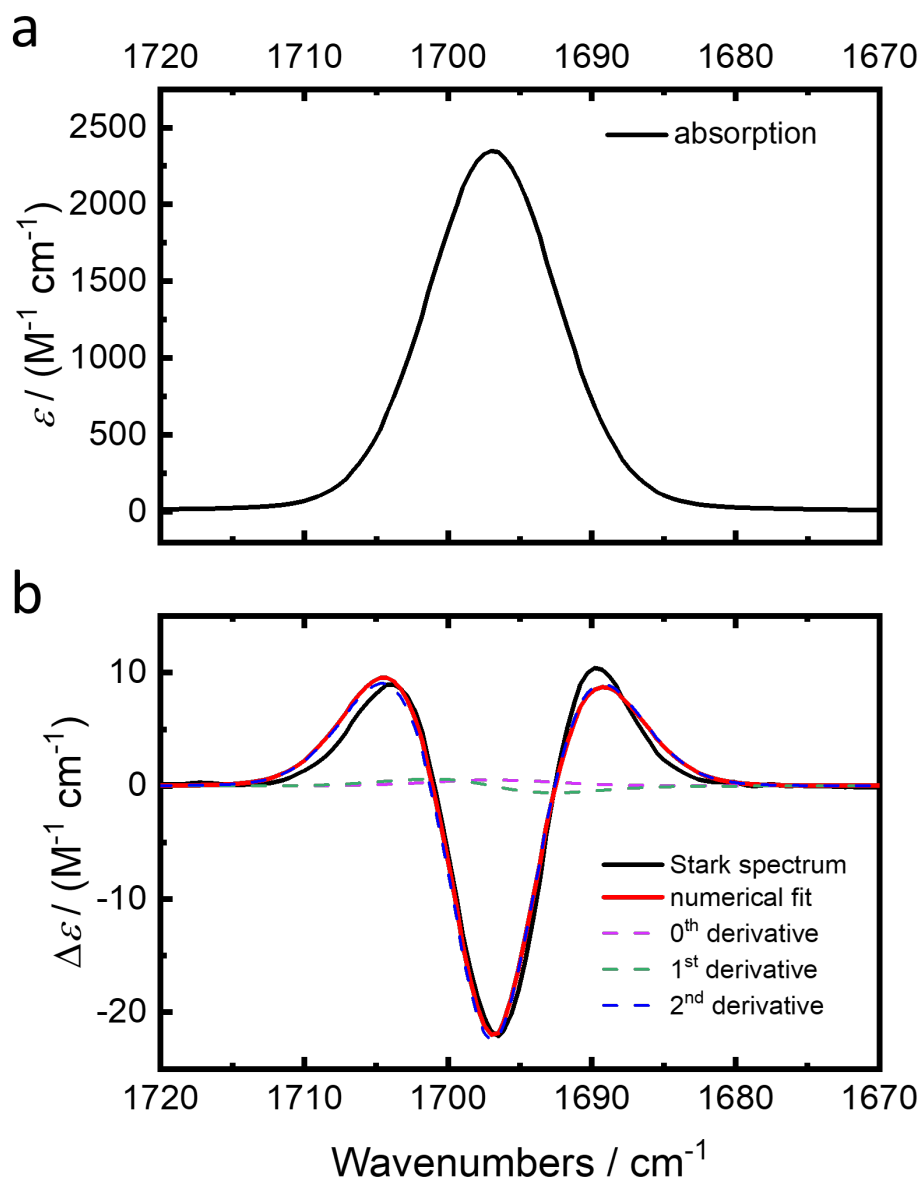


Figure S14. Infrared absorption and Stark spectra of MPC (50 mM in 2-methyltetrahydrofuran) at 77 K. (a) Infrared absorption spectrum. (b) Vibrational Stark spectrum scaled to an applied field of 1.0 MV/cm. The Stark spectrum was fitted to a sum of the derivatives of the absorption spectrum. See Table S14 for the fitting details.

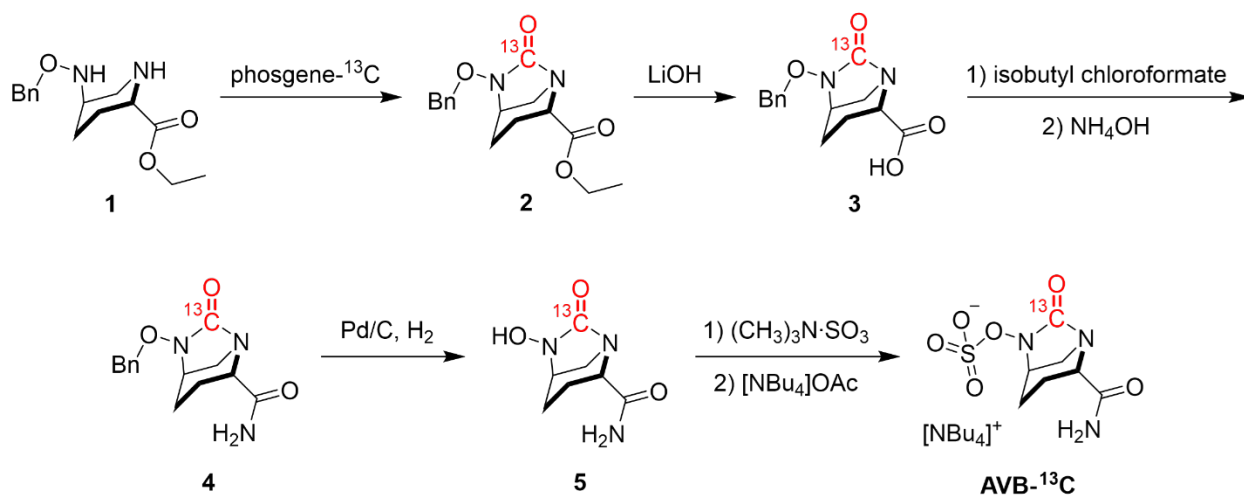


Figure S15. The synthetic route to ^{13}C -labeled AVB.

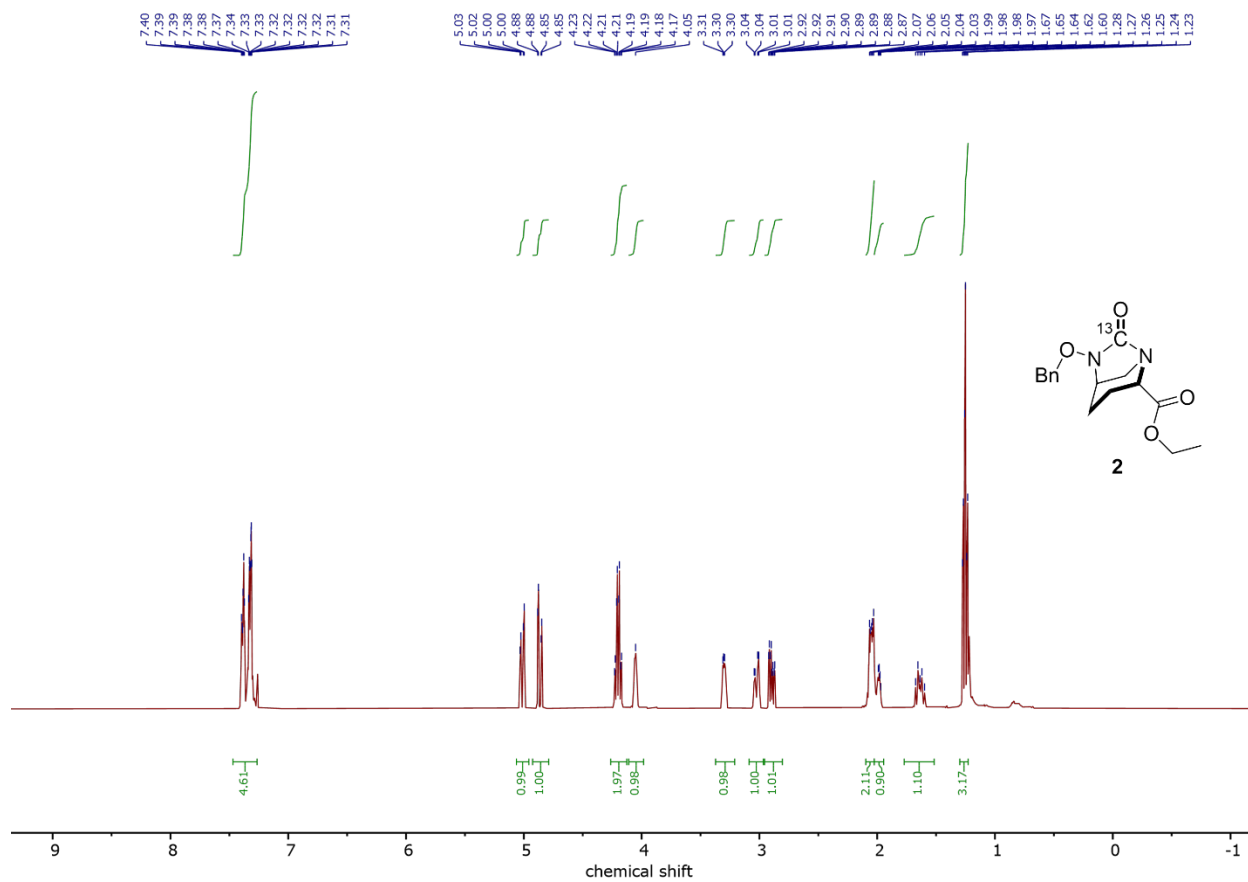


Figure S16. Liquid ¹H NMR spectrum of 2 in CDCl₃.

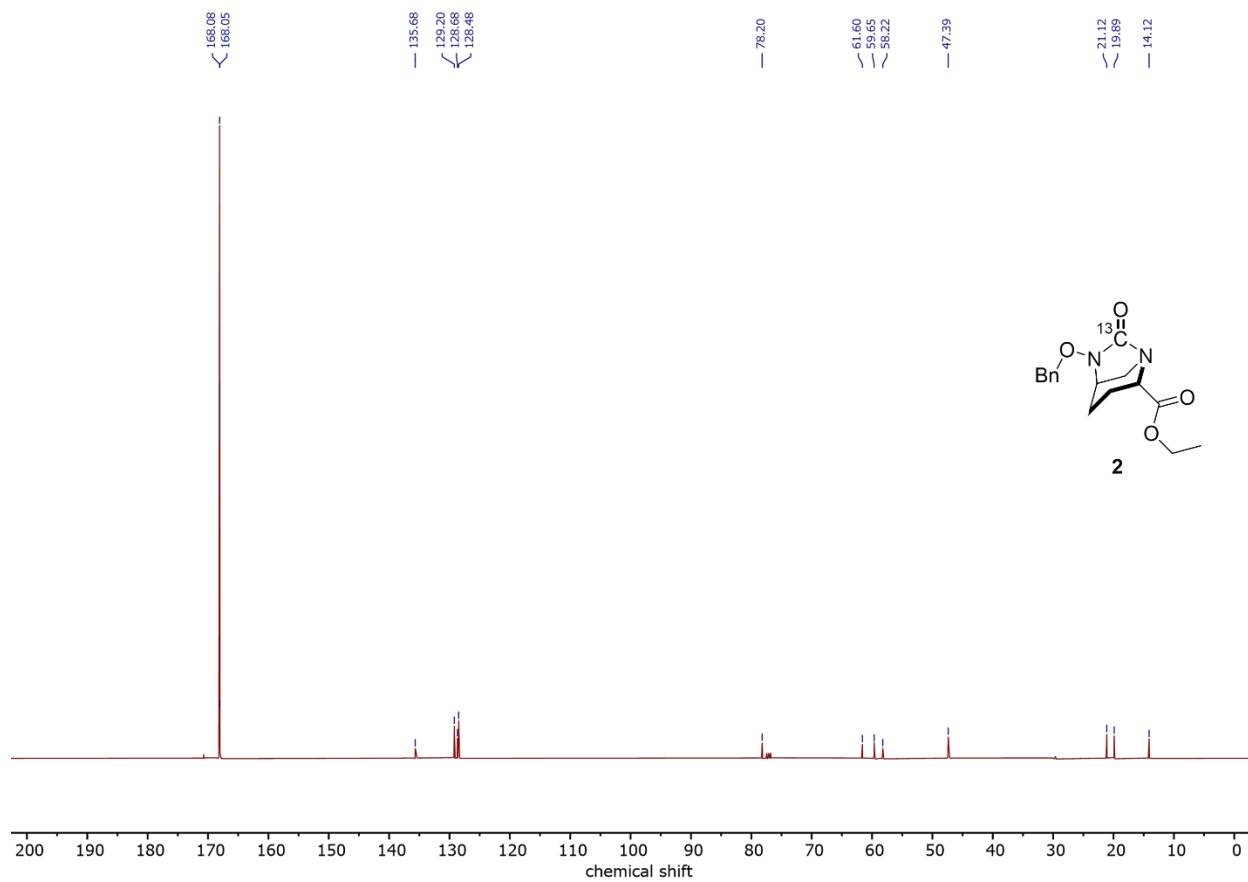


Figure S17. Liquid ^{13}C NMR spectrum of 2 in CDCl_3 .

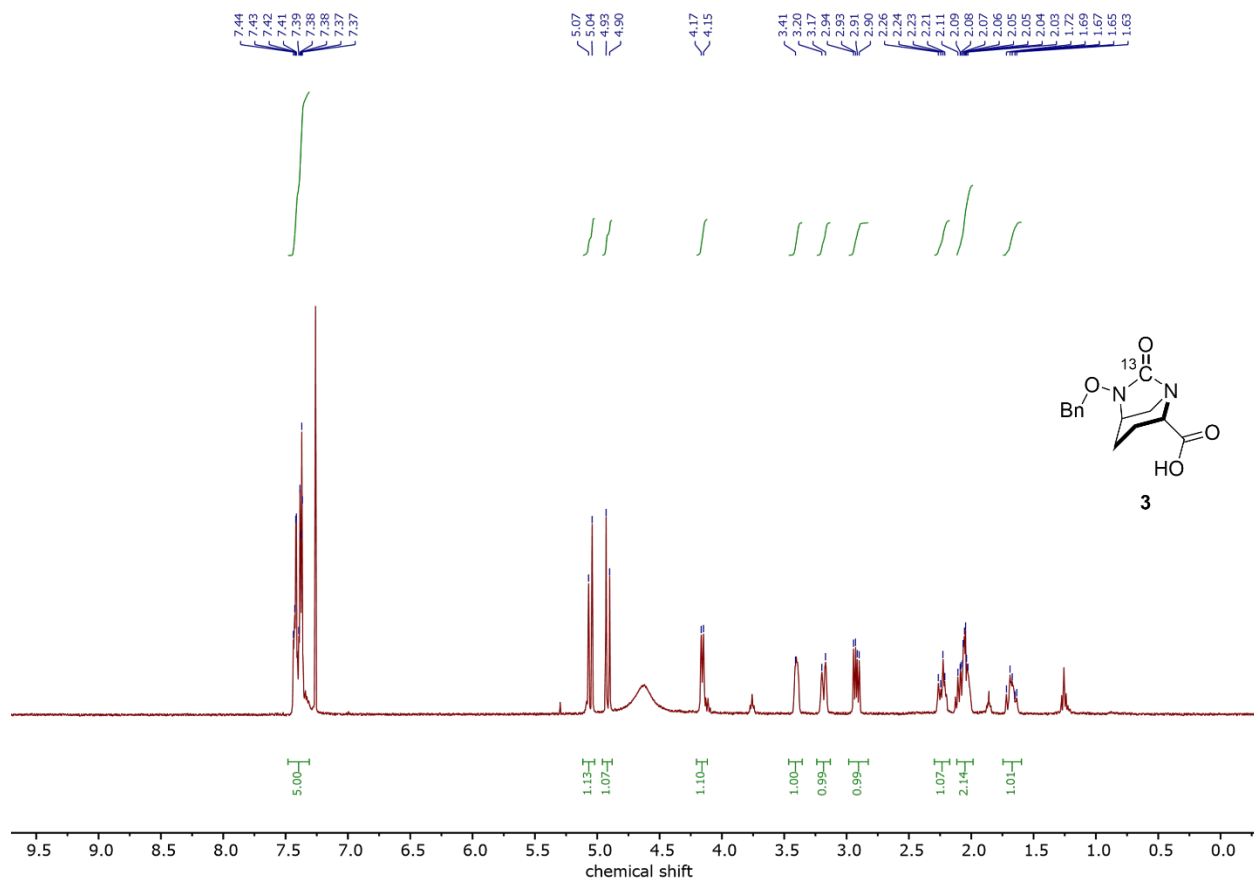


Figure S18. Liquid ¹H NMR spectrum of **3** in CDCl₃.

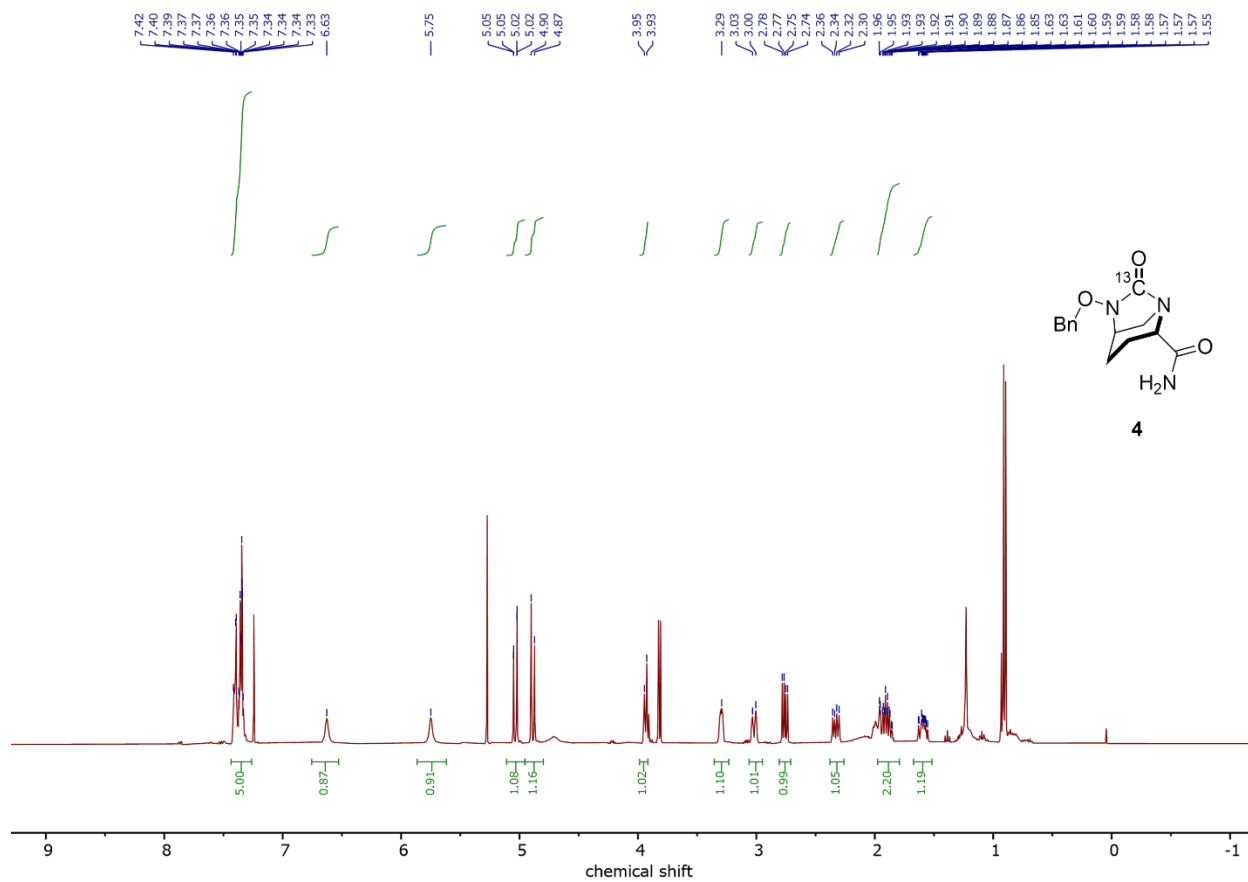


Figure S19. Liquid ¹H NMR spectrum of 4 in CDCl₃.

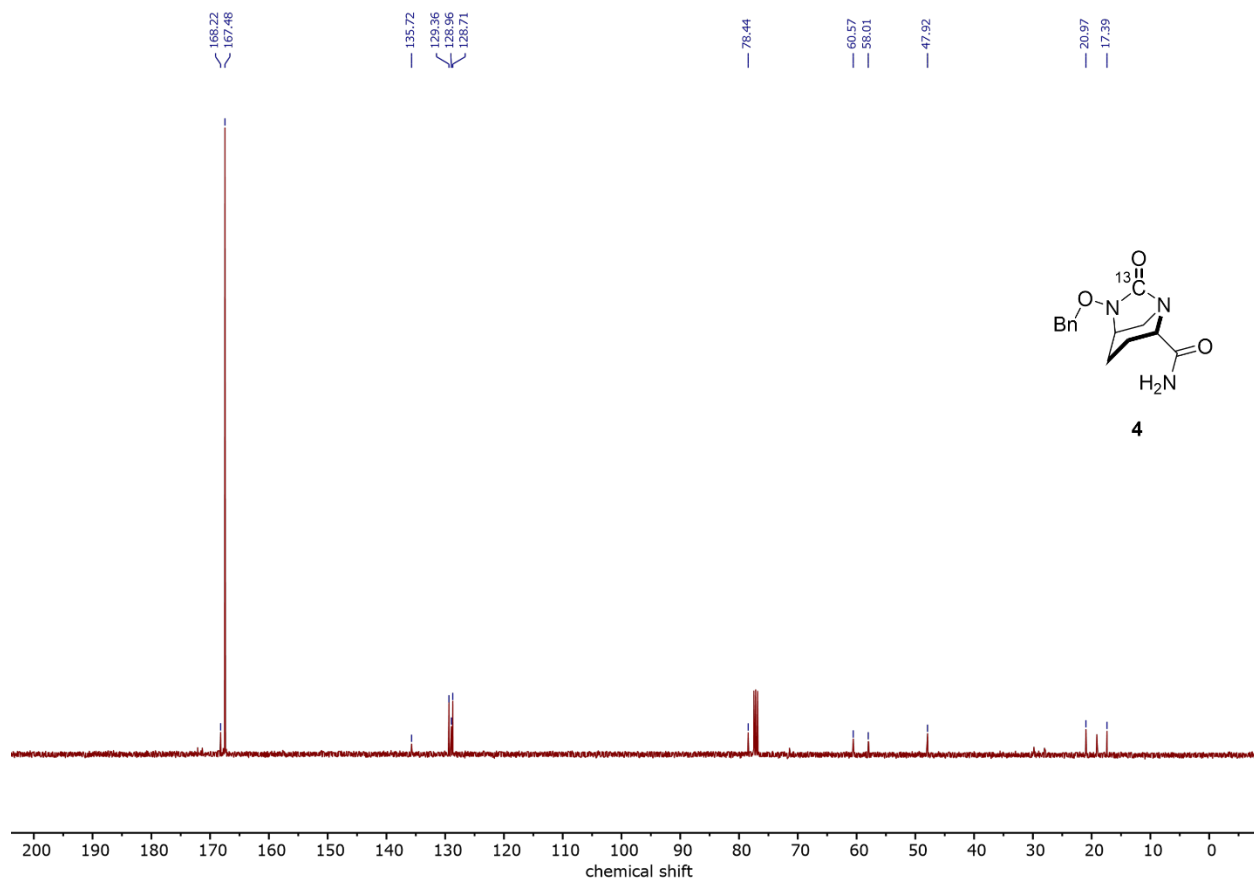


Figure S20. Liquid ¹³C NMR spectrum of 4 in CDCl₃.

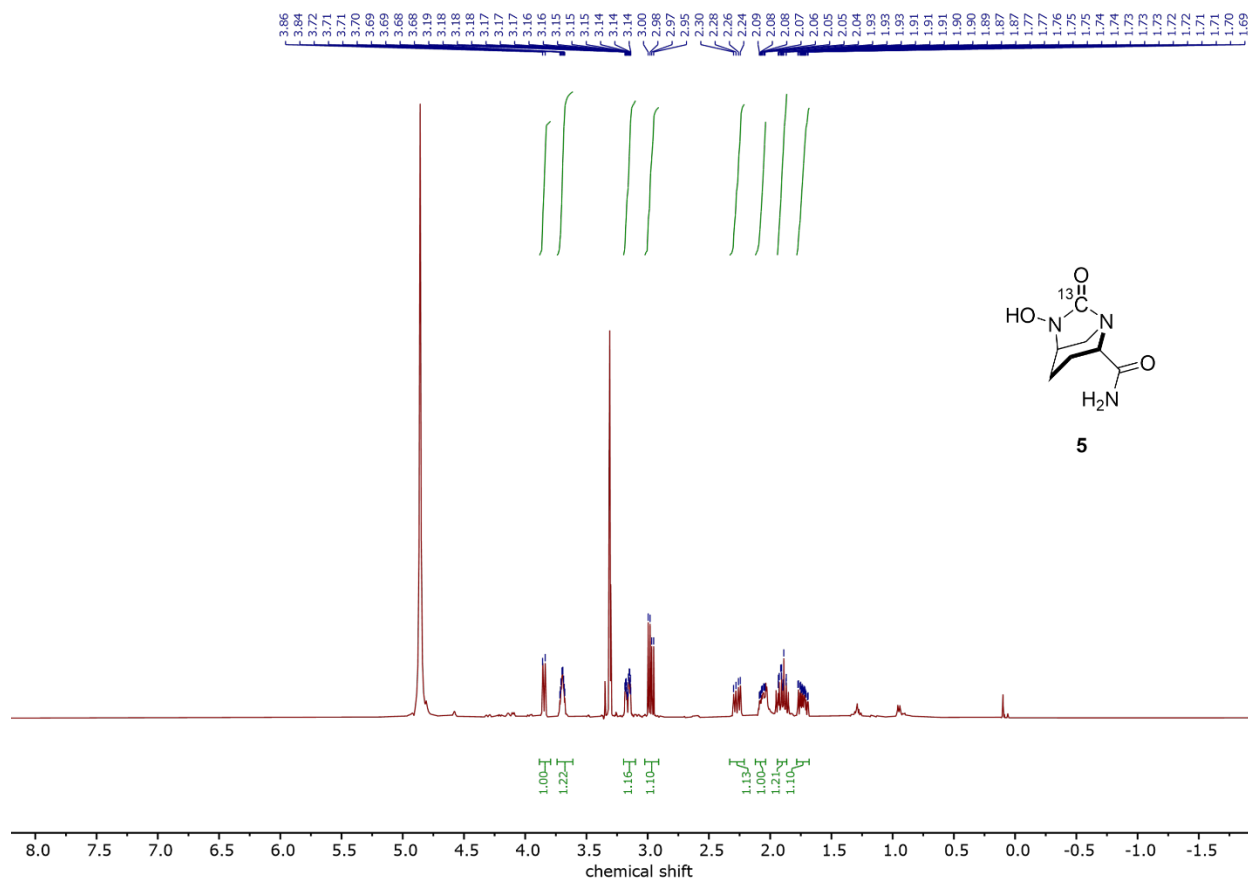


Figure S21. Liquid ^1H NMR spectrum of 5 in CD_3OD .

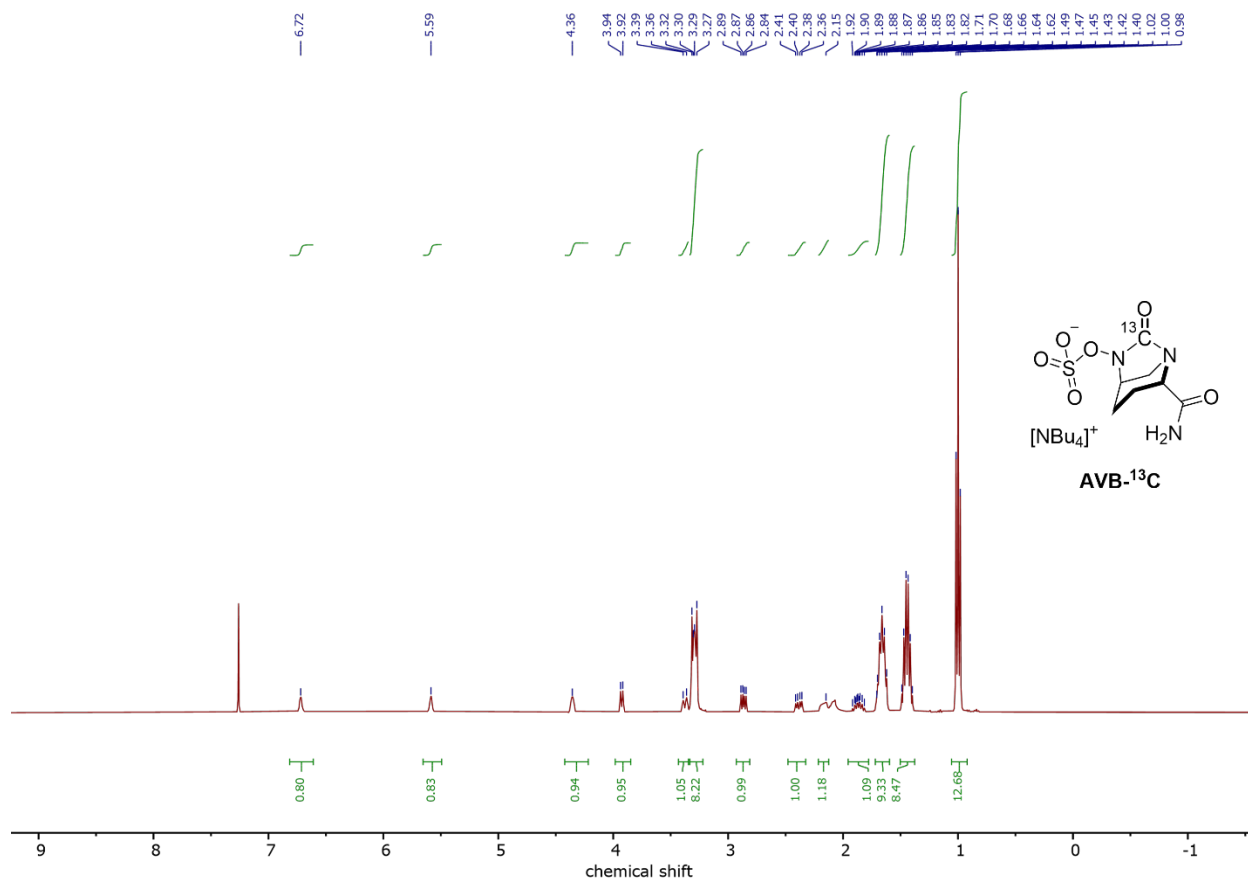


Figure S22. Liquid ^1H NMR spectrum of ^{13}C -labeled AVB in CDCl_3 .

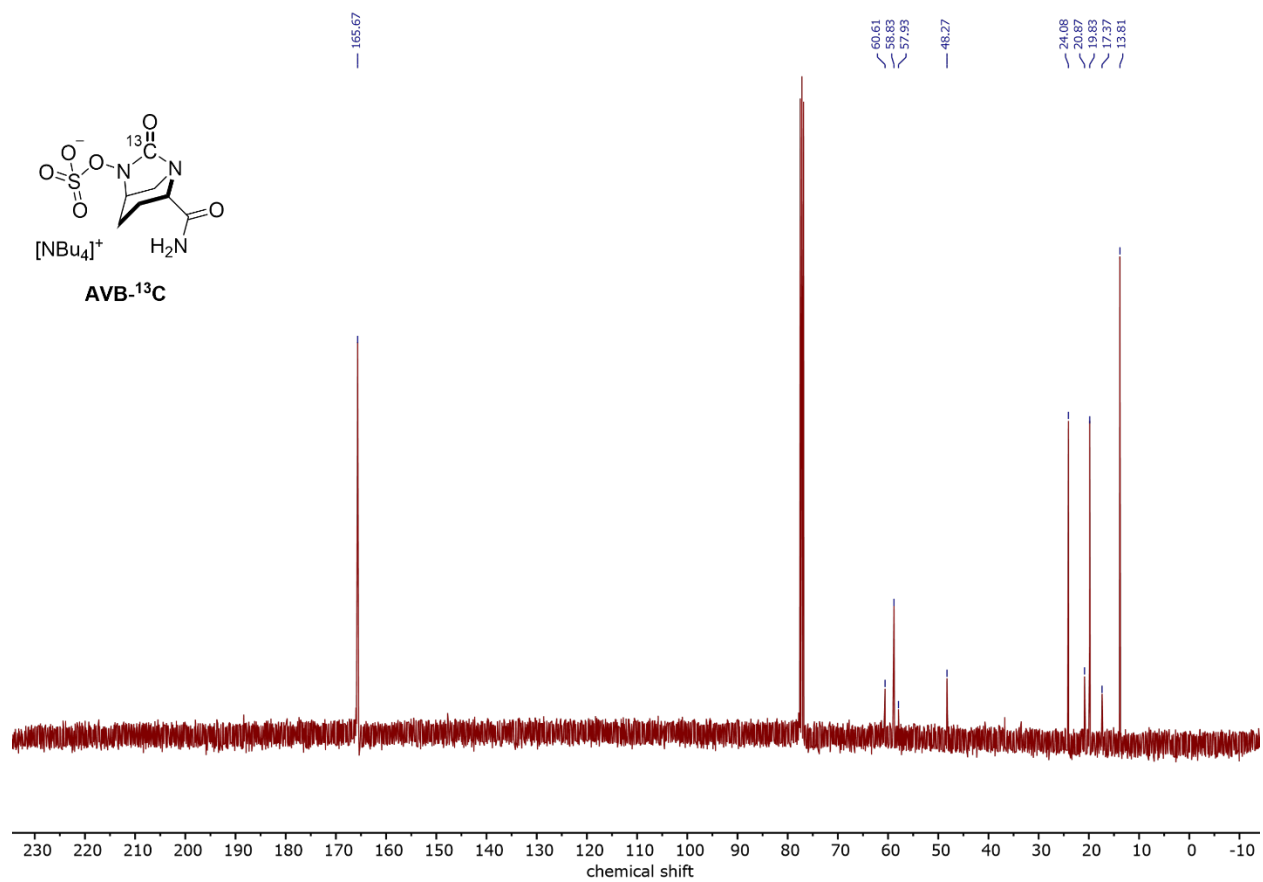


Figure S23. Liquid ¹³C NMR spectrum of ¹³C-labeled AVB in CDCl₃.

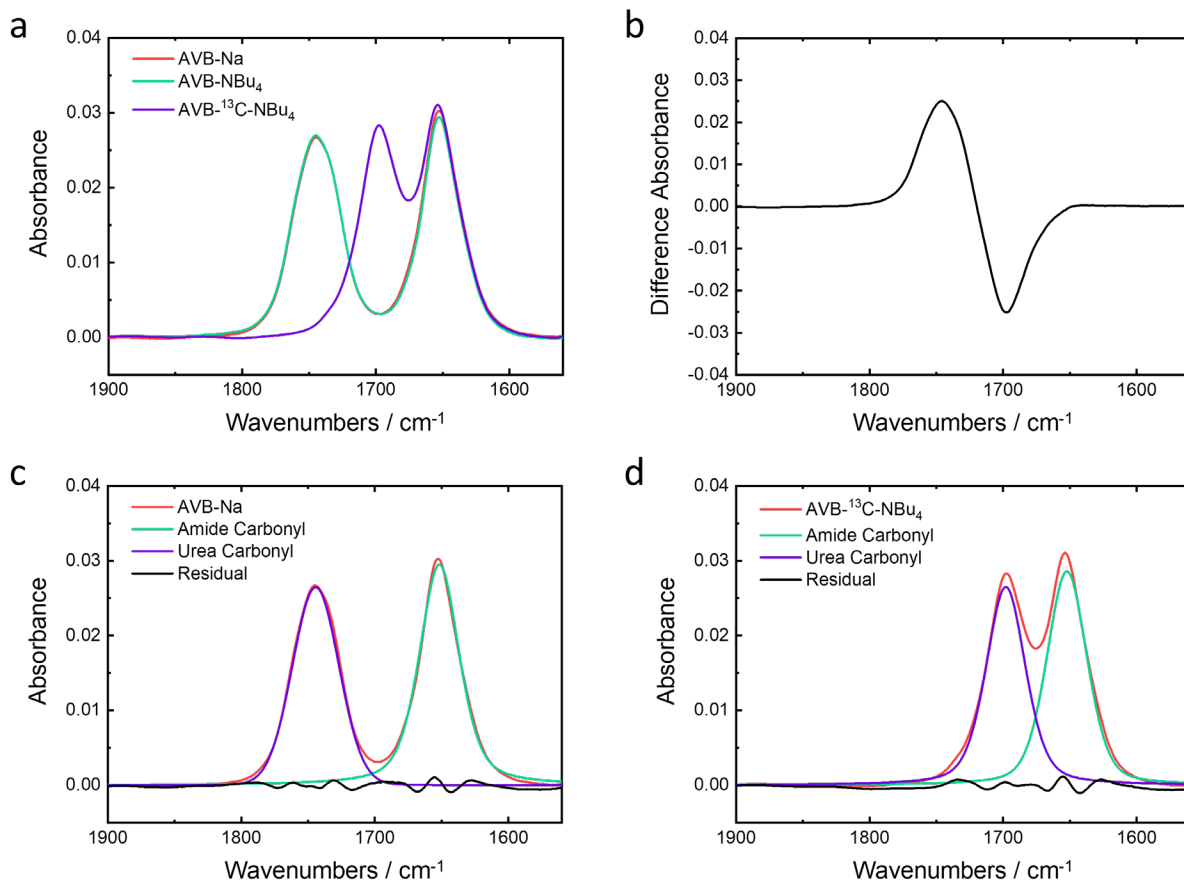


Figure S24. Infrared spectra of 10 mM AVB variants in D₂O buffer (100 mM NaCl, 50 mM KPi, pD 7.4) in the carbonyl region. (a) Overlay of the infrared absorption spectra for AVB sodium salt, AVB tetrabutylammonium salt, and the ¹³C-labeled AVB tetrabutylammonium salt. (b) Difference spectrum between AVB sodium salt and the ¹³C-labeled AVB tetrabutylammonium salt. (c) The spectrum of AVB sodium salt fitted to two peaks, corresponding to the urea C=O and the side amide C=O. (d) The spectrum of the ¹³C-labeled AVB tetrabutylammonium salt fitted to two peaks, corresponding to the urea C=O and the side amide C=O.

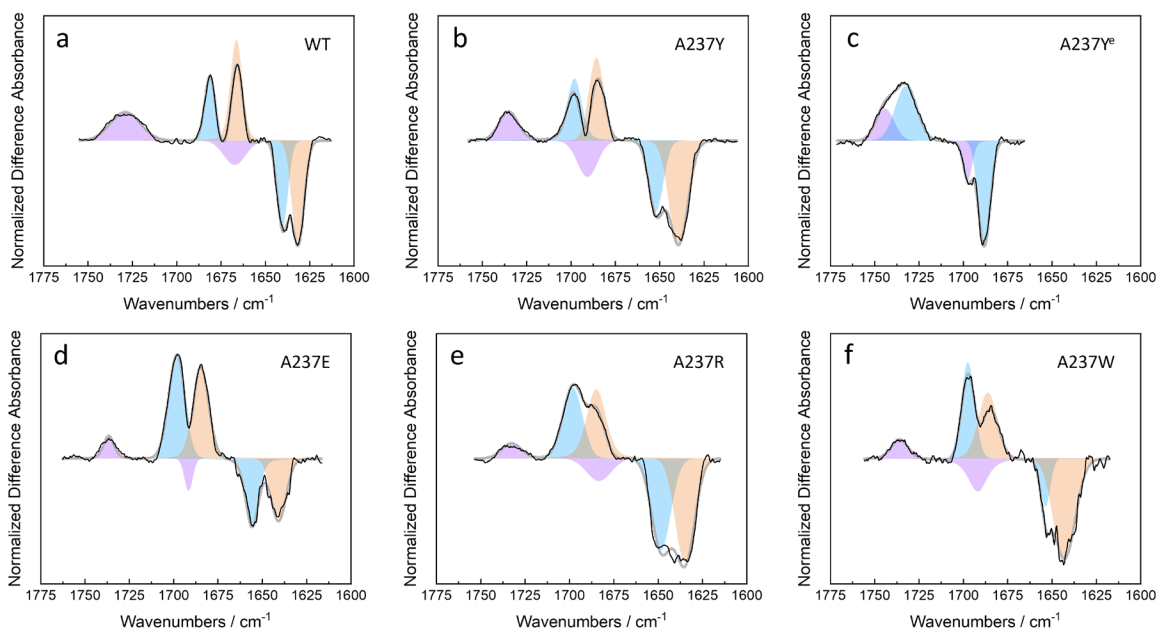


Figure S25. ^{12}C - ^{13}C difference infrared absorption spectra for TEM•AVB (trapped by S70G mutation). (a) WT. (b) A237Y. (c) A237Y^e. (d) A237E. (e) A237R. (f) A237W. The experimental curve (black) is fitted to a sum (grey) of ^{12}C (positive) and ^{13}C (negative) peaks. Peaks belonging to the same positive-negative pair are filled with the same color.

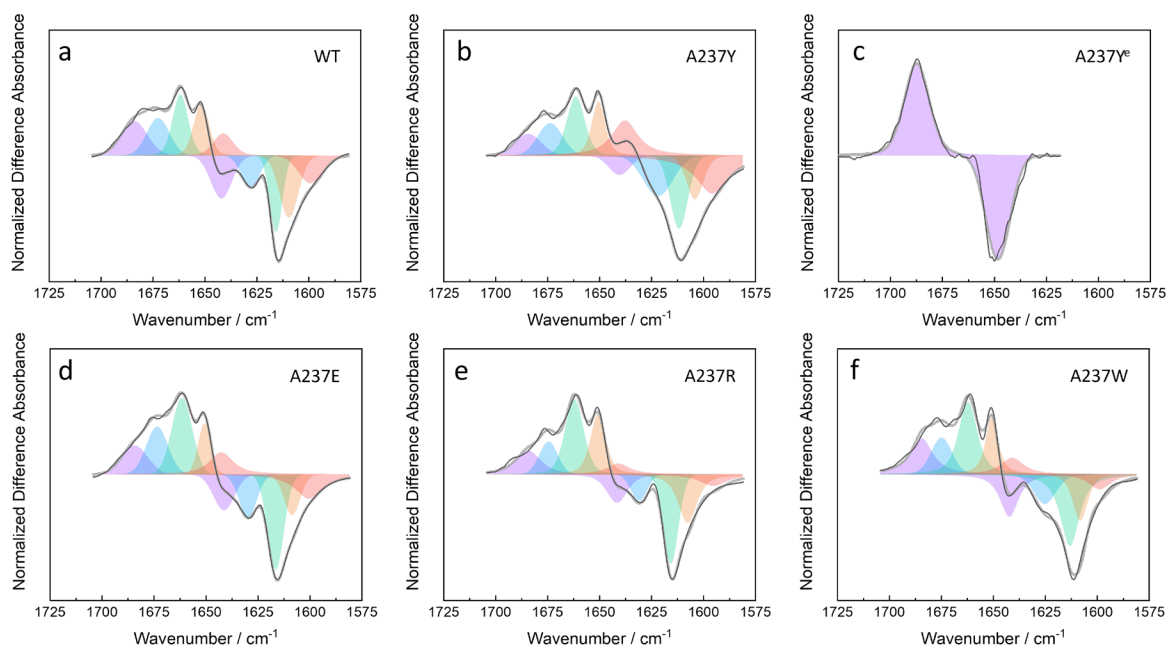


Figure S26. ^{12}C - ^{13}C difference infrared absorption spectra for TEM-AVB. (a) WT. (b) A237Y. (c) A237Y^e. (d) A237E. (e) A237R. (f) A237W. The experimental curve (black) is fitted to a sum (grey) of ^{12}C (positive) and ^{13}C (negative) peaks. Peaks belonging to the same positive-negative pair are filled with the same color.

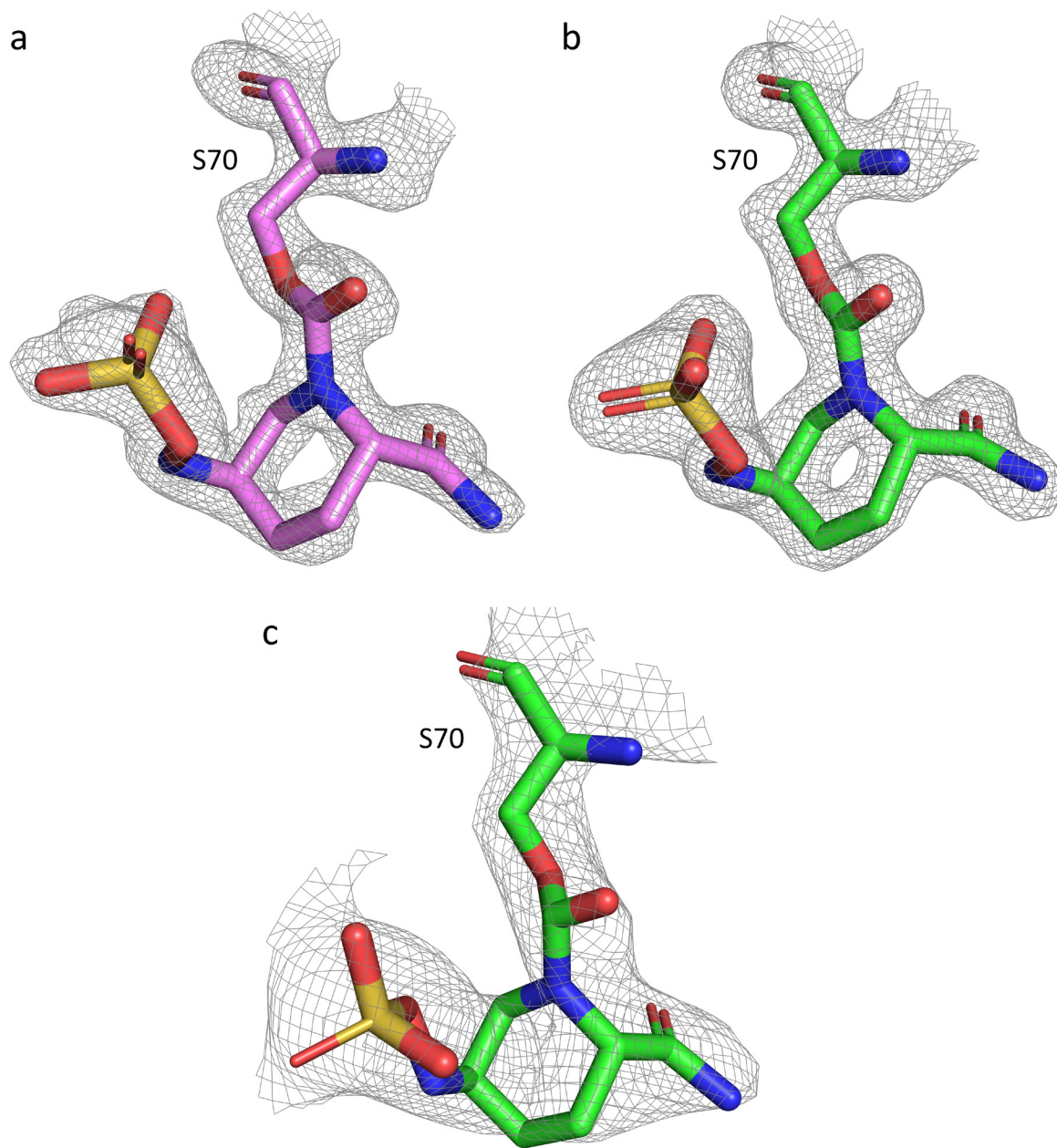


Figure S27. Conformation of AVB bound to TEM. (a) WT (PDB: 8DE0). (b) A237Y (PDB: 8DE1). (c) A237Y at room temperature (PDB: 8DE2). The electron density maps of AVB and S70 ($2mF_o-DF_c$, 1.5σ) are depicted.

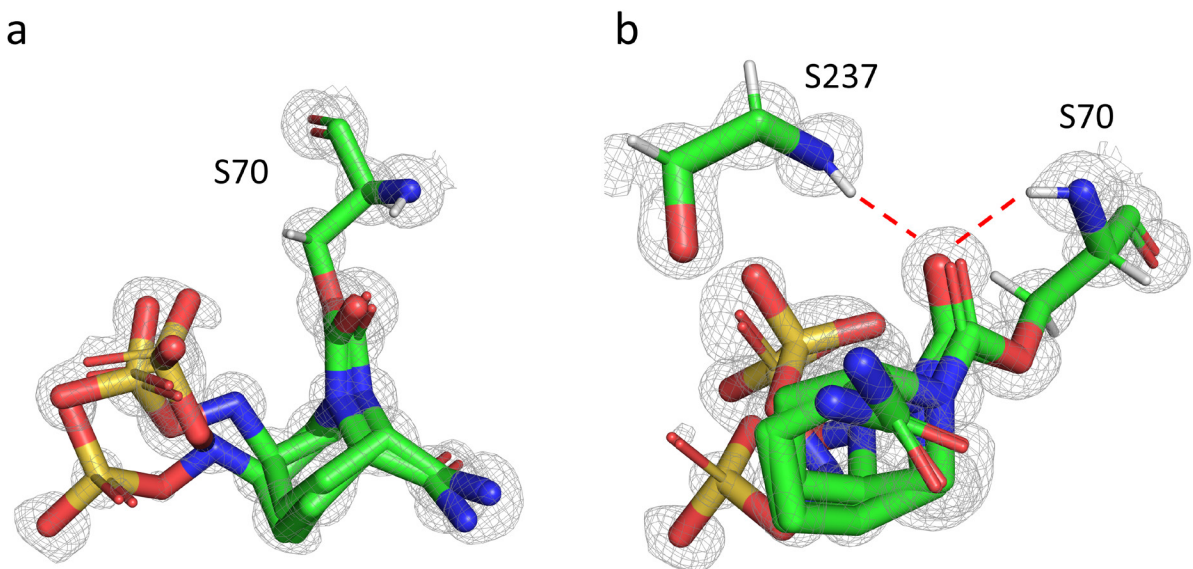


Figure S28. Conformations of AVB bound to CTX-M-14 solved at 0.83 Å (PDB: 6mz2)⁴⁶. (a) View focusing on three conformations of the sulfate group. (b) View showing the two key H-bonds. The O–N distances between the carbamate C=O and the backbone amides vary from 2.79(1) to 3.01(1) for the H-bond to S237 and from 2.80(1) to 2.55(1) for the H-bond to S70. The electron density maps ($2mF_o-DF_c$, 1.0σ) are depicted.

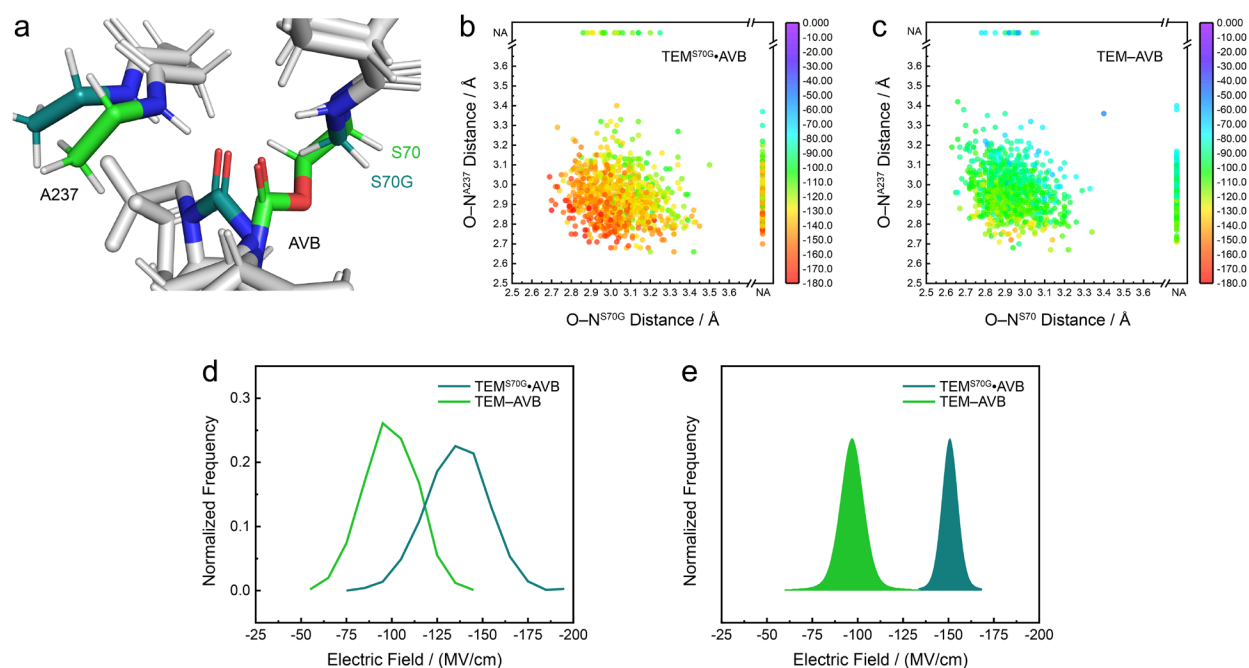


Figure S29. Polarizable MD simulations and electric field calculations on WT TEM•AVB (trapped by S70G mutation) and TEM–AVB. (a) Representative frames of TEM^{S70G}•AVB (dark green) and TEM–AVB (bright green) overlapped based on the whole protein structures. The orientation of AVB’s C=O changes after the covalent bond formation. (b,c) Plots of H-bond lengths and electric field magnitudes for AVB’s reactive C=O in TEM^{S70G}•AVB (b) and TEM–AVB (c). H-bonds were defined as those with O–N distance < 3.5 Å and H–N–O angle < 30°. For those missing a qualified H-bond, the data are presented on the top and right side with bond lengths shown as “NA”. The electric fields were calculated using the AMOEBA/BIO18 force field. (d,e) Magnitudes of the electric fields experienced by AVB’s reactive C=O, as calculated using polarizable force fields on MD frames (d), and as obtained from infrared spectroscopy (the largest-field population duplicated from Figure 3f,g) (e). The calculated average fields for TEM^{S70G}•AVB and TEM–AVB are -136 and -99 MV/cm, respectively. The experimentally measured fields for TEM^{S70G}•AVB and TEM–AVB are -150 and -97 MV/cm, respectively.

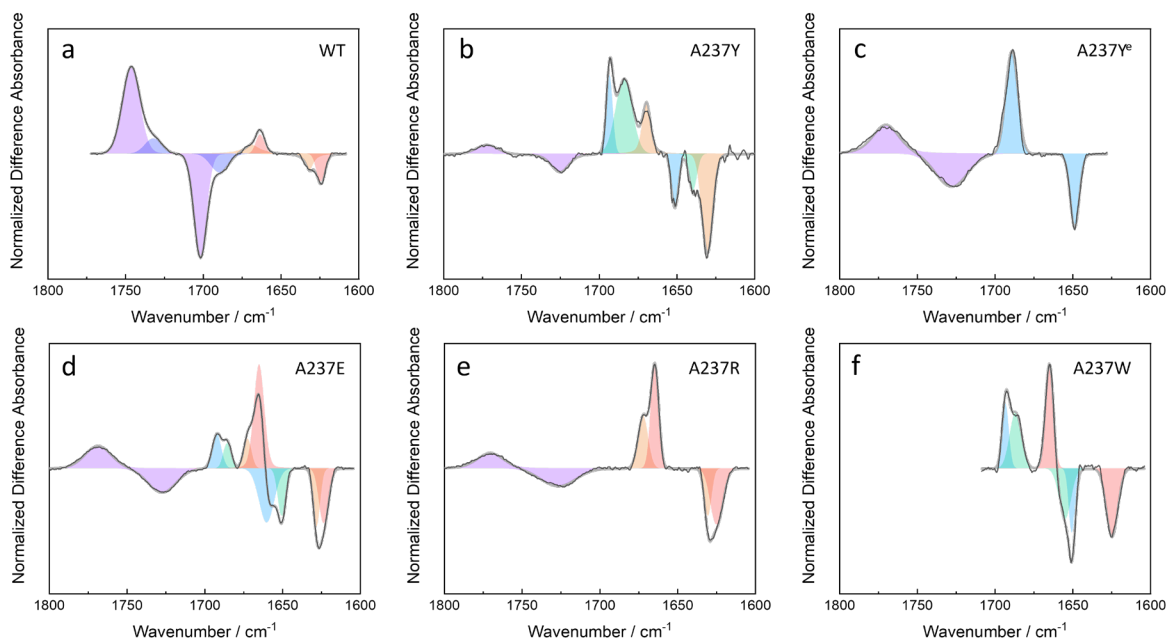


Figure S30. ^{12}C - ^{13}C difference infrared absorption spectra for TEM•PenG (trapped by S70G mutation). (a) WT. (b) A237Y. (c) A237Y^c. (d) A237E. (e) A237R. (f) A237W. The experimental curve (black) is fitted to a sum (grey) of ^{12}C (positive) and ^{13}C (negative) peaks. Peaks belonging to the same positive-negative pair are filled with the same color.

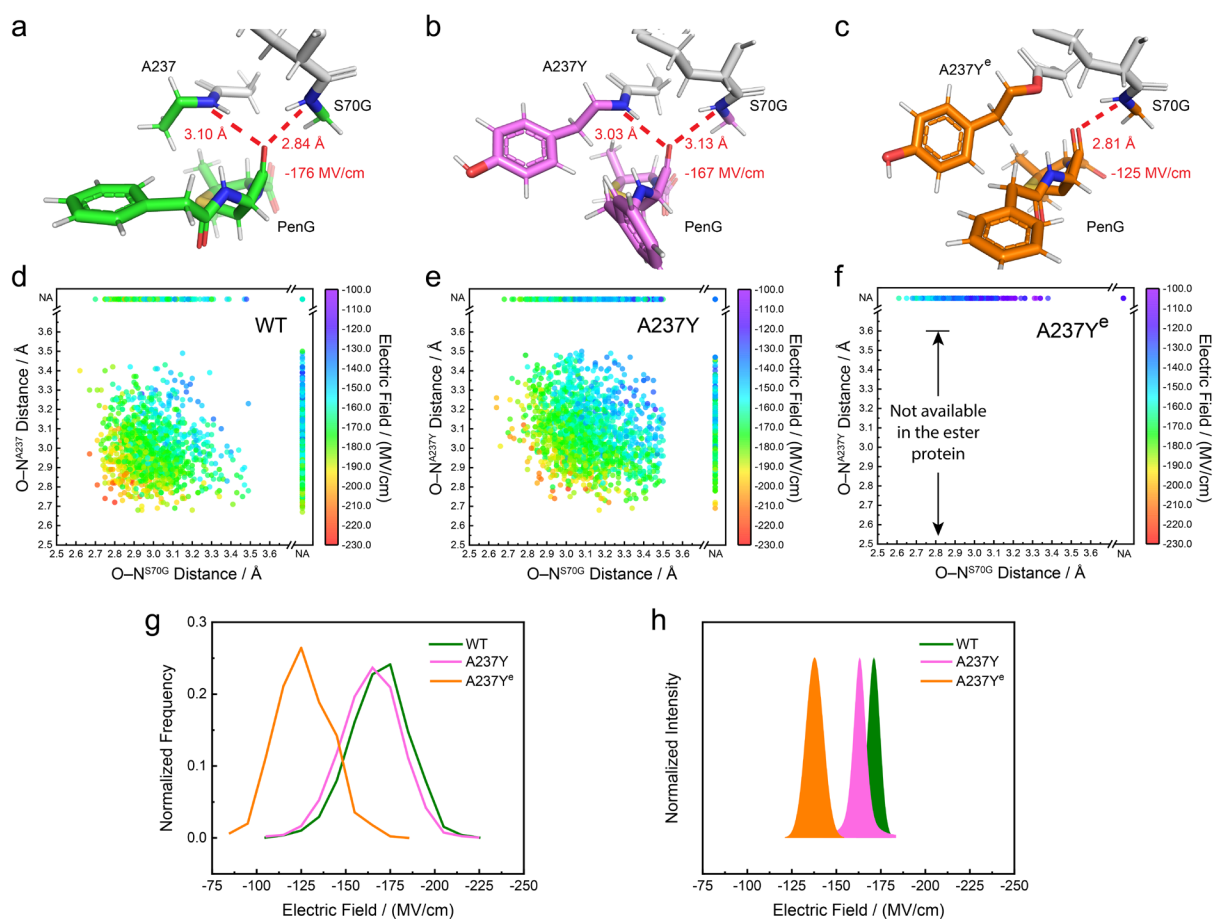


Figure S31. Polarizable MD simulations and electric field calculations on TEM•PenG (trapped by S70G mutation). (a-c) Representative frames of WT (a), A237Y (b), and A237Y^e (c). The key H-bonds are highlighted in red dashed lines and labeled with their bond lengths and electric fields exerted onto PenG’s β -lactam C=O. The electric fields were calculated using the AMOEBABIO18 force field. (d-f) Plots of H-bond lengths and electric field magnitudes for PenG’s β -lactam C=O in WT (d), A237Y (e), and A237Y^e (f). H-bonds were defined as those with O-N distance < 3.5 Å and H-N-O angle $< 30^\circ$. For those missing a qualified H-bond, the data are presented on the top and right side with bond lengths shown as “NA”. For those missing both H-bonds, the data are presented on the top right corner. All the datapoints in (f) are arranged in one dimension on the top because the O-N^{A237Y} distance for the ester protein is always “NA” and thus the O-N^{S70G} distance becomes the only variable. Compared with the WT, the A237Y mutant displays slightly elongated H-bonds and correspondingly smaller electric fields. A237Y^e possesses at most one H-bond and shows correspondingly large drops in field magnitudes. (g,h) Magnitudes of the electric fields experienced by PenG’s β -lactam C=O in WT, A237Y, and A237Y^e, as calculated using polarizable force fields on MD frames (g), and as obtained from infrared spectroscopy (the largest-field population duplicated from Figure 3h) (h). The calculation shows similar trends compared to the experimental results. The calculated average fields for WT, A237Y, and A237Y^e are -169, -164, and -127 MV/cm, respectively. The experimentally measured fields for WT, A237Y, and A237Y^e are -171, -163, and -138 MV/cm, respectively.

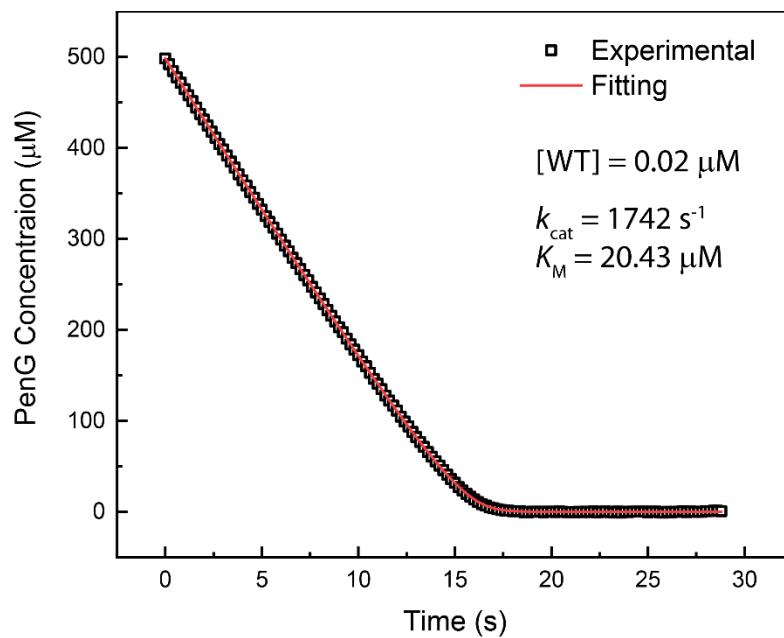


Figure S32. Full-time kinetic measurement on PenG hydrolysis catalyzed by TEM-1. The experimental curve was fitted to eq. 6, giving a fitted value of k_{cat} and K_{M} .

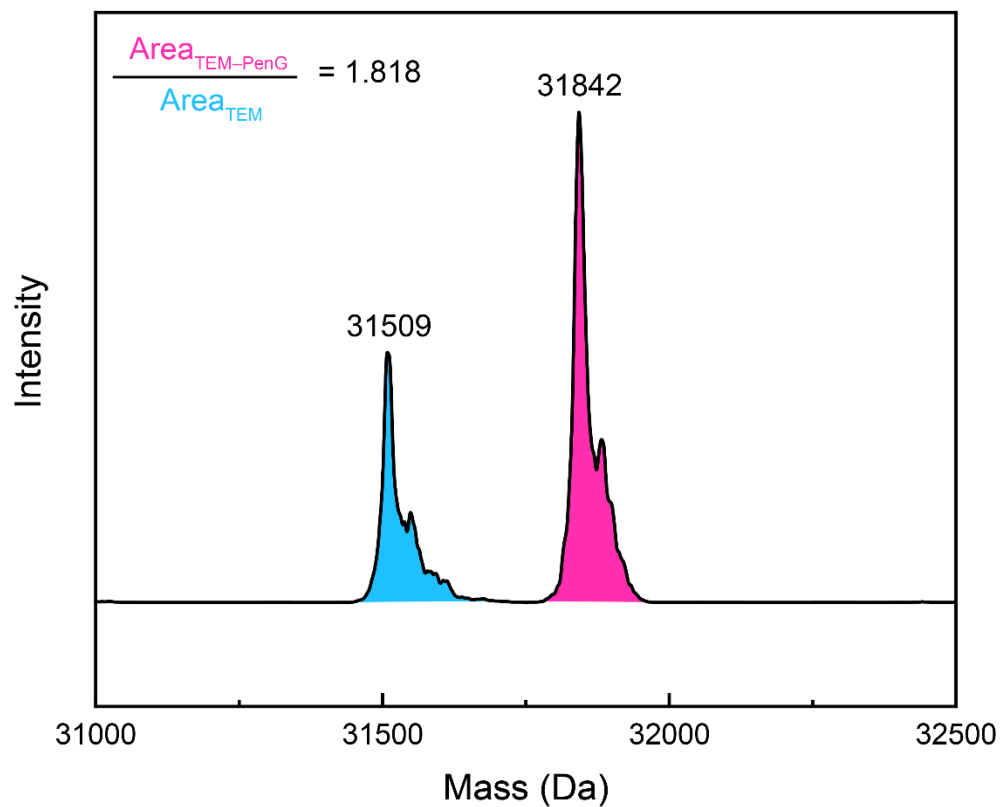


Figure S33. Mass spectrum of a mixture of PenG and TEM-1 quenched at a steady state. The peak area confers the concentration ratio between TEM and TEM–PenG, which can be used to determine k_{ac} according to eq. 10.

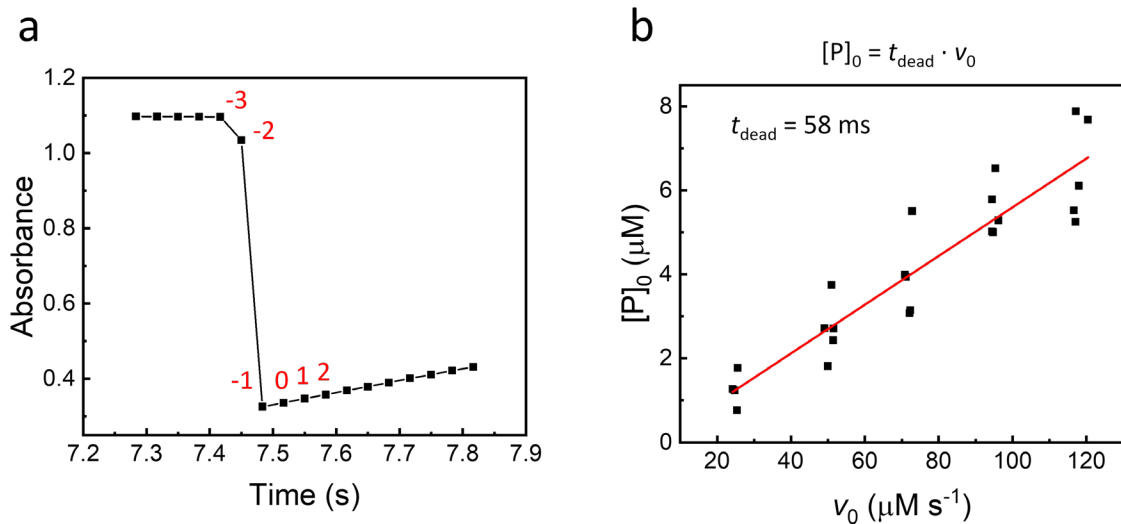


Figure S34. Dead-Time measurement of the stopped-flow apparatus. (a) Jump in absorbance when reactants were mixed using the stopped-flow technique in a typical kinetic experiment. Counting from the last data point that has not been affected by mixing ("-3"), we choose the datapoint "0" as the point of time zero. (b) Plot of the product concentration at time zero $[P]_0$ against the reaction rate at time zero v_0 for nitrocefin hydrolysis by the WT TEM-1. The slope of a linear regression affords the value of the dead time t_{dead} .

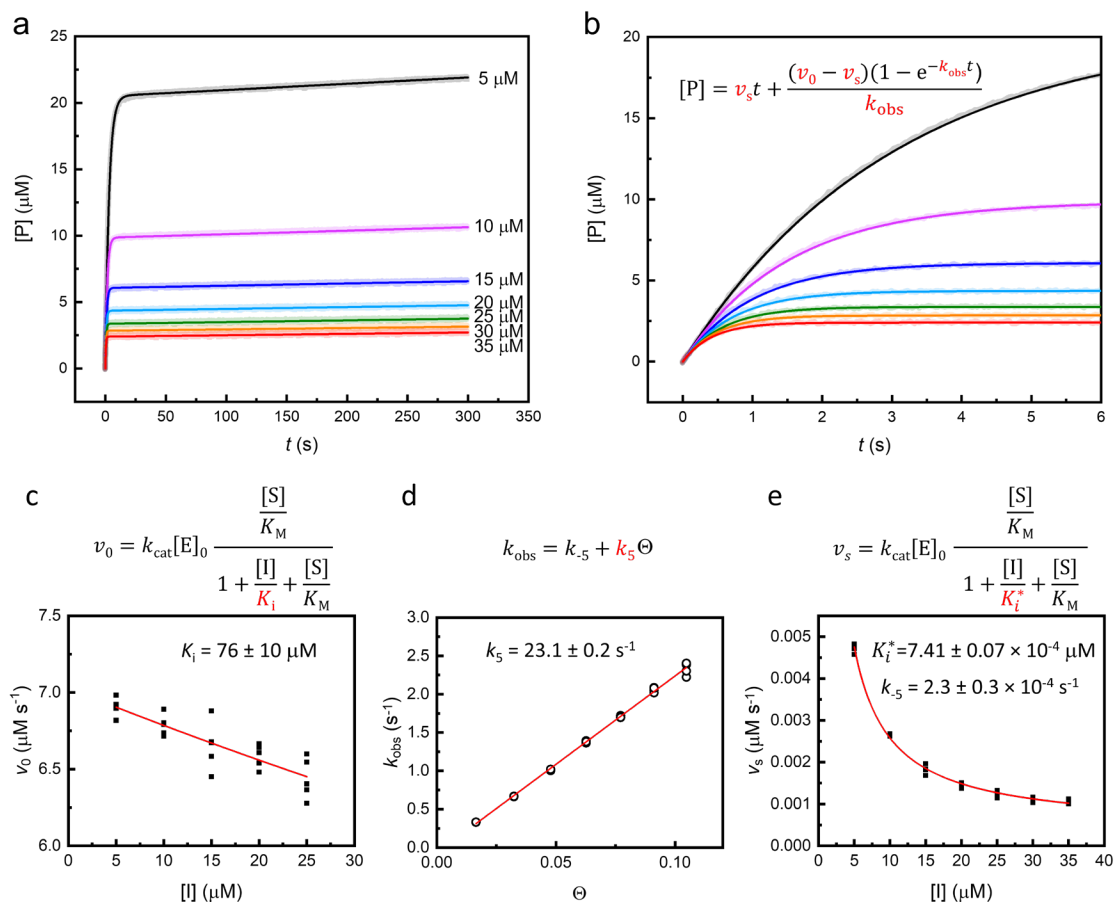


Figure S35. Kinetic measurement on AVB inhibition of TEM-1 using nitrocefin as the substrate. (a) Formation of product over time as a function of AVB concentration ranging from 5 μM to 35 μM . For each concentration of AVB, multiple experiments were run but shown here is only one experimental result for simplicity. The thicker, lighter curves are experimental data while the thinner, darker curves are the essentially identical fitting results according to eq. 13, giving v_0 , v_s , and k_{obs} . (b) Selected window of (a) highlighting the initial product formation. (c) Plot of v_0 against AVB concentration, which was fitted to eq. 17, giving K_i . (d) Plot of k_{obs} against Θ , the partition term defined in eq. 22. The plot was fitted to eq. 23, giving k_5 . (e) Plot of v_s against AVB concentration, which was fitted to eq. 20, giving K_i^* , which in turn was used to calculate k_5 .

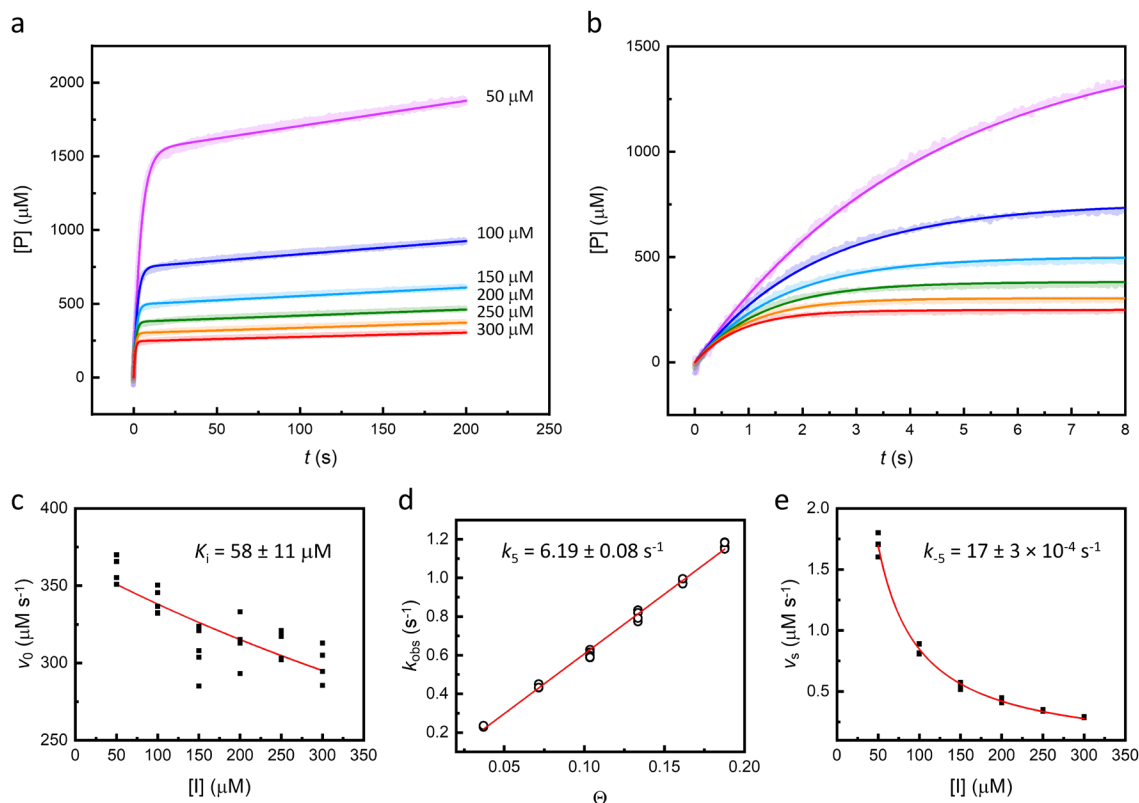


Figure S36. Kinetic measurement on AVB inhibition of A237Y TEM-1 using PenG as the substrate. (a) Formation of product over time as a function of AVB concentration ranging from 50 μM to 300 μM . The $[P]$ was scaled to an $[E]_0$ of 1 μM . For each concentration of AVB, multiple experiments were run but shown here is only one experimental result for simplicity. The thicker, lighter curves are experimental data while the thinner, darker curves are the fitting results according to eq. 13, giving v_0 , v_s , and k_{obs} . (b) Selected window of (a) highlighting the initial product formation. (c) Plot of v_0 against AVB concentration, which was fitted to eq. 17, giving K_i . (d) Plot of k_{obs} against Θ , the partition term defined in eq. 22. The plot was fitted to eq. 23, giving k_5 . (e) Plot of v_s against AVB concentration, which was fitted to eq. 20, giving K_i^* , which in turn was used to calculate k_{-5} .

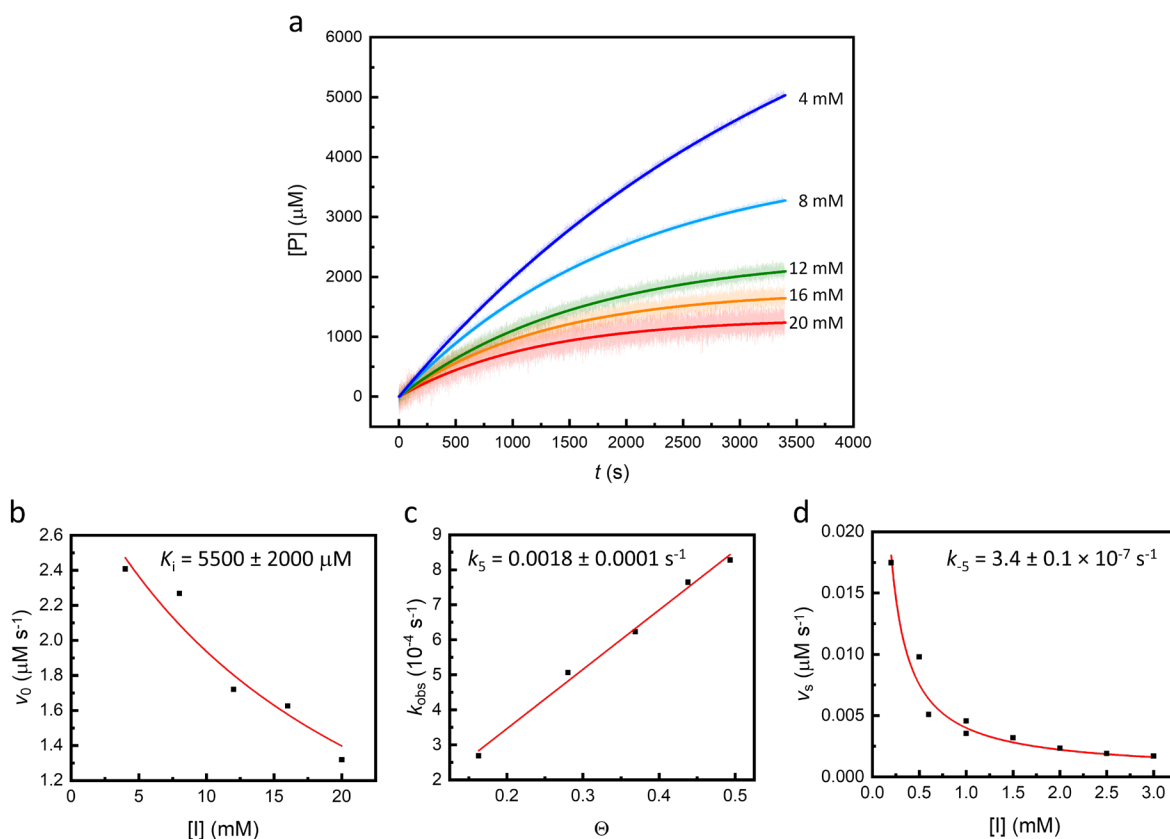


Figure S37. Kinetic measurement on AVB inhibition of A237Y^c TEM-1 using PenG as the substrate. (a) Formation of product over time as a function of AVB concentration ranging from 4 mM to 20 mM. The $[P]$ was scaled to an $[E]_0$ of $1 \mu\text{M}$. For each concentration of AVB, multiple experiments were run but shown here is only one experimental result for simplicity. The thicker, lighter curves are experimental data while the thinner, darker curves are the fitting results according to eq. 13, giving v_0 , v_s , and k_{obs} . (b) Plot of v_0 against AVB concentration, which was fitted to eq. 17, giving K_i . (c) Plot of k_{obs} against Θ , the partition term defined in eq. 22. The plot was fitted to eq. 23, giving k_5 . (d) Plot of v_s against AVB concentration, which was fitted to eq. 20, giving K_i^* , which in turn was used to calculate k_{-5} .

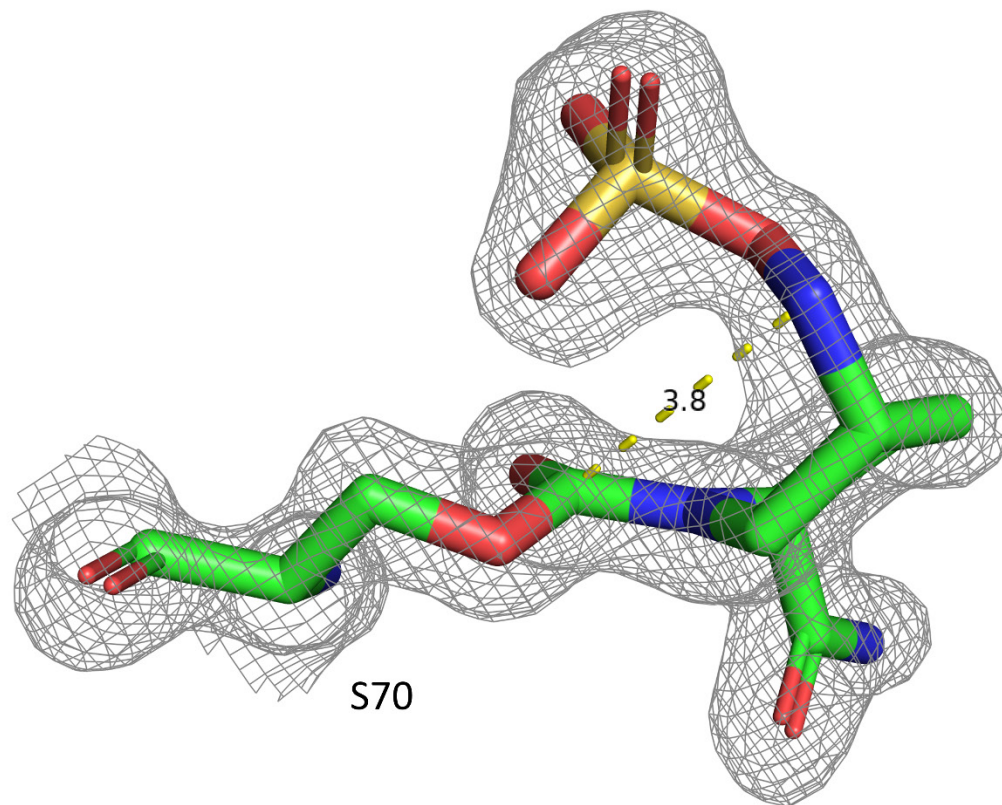


Figure S38. Crystal structure of WT TEM-AVB (PDB: 8DE0) showing the bad positioning of the N atom as the nucleophile for AVB recyclization. The electron density maps ($2mF_o-DF_c$, 1.5σ) are depicted.

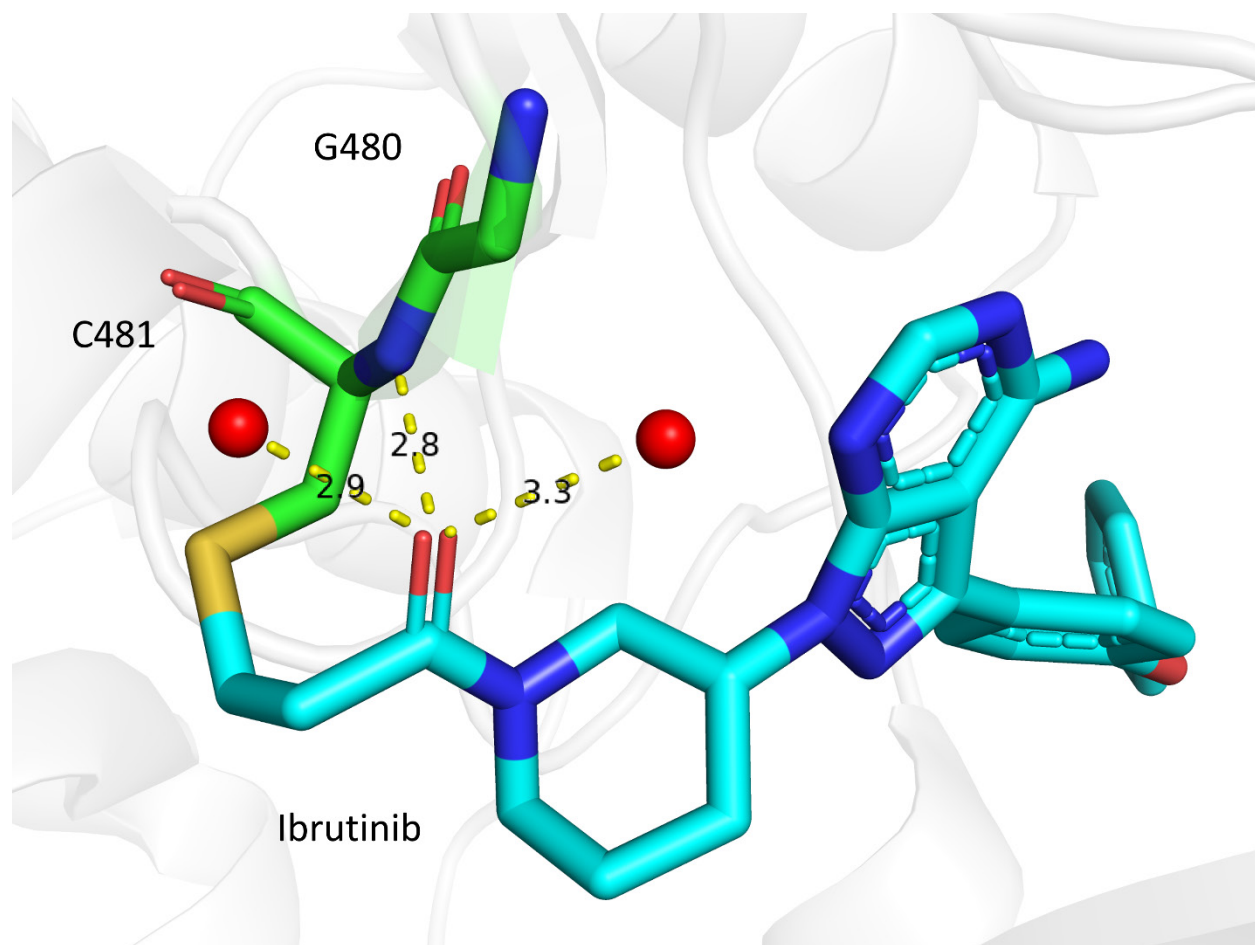


Figure S39. Crystal structure of ibrutinib bound to BTK1 (PDB: 5P9J)⁴⁷.

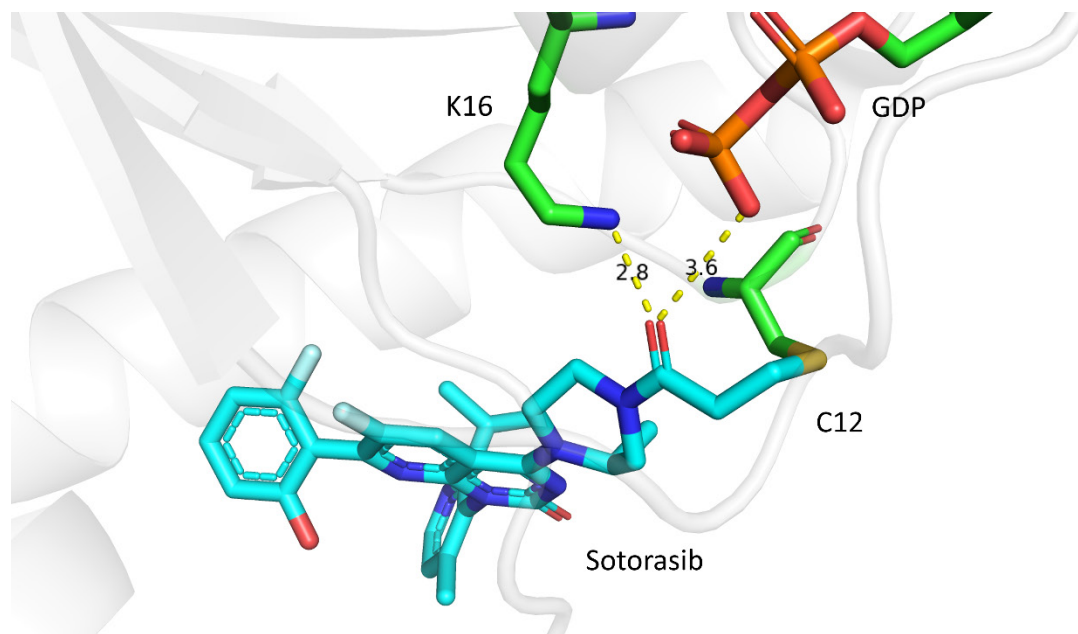


Figure S40. Crystal structure of sotorasib bound to KRAS-G12C (PDB: 6OIM)⁴⁸.

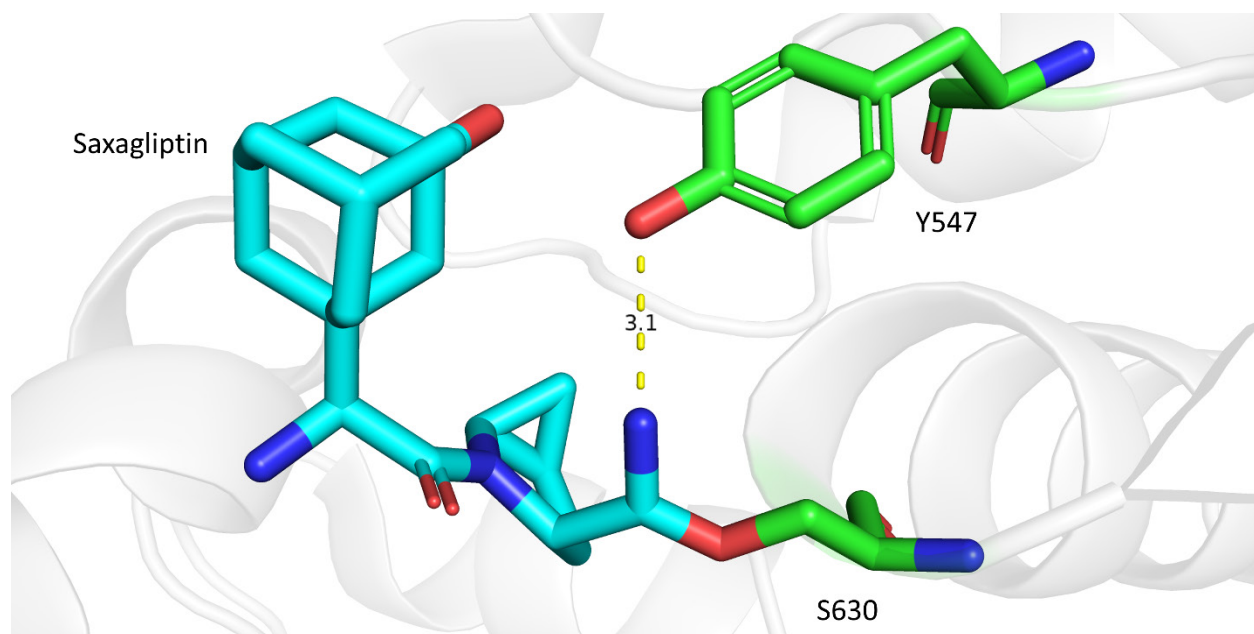


Figure S41. Crystal structure of saxagliptin bound to DPP-IV (PDB: 3BJM)⁴⁹.

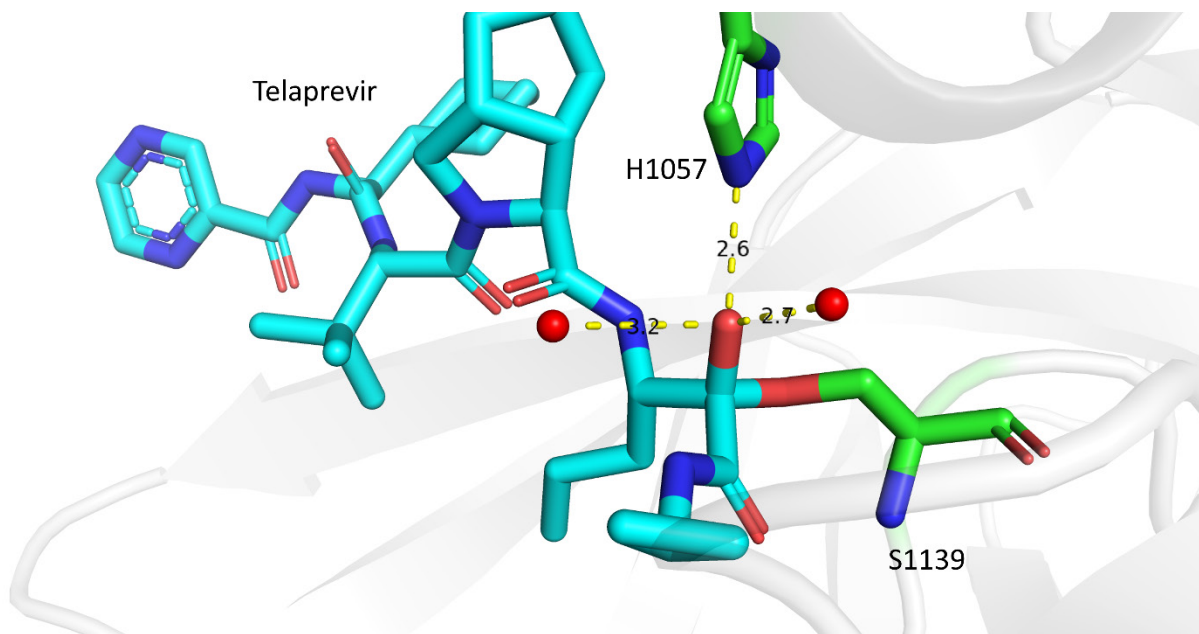


Figure S42. Crystal structure of telaprevir bound to NS3/4A-protease (PDB: 3SV6)⁵⁰.

Table S1. Kinetic parameters for PenG hydrolysis by TEM-1

	K_M (μM)	k_{cat} (s^{-1})	k_{ac} (s^{-1}) ^a	k_3 (s^{-1}) ^a
WT	22 \pm 1	1774 \pm 43	4941 [4784, 5086]	2769 [2697, 2843]
A237Y	261 \pm 3	793 \pm 4	2838 [2740, 2940]	1101 [1084, 1118]
A237Y ^c	1539 \pm 1 ^b	4.54 \pm 0.04 ^b	86.1 [69.2, 97.0]	4.80 [4.75, 4.87]
A237E	1967 \pm 20	1168 \pm 14	5857 [5288, 6012]	1466 [1442, 1500]
A237R	258 \pm 15	2044 \pm 64	3265 [3137, 3396]	5462 [5191, 5773]
A237W	366 \pm 5	332 \pm 3	1390 [1366, 1415]	436 [432, 441]

^a k_{ac} and k_3 are shown as median values and their uncertainties are shown as 68.25% confidence interval, equivalent to 1σ .

^b Measured after the addition of 50 μM AVB, which inhibits any amide mutants (such as A237Y) due to the imperfect fidelity in the incorporation of the non-canonical amino acid. Without adding AVB, the apparent k_{cat} was measured as $9.25 \pm 0.55 \text{ s}^{-1}$, indicating a 99% fidelity assuming all mis-incorporated amino acid is Tyr. The apparent K_M was measured as $194 \pm 10 \text{ mM}$. AVB at 50 μM concentration only binds to A237Y^c at a negligible level in the measurement time, according to the inhibition kinetics.

Table S2. Kinetic parameters for AVB inhibition of TEM-1

	K_i (μM)	K_i^* (nM)	k_{cbm} (s^{-1})	k_{rec} (10^{-4}s^{-1})
WT	76 ± 10	0.741 ± 0.007	23.1 ± 0.2	2.3 ± 0.3
A237Y	58 ± 11	15.9 ± 0.2	6.19 ± 0.08	17 ± 3
A237Y ^c	$(5.5 \pm 2.0) \times 10^3$	$(9.9 \pm 1.3) \times 10^2$	$(1.8 \pm 0.1) \times 10^{-3}$	$(3.4 \pm 0.1) \times 10^{-3}$
A237E	$(1.48 \pm 0.25) \times 10^3$	27.7 ± 0.8	4.63 ± 0.23	0.87 ± 0.15
A237R	47 ± 7	8.03 ± 0.04	3.63 ± 0.03	6.2 ± 0.9
A237W	54 ± 11	10.91 ± 0.05	3.31 ± 0.05	6.7 ± 1.3

Table S3. Mass and extinction coefficient of TEM-1 mutants

		ϵ_{280} ($M^{-1} \text{ cm}^{-1}$) ^a	Expected Mass (Da) ^a	Observed Mass (Da) ^b	Observed Mass at high resolution (Da)	
TEM-1	WT	28085	31499	31508		
	S70G	28085	31469	31479		
	WT-AVB		31763	31775		
	WT-PenG		31832	31845		
	A237Y	29575	31591	31600	31588.3	
	A237Y S70G	29575	31561	31564		
	A237Y-AVB		31855	31862 ^c		
	A237Y-PenG		31924	31934		
	A237E	28085	31557	31568		
	A237E S70G	28085	31527	31533		
	A237E AVB		31821	31829 ^c		
	A237E PenG		31890	31901		
	A237W	33585	31614	31622		
	A237W S70G	33585	31584	31588		
	A237W-AVB		31878	31891 ^c		
	A237W-PenG		31947	31956		
	A237R	28085	31584	31589		
	A237R S70G	28085	31554	31556		
	A237R-AVB		31848	31859 ^c		
	A237R-PenG		31917	31924		
	A237Y ^e	29575	31591 ^d (23403, 8205)	31602 ^d (23410, 8210)	31589.4 ^d (23401.2, 8205.7)	
	A237Y ^e S70G	29575	31561 ^d (23374, 8205)	31572 ^d (23381, 8209)		
	A237Y ^e AVB		31855 ^d (23667, 8205)	31878 ^d (23683, 8212) ^c		
	A237Y ^e PenG		31924 ^d (23736, 8205)	31937 ^d (23746, 8209)		
	TEM-1-native	WT	28085	28934	28941	
		A237Y	29575	29026	29034	

^a Calculated using ProtParam tool at <https://web.expasy.org/protparam/>

^b Proteins of ~ 30 kDa have a systematic error within +15 Da, depending on instrument status.

^c Higher mass might be observed because the infrared samples were used for measuring mass spectra, which have been partially deuterium exchanged.

^d Values in brackets correspond to the protein fragments generated by backbone ester hydrolysis.

Table S4. X-ray diffraction data and refinement statistics of WT TEM-1

Protein	WT
PDB entry	7U6Q
Data collection statistics	
Beamline	BL 12-2
Wavelength (Å)	0.97946
Resolution range (Å)	39.23 – 1.90 (1.95 – 1.90)
Space group	P 2 ₁ 2 ₁ 2 ₁ (No.19)
Unit cell dimensions a, b, c, (Å) α , β , γ (°)	60.73, 96.33, 154.20 90, 90, 90
Matthews coefficient	2.59
Solvent content (%)	52.60
Total observations	948,280 (70,789)
Unique observations	71,785 (5,232)
Multiplicity	13.210 (13.530)
Completeness (%)	99.6 (99.9)
Mean I/s(I)	8.23 (1.50)
Wilson B-factor (Å ²)	22.0
Anisotropy	0.192
R _{merge}	0.288 (2.512)
R _{meas}	0.300 (2.610)
CC _{1/2}	0.997 (0.640)
Refinement statistics	
Reflections used	71,756 (2,565)
Reflections used for R _{free}	3,588 (134)
R _{work}	0.1911 (0.3077)
R _{free}	0.2385 (0.3395)
Number of non-H atoms	6,960
Protein	6,116
Ligand	30
Solvent	814
Protein residues	790
RMSD bond lengths (Å)	0.014
RMSD bond angles (°)	1.78
Ramachandran favored (%)	98.21
Ramachandran allowed (%)	1.79
Ramachandran outliers (%)	0.00
Rotamer outliers (%)	2.12
Clashscore	2.52
Average B factor (Å ²)	24.40
Protein	23.18
Ligand	38.83
Solvent	32.99

Table S5. X-ray diffraction data and refinement statistics of A237Y TEM-1

Protein	A237Y
PDB entry	8DDZ
Data collection statistics	
Beamline	BL 12-2
Wavelength (Å)	0.97946
Resolution range (Å)	38.37 – 1.45 (1.50 – 1.46)
Space group	P 1 2 ₁ 1 (No.4)
Unit cell dimensions a, b, c, (Å) α , β , γ (°)	60.61, 83.77, 95.66 90, 90.23, 90
Matthews coefficient	2.09
Solvent content (%)	41.12
Total observations	2,273,538 (164,682)
Unique observations	164,606 (11,707)
Multiplicity	13.812 (14.067)
Completeness (%)	97.6 (95.7)
Mean I/s(I)	9.51 (1.56)
Wilson B-factor (Å ²)	15.5
Anisotropy	0.254
R _{merge}	0.167 (2.002)
R _{meas}	0.174 (2.076)
CC _{1/2}	0.998 (0.729)
Refinement statistics	
Reflections used	164,606 (3,699)
Reflections used for R _{free}	8,086 (206)
R _{work}	0.1769 (0.1858)
R _{free}	0.2121 (0.2282)
Number of non-H atoms Protein Ligand Solvent	8,900 8,183 0 717
Protein residues	1,048
RMSD bond lengths (Å)	0.018
RMSD bond angles (°)	1.70
Ramachandran favored (%)	97.88
Ramachandran allowed (%)	2.12
Ramachandran outliers (%)	0.00
Rotamer outliers (%)	1.25
Clashscore	2.26
Average B factor (Å ²) Protein Ligand Solvent	18.62 17.92 NA 26.58

Table S6. X-ray diffraction data and refinement statistics of WT TEM-1–AVB

Protein	WT–AVB
PDB entry	8DE0
Data collection statistics	
Beamline	BL 12-2
Wavelength (Å)	0.97946
Resolution range (Å)	38.33 – 1.72 (1.77 – 1.73)
Space group	P 1 2 ₁ 1 (No.4)
Unit cell dimensions a, b, c, (Å) α , β , γ (°)	60.65, 83.69, 95.57 90, 90.19, 90
Matthews coefficient	2.08
Solvent content (%)	40.77
Total observations	1,347,709 (80,926)
Unique observations	99,749 (7,221)
Multiplicity	13.51 (11.21)
Completeness (%)	99.0 (97.7)
Mean I/s(I)	9.060 (1.620)
Wilson B-factor (Å ²)	21.07
Anisotropy	0.044
R _{merge}	0.190 (1.647)
R _{meas}	0.197 (1.724)
CC _{1/2}	0.998 (0.671)
Refinement statistics	
Reflections used	99,749 (2,557)
Reflections used for R _{free}	5,045 (118)
R _{work}	0.1727 (0.1604)
R _{free}	0.1981 (0.2141)
Number of non-H atoms	9,284
Protein	8,149
Ligand	68
Solvent	1,067
Protein residues	1,048
RMSD bond lengths (Å)	0.013
RMSD bond angles (°)	1.65
Ramachandran favored (%)	97.98
Ramachandran allowed (%)	2.02
Ramachandran outliers (%)	0.00
Rotamer outliers (%)	1.26
Clashscore	3.52
Average B factor (Å ²)	21.71
Protein	20.37
Ligand	21.23
Solvent	31.94

Table S7. X-ray diffraction data and refinement statistics of A237Y TEM-1–AVB

Protein	A237Y–AVB
PDB entry	8DE1
Data collection statistics	
Beamline	BL 12-2
Wavelength (Å)	0.97946
Resolution range (Å)	38.30 – 1.56 (1.60 – 1.56)
Space group	P 1 2 ₁ 1 (No.4)
Unit cell dimensions a, b, c, (Å) α , β , γ (°)	60.61, 83.57, 95.86 90, 90.44, 90
Matthews coefficient	2.07
Solvent content (%)	40.64
Total observations	1,825,431 (123,641)
Unique observations	135,097 (9,774)
Multiplicity	13.51 (12.65)
Completeness (%)	99.5 (97.4)
Mean I/s(I)	7.97 (1.59)
Wilson B-factor (Å ²)	16.4
Anisotropy	0.546
R _{merge}	0.201 (1.829)
R _{meas}	0.209 (1.905)
CC _{1/2}	0.998 (0.733)
Refinement statistics	
Reflections used	135,091 (6,217)
Reflections used for R _{free}	6,817 (319)
R _{work}	0.2065 (0.3257)
R _{free}	0.2214 (0.3410)
Number of non-H atoms	9,507
Protein	8,169
Ligand	68
Solvent	1,270
Protein residues	1,052
RMSD bond lengths (Å)	0.013
RMSD bond angles (°)	1.20
Ramachandran favored (%)	97.99
Ramachandran allowed (%)	2.01
Ramachandran outliers (%)	0.00
Rotamer outliers (%)	1.48
Clashscore	7.28
Average B factor (Å ²)	18.87
Protein	17.60
Ligand	20.51
Solvent	26.97

Table S8. X-ray diffraction data and refinement statistics of A237Y TEM-1–AVB at RT

Protein	A237Y–AVB at RT
PDB entry	8DE2
Data collection statistics	
Beamline	BL 12-1
Wavelength (Å)	0.97946
Resolution range (Å)	39.33 – 2.45 (2.51 – 2.45)
Space group	P 1 2 ₁ 1 (No.4)
Unit cell dimensions a, b, c, (Å) α , β , γ (°)	60.93, 86.07, 96.94 90, 90.00, 90
Matthews coefficient	2.17
Solvent content (%)	43.31
Total observations	211,429 (11,647)
Unique observations	35,092 (2,004)
Multiplicity	6.025 (5.812)
Completeness (%)	94.9 (73.5)
Mean I/s(I)	8.54 (1.79)
Wilson B-factor (Å ²)	36.7
Anisotropy	0.853
R _{merge}	0.152 (0.978)
R _{meas}	0.167 (1.073)
CC _{1/2}	0.998 (0.851)
Refinement statistics	
Reflections used	35,092 (1,971)
Reflections used for R _{free}	1,789 (102)
R _{work}	0.2045 (0.3512)
R _{free}	0.2495 (0.4194)
Number of non-H atoms	8,302
Protein	8,132
Ligand	68
Solvent	102
Protein residues	1,052
RMSD bond lengths (Å)	0.004
RMSD bond angles (°)	0.68
Ramachandran favored (%)	97.99
Ramachandran allowed (%)	2.01
Ramachandran outliers (%)	0.00
Rotamer outliers (%)	3.44
Clashscore	9.34
Average B factor (Å ²)	43.53
Protein	43.61
Ligand	40.29
Solvent	39.35

Table S9. Growth of DH10B $\Delta aspC \Delta tyrB$ in the minimal media

Incubation Time (h)	OD ₆₀₀ (no Tyr)	OD ₆₀₀ (1 mM Tyr)
18	0.009	0.218
42	0.012	1.855

Table S10. FTIR data analysis of BODAC

Solvent	Urea Carbonyl				Amide Carbonyl			
	Peak Picking		Curve Fitting		Peak Picking		Curve Fitting	
	Position (cm ⁻¹)	FWHM (cm ⁻¹)						
dibutylether	1771.8	14.2	1771.3	14.7	1707.1	16.4	1705.7	17.4
toluene	1767.5	13.1	1767.2	13.8	1705.9	11.5	1705.6	11.8
THF	1764.7	15.2	1764.4	15.6	1697.7	13.3	1698.2	13.7
DCM	1757.1	21.8	1756.0	23.2	1698.5	15.7	1698.2	16.3
DMSO	1751.6	20.0	1751.1	21.5	1687.6	14.3	1687.7	15.1
water	1722.3	31.7	1722.4	39.6	1652.8	29.7	1651.1	37.3

Table S11. Solvent electric fields projected on the C=O (Urea) in BODAC based on MD simulation

Solvent	Average (MV/cm)	Standard Deviation (MV/cm)
dibutylether	-10.6	5.2
toluene	-15.3	6.0
THF	-20.3	7.1
DCM	-32	12
DMSO	-35.0	9.8
water	-75	22

Table S12. FTIR data analysis of MPC

Solvent	Peak Picking		Curve Fitting	
	Position (cm^{-1})	FWHM (cm^{-1})	Position (cm^{-1})	FWHM (cm^{-1})
hexanes	1715.4	7.5	1715.3	7.6
dibutylether	1711.6	10.1	1711.4	10.3
THF	1705.8	10.7	1705.7	10.8
toluene	1705.3	11.6	1705.2	11.7
DMSO	1694.1	16.4	1694.0	16.4
DCM	1691.7	18.8	1692.0	19.6
water	1658.8	34.0	1657.0	34.7

Table S13. Solvent electric fields projected on the C=O in MPC based on MD simulation

Solvent	Average (MV/cm)	Standard Deviation (MV/cm)
hexanes	-0.04	0.75
dibutylether	-6.4	5.3
THF	-11.8	8.6
toluene	-10.4	6.8
DMSO	-22.7	9.7
DCM	-26	15
water	-75	22

Table S14. The fitting results of the vibrational Stark spectrum of MPC

Peak position (cm^{-1})	FWHM (cm^{-1})	A^a	B^a (cm^{-1})	C^a (cm^{-2})	$ \Delta\mu f$ [$\text{cm}^{-1} /$ (MV/cm)]	$ \Delta\mu ^b$ [$\text{cm}^{-1} /$ (MV/cm)]	f
1696.9	10.5	2.24 $\times 10^{-4}$	1.97 $\times 10^{-3}$	1.85 $\times 10^{-1}$	1.36	0.754	1.80

^a A , B , and C are the fitting coefficients for the Stark spectra, corresponding to the 0th (A), 1st (B), and 2nd (C) derivative contributions respectively. The Stark tuning rates ($|\Delta\mu|f$) can be extracted from the coefficient of the dominant 2nd derivative contribution (C) assuming the difference dipole of the vibrational mode is parallel with its transition dipole moment.

^b $|\Delta\mu|$ was obtained from solvatochromism and MD simulations, see Figure S13.

Table S15. FTIR data analysis of 10 mM AVB solutions in D₂O buffer^a

Solute	Urea Carbonyl				Amide Carbonyl			
	Peak Picking		Curve Fitting		Peak Picking		Curve Fitting	
	Position (cm ⁻¹)	FWHM (cm ⁻¹)						
AVB-Na	1744.7	40.0	1744.3	41.0	1652.5	32.0	1651.7	35.3
AVB- NBu ₄	1745.0	39.9	1744.4	40.9	1652.7	31.3	1651.7	34.1
AVB- ¹³ C- NBu ₄	1697.6	21.7	1698.0	34.9	1653.7	23.7	1652.3	35.5

^a The D₂O buffer is the same used for FTIR spectroscopy for proteins, containing 100 mM NaCl and 50 mM KPi (pD 7.4).

Table S16. Peak fitting of the difference FTIR spectra of TEM•AVB

	¹² C			¹³ C		
	Position (cm ⁻¹)	FWHM (cm ⁻¹)	Lorentzian (%) ^a	Position (cm ⁻¹)	FWHM (cm ⁻¹)	Lorentzian (%) ^a
WT	1729.0	20.0	0.0	1667.0	14.5	0.0
	1681.2	6.9	0.0	1640.2	7.4	0.0
	1666.1	7.9	18.8	1631.5	7.9	0.0
A237Y	1735.2	12.6	14.3	1690.5	13.3	0.5
	1697.9	9.8	27.8	1651.9	9.9	0.0
	1685.4	9.8	0.0	1639.3	12.2	0.0
A237Y ^c	1744.1	12.3	0.0	1697.4	6.1	22.0
	1732.3	14.1	0.0	1688.2	7.8	0.0
A237E	1736.6	7.0	30.0	1691.4	5.6	0.0
	1698.1	11.0	0.0	1655.7	8.8	30.0
	1684.7	10.6	13.3	1640.8	9.9	0.0
A237R	1732.7	13.0	0.1	1683.1	16.3	0.0
	1698.0	13.1	0.0	1648.2	13.0	0.0
	1684.7	12.7	27.8	1634.8	12.6	0.0
A237W	1735.9	11.2	18.6	1691.7	12.8	58.6
	1697.2	9.0	0.0	1653.4	6.5	0.0
	1685.9	12.6	8.2	1643.1	14.2	0.0

^a Gaussian-Lorentzian sum

Table S17. Peak fitting of the difference FTIR spectra of TEM–AVB

	¹² C			¹³ C		
	Position (cm ⁻¹)	FWHM (cm ⁻¹)	Lorentzian (%) ^a	Position (cm ⁻¹)	FWHM (cm ⁻¹)	Lorentzian (%) ^a
WT	1683.9	15.0	6.6	1641.9	12.0	0.0
	1672.4	12.8	0.0	1627.8	10.3	0.0
	1661.6	8.8	18.0	1615.6	7.2	0.0
	1651.6	8.7	17.1	1609.4	10.8	1.3
	1641.0	11.3	22.0	1599.0	13.6	2.2
A237Y	1684.3	15.0	0.0	1640.2	12.1	2.7
	1673.6	14.0	0.5	1621.6	16.7	0.0
	1661.3	10.2	23.2	1611.5	10.1	4.2
	1650.4	7.6	43.6	1603.9	9.5	23.6
	1637.6	15.0	85.6	1595.6	18.7	100.0
A237Y ^c	1687.4	14.3	25.5	1648.3	13.9	0.0
A237E	1684.2	15.0	0.4	1641.1	12.0	0.0
	1673.3	12.3	0.7	1629.6	10.1	0.0
	1661.4	11.6	0.0	1616.3	9.3	0.0
	1650.5	7.3	0.0	1608.3	9.1	7.9
	1642.4	13.5	82.1	1600.4	15.9	98.3
A237R	1684.2	14.5	69.0	1641.4	11.8	49.4
	1674.4	10.5	0.8	1630.8	9.1	0.0
	1662.0	10.6	23.6	1615.5	8.6	6.8
	1650.6	8.8	45.8	1607.4	10.8	65.8
	1640.8	13.1	91.0	1595.0	16.0	100.0
A237W	1684.2	12.6	95.9	1642.1	10.6	76.4
	1674.8	11.9	13.8	1624.9	12.7	19.8
	1662.1	10.7	55.9	1612.9	11.0	75.9
	1650.5	7.2	70.1	1607.9	8.5	50.2
	1640.8	13.3	81.4	1598.6	12.8	83.8

^a Gaussian-Lorentzian sum

Table S18. The largest field experienced by AVB in TEM

	F (TEM•AVB) (MV/cm) ^a	F (TEM–AVB) (MV/cm) ^a
WT	-150 ± 4	-97 ± 4
A237Y	-124 ± 3	-102 ± 4
A237Y ^c	-63 ± 2	-35 ± 2
A237E	-125 ± 3	-95 ± 4
A237R	-125 ± 3	-98 ± 4
A237W	-124 ± 3	-98 ± 4

^a The error of the field was calculated based on the error of probe calibration (see the captions of Figures S12 and S13).

Table S19. Peak fitting of the difference FTIR spectra of TEM•PenG

	¹² C			¹³ C		
	Position (cm ⁻¹)	FWHM (cm ⁻¹)	Lorentzian n (%) ^a	Position (cm ⁻¹)	FWHM (cm ⁻¹)	Lorentzian (%) ^a
WT	1746.4	13.4	4.0	1701.9	9.7	3.5
	1732.0	12.7	0.0	1689.3	13.6	0.0
	1668.8	12.8	100.0	1631.5	6.4	100.0
	1663.3	6.3	0.0	1624.3	6.2	0.0
A237Y	1772.3	16.1	0.0	1725.3	13.5	40.0
	1693.2	4.9	0.0	1651.4	5.4	0.0
	1683.9	12.7	0.0	1639.6	6.3	0.0
	1669.5	6.3	43.3	1630.4	8.0	3.3
A237Y ^c	1770.3	20.0	39.9	1728.1	24.0	0.0
	1689.3	9.1	0.0	1648.8	6.7	5.9
A237E	1768.7	20.0	12.1	1727.5	21.1	0.0
	1692.1	7.0	0.0	1660.0	11.4	0.0
	1685.5	5.8	0.0	1650.4	5.7	0.0
	1672.3	6.0	0.0	1627.9	5.4	0.0
	1664.9	7.9	13.4	1623.4	6.9	0.0
A237R	1770.5	20.0	30.7	1726.9	26.5	0.0
	1672.1	7.8	0.0	1630.3	5.6	0.0
	1664.6	5.9	0.7	1624.8	9.2	0.0
A237W	1693.1	5.2	0.0	1650.4	4.6	0.0
	1686.7	8.9	0.0	1654.7	9.1	0.0
	1665.0	6.2	0.0	1624.8	8.5	0.0

^a Gaussian-Lorentzian sum

Table S20. The largest field experienced by PenG in TEM•PenG

	F (MV/cm) ^a
WT	-171 ± 4
A237Y	-163 ± 4
A237Y ^e	-138 ± 4
A237E	-169 ± 4
A237R	-169 ± 4
A237W	-169 ± 4

^a The error of the field was calculated based on the error of probe calibration. The calibration was performed in our previous work using penam as a model compound¹⁴, providing $|\Delta\mu| = 0.78 \pm 0.02 \text{ cm}^{-1}/(\text{MV}/\text{cm})$ and the frequency in vacuum as $1796.8 \pm 0.6 \text{ cm}^{-1}$.

Table S21. Free energy barrier for PenG hydrolysis by TEM-1

	$\Delta G_{\text{cat}}^{\ddagger}$ (kcal/mol) ^{a,b}	$\Delta G_{\text{ac}}^{\ddagger}$ (kcal/mol) ^{a,b}	ΔG_3^{\ddagger} (kcal/mol) ^{a,b}
WT	12.92 [12.91, 12.94]	12.32 [12.30, 12.34]	12.66 [12.65, 12.68]
A237Y	13.40 [13.39, 13.40]	12.65 [12.63, 12.67]	13.20 [13.19, 13.21]
A237Y ^c	16.43 [16.43, 16.44]	14.70 [14.63, 14.83]	16.40 [16.39, 16.41]
A237E	13.17 [13.16, 13.18]	12.22 [12.20, 12.28]	13.03 [13.02, 13.04]
A237R	12.84 [12.82, 12.86]	12.56 [12.54, 12.59]	12.26 [12.23, 12.29]
A237W	13.91 [13.90, 13.91]	13.07 [13.06, 13.08]	13.75 [13.74, 13.75]

^a $\Delta G^{\ddagger} = -RT \ln[k/(k_{\text{B}}T/h)]$; R = gas constant; T = 296 K; k is the measured rate constant; k_{B} = Boltzmann's constant; \hbar = Planck's constant.

^b The uncertainties of $\Delta G_{\text{cat}}^{\ddagger}$, $\Delta G_{\text{ac}}^{\ddagger}$, and ΔG_3^{\ddagger} were calculated based on the standard error and uncertainty of k_{cat} , k_{ac} , and k_3 in Table S1, respectively.

Table S22. Free energy barrier for AVB inhibition of TEM-1

	$\Delta G_{\text{cbm}}^{\ddagger}$ (kcal/mol) ^{a,b}	$\Delta G_{\text{rec}}^{\ddagger}$ (kcal/mol) ^{a,b}
WT	15.48 [15.47, 15.48]	22.25 [22.18, 22.33]
A237Y	16.25 [16.24, 16.26]	21.07 [20.98, 21.19]
A237Y ^c	21.04 [21.01, 21.07]	26.08 [26.07, 26.10]
A237E	16.42 [16.39, 16.45]	22.82 [22.73, 22.93]
A237R	16.56 [16.56, 16.57]	21.67 [21.59, 21.76]
A237W	16.62 [16.61, 16.63]	21.62 [21.52, 21.75]

^a $\Delta G^{\ddagger} = -RT \ln[k/(k_{\text{B}}T/h)]$; R = gas constant; T = 296 K; k is the measured rate constant; k_{B} = Boltzmann's constant; \hbar = Planck's constant.

^b The uncertainties of $\Delta G_{\text{cbm}}^{\ddagger}$ and $\Delta G_{\text{rec}}^{\ddagger}$ were calculated based on the standard error of k_{cbm} and k_{rec} in Table S2, respectively.

Script 1. Data processing of difference IR spectra

```
%-----Description-----
%
% This script is used to fit 12C-13C difference FTIR spectra into multiple
% 12C and 13C peaks to account for multiple probe conformations.
% Users can specify the wavenumber window for fitting and the number of 12C-
% 13C peak pairs to fit with.
% Author Zhe Ji

%-----Input-----
%
% A 12C-13C spectra that has been baselined: The first column for wavenumber,
% the second column for absorbance.
% The wavenumber window that the spectrum needs to be cut into.
% The number of 12C-13C peak pairs to fit the data into.
% User can suggest the peak positions to start the fitting from.

%-----Output-----
%
% result.txt containing the fitting parameters: each row for a 12C-13C pair.
% 1st column: 12C frequency (cm-1)
% 2nd column: 12C FWHM (cm-1)
% 3rd column: 12C intensity (mOD)
% 4th column: 12C Lorentzian percentage
% 5th column: 13C frequency (cm-1)
% 6th column: 13C FWHM (cm-1)
% 7th column: 13C intensity (mOD)
% 8th column: 13C Lorentzian percentage
% 9th column: frequency shift from 12C to 13C
% 10th column: FWHM ratio from 12C to 13C
% 11th column: Intensity ratio from 12C to 13C
% 12th column: change in Lorentzian percentage from 12C to 13C
%
% Fit.txt containing the absorbance-wavenumber curve for each peak component
% of fitting.
% 1st column is wavenumber, followed by n columns of 12C and n columns of 13C
% absorbance, n=the number of 12C-13C pairs.
% These are further followed by the sum of the fitting peaks, the
% experimental difference spectrum, and the fitting residue.

%-----Main-----
clear
clc
scaf=10000;%A scaling factor that adjust the spectra intensity for better
data fitting.

%Load a 12C-13C difference spectrum
[fname,pname]=uigetfile('*.','Load IR Spectra','MultiSelect','on');
cd(pname);
Data=readtable(fname,'Delimiter',' ','Format','%f %f');
w=Data(:,1);%Wavenumber, cm-1
a=Data(:,2)*1000;%Absorbance, mOD
plot(w,a)
```

```

%Input wavenumber window. The data outside of the window will be cut and not
used for fitting
%also input the number of conformations. For instance, "5" means to fit 5 12C
positive peaks and 5 13C negative peaks
dlgtitle='Input';
dim=1;
prompt1={'Wavenumber upper limit', 'Wavenumber lower limit', 'Number of C=O
conformations'};
def1={'2000', '1500', '3', };
answer1=inputdlg(prompt1,dlgtitle,dim,def1);
drawnow

%suggest the initial value of the peak positions. If there are 5
conformations, the user can suggest 5 12C-peak positions and 5 13C-peak
positions.
pair=str2num(char(answer1(3)));% the number of positive-negative pairs
(conformations)
dlgtitle='Input Wavenumber';
dim=1;
prompt2=cell(1,pair*2);
prompt2(1,1:pair)={'12C Wavenumber'};
prompt2(1,pair+1:pair*2)={'13C Wavenumber'};
def2=cell(1,pair*2)
def2(1,1:pair*2)={'0'};% the default position is "0", if no suggestion is
given.
answer2=inputdlg(prompt2,dlgtitle,dim,def2);
drawnow

%-----Data cutting and peak position guess-----
-----
if str2num(char(answer1(1)))>=w(1)
    wul=w(1);
    ul_index=1;%the index of the upper limit of the wavenumber
else
    wul=str2num(char(answer1(1)));
    for j=1:length(w)
        if w(j)>wul
            ul_index=j;
        end
    end
    ul_index=ul_index+1;
end
if str2num(char(answer1(2)))<=w(end)
    wll=w(end);
    ll_index=length(w);%the index of the lower limit of the wavenumber
else
    wll=str2num(char(answer1(2)));
    for j=length(w):-1:1
        if w(j)<wll
            ll_index=j;
        end
    end
    ll_index=ll_index-1;
end
end

```

```

guess=zeros(pair*2,1);
guessinput=zeros(pair*2,1);
for i=1:pair*2
    guessinput(i)=str2num(char(answer2(i)));%user-suggested peak positions
end

if ismember(0,guessinput(1:pair))% if there is no suggestion for 12C
positions
    gap=(wul-wll)/2/(pair+1);
    for i=1:pair
        guess(i)= wul-gap*i;% the initial 12C positions are set to evenly
span the upper half of the wavenumber window
    end
    guess(pair+1:pair*2)=guess(1:pair)-47;
else % if there is suggestion for 12C positions
    guess(1:pair)=guessinput(1:pair);
    if ismember(0,guessinput(pair+1:pair*2)) %if there is no suggestion for
the 13C positions
        guess(pair+1:pair*2)=guess(1:pair)-47;
    else
        guess(pair+1:pair*2)=guessinput(pair+1:pair*2);%if there is
suggestion for the 13C positions
    end
end
end
w=w(ul_index:ll_index);%cut the data according to the user-defined wavenumber
window
a=a(ul_index:ll_index,:);

%-----Peak Fitting-----
-----
scaling=1/max(a)*scaf;
a=a*scaling;%scale absorbance such that the built-in fitting tolerance is
suitable
a=[w,a];

fun=@ModFun;
x0=zeros(pair*8,1);%the initial fitting parameters. There are 8 parameters
for each 12C-13C pair.
for i=0:(pair-1)
    x0(i*8+1)=guess(i+1);%peak position by guess
    x0(i*8+2)=10;%FWHM
    x0(i*8+3)=0.5*scaling;%Intensity
    x0(i*8+4)=0.2;%percentage of Lorentzian
    x0(i*8+5)=guess(i+1+pair)-guess(i+1);%frequency shift from 12C to 13C
    x0(i*8+6)=1;%widening ratio from 12C to 13C
    x0(i*8+7)=1;%Amplification ratio from 12C to 13C
    x0(i*8+8)=0;%change in Lorentzian percentage
end

lb=zeros(pair*8,1);%the lower bound for the parameters
for i=0:(pair-1)
    lb(i*8+1)=min(w);
    lb(i*8+2)=2;%the narrowest FWHM
    lb(i*8+3)=0.1*scaling;%the lowest intensity
    lb(i*8+4)=0;%Lorentzian percentage from 0 to 1

```

```

    lb(i*8+5)=-62;%the largest frequency shift allowed from 12C to 13C
    lb(i*8+6)=0.8;% the narrowing limit of FWHM from 12C to 13C
    lb(i*8+7)=-1.5;% the upper limit of intensity enhancement from 12C to
13C. Take negative sign for 13C peaks
    lb(i*8+8)=-0.3;%the largest decrease of Lorentzian percentage allowed
from 12C to 13C
end

ub=zeros(pair*8,1);%the upper bound for the fitting parameters
for i=0:(pair-1)
    ub(i*8+1)=max(w);
    ub(i*8+2)=20;%the widest FWHM
    ub(i*8+3)=20*scaling;%the highest intensity
    ub(i*8+4)=1;%Lorentzian percentage from 0 to 1
    ub(i*8+5)=-32;%the smallest frequency shift allowed from 12C to 13C
    ub(i*8+6)=1.25;% the broadening limit of FWHM from 12C to 13C
    ub(i*8+7)=-0.67;% the lower limit of intensity enhancement from 12C to
13C. Take negative sign for 13C peaks
    ub(i*8+8)=0.3;%the largest increase of Lorentzian percentage allowed from
12C to 13C
end

TargetFun=zeros(length(a(:,1)),1);
options = optimset('MaxFunEvals',100000);
options = optimset(options, 'MaxIter',100000, 'TolX',1E-18);
[x,resnorm,residual] = lsqcurvefit(fun,x0,a,TargetFun,lb,ub,options);%the
fitting
a(:,1)=[];
a=a/scaling;%recover the original Absorbance, unit: mOD
residual=-residual/scaling;
result=zeros(pair,12);%the matrix that stores the fitting parameters
for i=0:(pair-1)%each row for one conformation
    result(i+1,1)=x(i*8+1);%Peak position for 12C
    result(i+1,2)=x(i*8+2);%FWHM for 12C
    result(i+1,3)=x(i*8+3)/scaling;%Intensity for 12C
    result(i+1,4)=x(i*8+4)*100;%Lorentzian percentage for 12C
    result(i+1,5)=x(i*8+1)+x(i*8+5);%Peak position for 13C
    result(i+1,6)=x(i*8+2)*x(i*8+6);%FWHM for 13C
    result(i+1,7)=x(i*8+3)*x(i*8+7)/scaling;%Intensity for 13C
    result(i+1,8)=(x(i*8+4)+x(i*8+8))*100;%Lorentzian percentage for 13C
    if result(i+1,8)<0 %the Lorentzian percentage must be [0,100]
        result(i+1,8)=0;
    elseif result(i+1,8)>100
        result(i+1,8)=100;
    end
end
end
result(:,9)=result(:,5)-result(:,1);%frequency shift from 12C to 13C
result(:,10)=result(:,6)./result(:,2);%FWHM ratio
result(:,11)=result(:,7)./result(:,3);%Intensity ratio
result(:,12)=result(:,8)-result(:,4);%change in Lorentzian percentage
result=sortrows(result,1,'descend');

PeakFit=zeros(length(w),pair*2+1);%The matrix that stores the absorbance-
wavenumber curve for each peak component of fitting.
PeakFit(:,1)=w;
for i = 1:pair

```

```

E=result(i,1);
F=result(i,2);
h=result(i,3);
m=result(i,4)/100;
E2=result(i,5);
F2=result(i,6);
h2=result(i,7);
m2=result(i,8)/100;
for j=1:length(w)
    PeakFit(j,(i-1)*2+2)=PeakFit(j,(i-1)*2+2)+h*(1-m)*exp(-4*log(2)*(w(j)-
E)^2/F^2)+h*m/(1+4*(w(j)-E)^2/F^2);
end
for j=1:length(w)
    PeakFit(j,(i-1)*2+3)=PeakFit(j,(i-1)*2+3)+h2*(1-m2)*exp(-4*log(2)*(w(j)-
E2)^2/F2^2)+h2*m2/(1+4*(w(j)-E2)^2/F2^2);
end
end

PeakFitTotal=zeros(length(w),1);%The sum of the absorbance-wavenumber curves
for all peak component of fitting.
for i =1:pair*2
    PeakFitTotal=PeakFitTotal+PeakFit(:,i+1);
end

figure(1)
plot(w,PeakFit(:,2:(pair*2+1)),w,a,'--')
xlabel('Wavenumber (cm-1)')
ylabel('Difference Absorbance (mOD)')

figure(2)
plot(w,a,'--',w,PeakFitTotal,w,residual)
xlabel('Wavenumber (cm-1)')
ylabel('Difference Absorbance (mOD)')

Fit=[PeakFit,PeakFitTotal,a,residual];

mkdir new
cd new/
writematrix(Fit);
writematrix(result);
cd ..

function Res=ModFun(x,a)
pairnum=length(x)/8;%every positive-negative pair has 8 parameters
Abs=zeros(length(a(:,1)),1);
for i = 0:(pairnum-1)
    E=x(i*8+1);%peak position
    F=x(i*8+2);%FWHM
    h=x(i*8+3);%Intensity
    m=x(i*8+4);%the percentage of Lorentzian
    shift=x(i*8+5);%the frequency shift from 12C to 13C
    widen=x(i*8+6);%the FWHM widening ratio from 12C to 13C
    Amplif=x(i*8+7);%the Intensity amplification ratio from 12C to 13C
    reshape=x(i*8+8);%the change in Lorentzian percentage from 12C to 13C

```

```

E2=E+shift;
F2=F*widen;
h2=h*Amplif;
if reshape<0      %the Lorentzian percentage of 13C should be in the range
of 0-1
    m2=max(m+reshape,0);
else
    m2=min(m+reshape,1);
end
for j=1:length(a(:,1))
    Abs(j)=Abs(j)+h*(1-m)*exp(-4*log(2)*(a(j,1)-E)^2/F^2)+h*m/(1+4*(a(j,1)-
E)^2/F^2);%the Gaussian-Lorentzian sum of 12C peak
    Abs(j)=Abs(j)+h2*(1-m2)*exp(-4*log(2)*(a(j,1)-
E2)^2/F2^2)+h2*m2/(1+4*(a(j,1)-E2)^2/F2^2);%the Gaussian-Lorentzian sum of
13C peak
end
end
Res=Abs-a(:,2);
end

```

Script 2. Data processing of raw isotope-edited IR spectra

```
%-----Description-----
%
% This script is used to cut, baseline, and fit 12C and 13C FTIR spectra.
% Loaded into the script are raw 12C and 13C spectra. They can be repeats of
multiple experiments.
% The 12C spectra will be subtracted by the corresponding 13C spectra.
% A baseline will be fitted for each difference spectrum.
% A single set of 12C-13C peak pairs will be fitted for all the difference
spectra.
% Author Zhe Ji

%-----Input-----
%
% n 12C spectra and n 13C spectra (n=number of experimental repeats): The
first column for wavenumber, the second column for absorbance.
% The wavenumber window that the spectrum needs to be cut into.
% The number of 12C-13C peak pairs to fit the data into.
% For baselines, whether add a linear function in addition to the two default
Gaussian functions.

%-----Output-----
%
% Spec_13Scaled.txt containing a column of wavenumber followed by n columns
of 12C absorbance and n columns of 13C absorbance. The 13C spectra has been
scaled.
%
% Spec_DiffBase.txt containing a column of wavenumber followed by n columns
of difference absorbance, n columns of baseline absorbance, and n columns of
baselined difference absorbance.
%
% result.txt containing the fitting parameters: each row for a 12C-13C pair.
% 1st column: 12C frequency (cm-1)
% 2nd column: 12C FWHM (cm-1)
% 3rd column: 12C intensity (mOD)
% 4th column: 12C Lorentzian percentage
% 5th column: 13C frequency (cm-1)
% 6th column: 13C FWHM (cm-1)
% 7th column: 13C intensity (mOD)
% 8th column: 13C Lorentzian percentage
% 9th column: frequency shift from 12C to 13C
% 10th column: FWHM ratio from 12C to 13C
% 11th column: Intensity ratio from 12C to 13C
% 12th column: change in Lorentzian percentage from 12C to 13C
%
% Fit.txt containing the absorbance-wavenumber curve for each peak component
of fitting.
% 1st column is wavenumber, followed by n columns of 12C and n columns of 13C
absorbance,
% a column of the absorbance sum of the fitting peaks, a column of the
% average absorbance of the baselined difference spectra,
% a column of averaged fitting residue, and n columns of fitting residue.
%
% BaseResult.txt containing the fitting parameters: each row for a baseline.
% 1st column: 1st Gaussian frequency (cm-1)
```

```

% 2nd column: 1st Gaussian FWHM (cm-1)
% 3rd column: 1st Gaussian intensity (mOD)
% 4th column: 2nd Gaussian frequency (cm-1)
% 5th column: 2nd Gaussian FWHM (cm-1)
% 6th column: 2nd Gaussian intensity (mOD)
% 7th column: slope of the linear
% 8th column: intercept of the linear

%-----Main-----
clear
clc
scaling=1/100;%A scaling factor that adjust the spectra intensity for better
data fitting.

%Load a 12C and 13C spectra. For 9 experimental repeats, the input will be 9
12C spectra followed by 9 13C spectra.
%The spectra is in the format of wavenumber vs absorbance.
[fname,pname]=uigetfile('*.','Load IR Spectra','MultiSelect','on');
cd(pname);
SpecNum=length(fname)/2;
Data=readtable(fname{1},'Delimiter',' ','Format','%f %f');
w=Data{: ,1};%Wavenumber, cm-1
a=Data{: ,2}*1000;%Absorbance, mOD
if SpecNum>0.5
    for i = 2:SpecNum*2
        Data=readtable(fname{i},'Delimiter',' ','Format','%f %f');
        atemp=Data{: ,2}*1000;%Absorbance, mOD
        a=[a,atemp];
    end
end

%Input wavenumber window. The data outside of the window will be cut and not
used for fitting
%Input the number of conformations. For instance, "5" means to fit 5 12C
positive peaks and 5 13C negative peaks
%Input the baseline parameter: whether add a linear component? "0" means no;
"1" means yes.
dlgtitle='Input';
dim=1;
prompt1={'Wavenumber upper limit','Wavenumber lower limit','Number of C=O
conformations','Baseline add linear?'};
def1={'1704.5','1580.5','5','0'};
answer1=inputdlg(prompt1,dlgtitle,dim,def1);
drawnow
bslLinear=str2num(char(answer1(4)));
pair=str2num(char(answer1(3)));% the number of positive-negative pairs

%-----Data cutting and peak position initialization-----
if str2num(char(answer1(1)))>=w(1)
    wul=w(1);%the index of the upper limit of the wavenumber
    ul_index=1;
else
    wul=str2num(char(answer1(1)));
    for j=1:length(w)

```

```

        if w(j)>wul
            ul_index=j;
        end
    end
    ul_index=ul_index+1;
end
if str2num(char(answer1(2)))<=w(end)
    wll=w(end);%the index of the lower limit of the wavenumber
    ll_index=length(w);
else
    wll=str2num(char(answer1(2)));
    for j=length(w):-1:1
        if w(j)<wll
            ll_index=j;
        end
    end
    ll_index=ll_index-1;
end
guess=zeros(pair,1);
gap=(wul-wll)/2/(pair+1);
for i=1:pair
    guess(i)= wul-gap*i;% the initial 12C positions are set to evenly span
the upper half of the wavenumber window
end

w=w(ul_index:ll_index);
a=a(ul_index:ll_index,:);

%-----12C subtraction by 13C-----
-----
for i=1:SpecNum
    %A scaling factor is used to adjust the intensity such that the area
under the 13C curve is the same as that of the 12C curve
    a(:,i+SpecNum)=sum(a(:,i))/sum(a(:,i+SpecNum))*a(:,i+SpecNum);
end
Spec_13Scaled=a;
for i=1:SpecNum
    a(:,i+SpecNum)=a(:,i)-a(:,i+SpecNum);
end
a(:,1:SpecNum)=[];
Spec_Subtracted=a;

%-----Peak Fitting-----
-----
a=a*scaling;%scale absorbance such that the built-in fitting tolerance is
suitable
a=[w,a];
fun=@ModFun;
x0=zeros(pair*8+SpecNum*8,1);%the initial fitting parameters. There are 8
parameters for each 12C-13C pair plus 8 parameters for each baseline.
for i=0:(pair-1)
    x0(i*8+1)=guess(i+1);%peak position
    x0(i*8+2)=10;%FWHM
    x0(i*8+3)=5*scaling;%Intensity
    x0(i*8+4)=0.5;%percentage of Lorentzian
    x0(i*8+5)=-47;%frequency shift from 12C to 13C

```

```

    x0(i*8+6)=1;%widening ratio from 12C to 13C
    x0(i*8+7)=1;%Amplification ratio from 12C to 13C
    x0(i*8+8)=0;%change in Lorentzian percentage
end

%also the fitting parameters for the baselines. There is one baseline for
each difference spectrum.
%The baseline contains two gaussian functions and a linear function
(optional)
for i=0:SpecNum-1
    x0(8*pair+8*i+1)=1620;%peak position of the 1st gaussian
    x0(8*pair+8*i+2)=40;%FWHM of the 1st gaussian
    x0(8*pair+8*i+3)=15*scaling;%The peak intensity of the 1st gaussian
    x0(8*pair+8*i+4)=1660;%peak position of the 2nd gaussian
    x0(8*pair+8*i+5)=40;%FWHM of the 2nd gaussian
    x0(8*pair+8*i+6)=-5*scaling;%The peak intensity of the 2nd gaussian
end

lb=zeros(pair*8+8,1);%the lower bound for the fitting parameters
for i=0:(pair-1)
    lb(i*8+1)=min(w)+20;
    lb(i*8+2)=2;%the narrowest FWHM
    lb(i*8+3)=1*scaling;%the lowest intensity
    lb(i*8+4)=0;%Lorentzian percentage from 0 to 1
    lb(i*8+5)=-52;%the largest frequency shift allowed from 12C to 13C
    lb(i*8+6)=0.80;% the narrowing limit of FWHM from 12C to 13C
    lb(i*8+7)=-1.25;% the upper limit of intensity enhancement from 12C to
13C. Take negative sign for 13C peaks
    lb(i*8+8)=-0.2;%the largest decrease of Lorentzian percentage allowed
from 12C to 13C
end

for i=0:SpecNum-1
    lb(8*pair+8*i+1)=min(w)+20;%1st Gaussian
    lb(8*pair+8*i+2)=20;
    lb(8*pair+8*i+3)=-30*scaling;
    lb(8*pair+8*i+4)=min(w)+20;%2nd Gaussian
    lb(8*pair+8*i+5)=15;
    lb(8*pair+8*i+6)=-30*scaling;
    lb(8*pair+8*i+7)=-0.1*scaling*bslLinear;%optional linear slope
    lb(8*pair+8*i+8)=-10*scaling*bslLinear;%optional linear intercept
end

ub=zeros(pair*8+8,1);%the upper bound for the parameters
for i=0:(pair-1)
    ub(i*8+1)=max(w)-20;
    ub(i*8+2)=15;%the widest FWHM
    ub(i*8+3)=30*scaling;%the highest intensity
    ub(i*8+4)=1;%Lorentzian percentage from 0 to 1
    ub(i*8+5)=-42;%the smallest frequency shift from 12C to 13C
    ub(i*8+6)=1.25;% the broadening limit of FWHM from 12C to 13C
    ub(i*8+7)=-0.80;% the lower limit of intensity enhancement from 12C to
13C. Take negative sign for 13C peaks
    ub(i*8+8)=0.2;%the largest increase of Lorentzian percentage allowed from
12C to 13C
end

```

```

for i=0:SpecNum-1
    ub(8*pair+8*i+1)=max(w)-20;%1st Gaussian
    ub(8*pair+8*i+2)=200;
    ub(8*pair+8*i+3)=30*scaling;
    ub(8*pair+8*i+4)=max(w)-20;%2nd Gaussian
    ub(8*pair+8*i+5)=200;
    ub(8*pair+8*i+6)=30*scaling;
    ub(8*pair+8*i+7)=0.1*scaling*bslLinear;%optional linear slope
    ub(8*pair+8*i+8)=10*scaling*bslLinear;%optional linear intercept
end

TargetFun=zeros(length(a(:,1)),SpecNum);
options = optimset('MaxFunEvals',100000);
options = optimset(options,'MaxIter',100000,'TolX',1E-18);
[x,resnorm,residual] = lsqcurvefit(fun,x0,a,TargetFun,lb,ub,options);%the
fitting
a(:,1)=[];
a=a/scaling;%recover the original Absorbance, unit: mOD
residual=-residual/scaling;
result=zeros(pair,12);%the matrix that stores the fitting parameters for the
12C and 13C peaks
for i=0:(pair-1)%each row for one pair of 12C-13C peaks
    result(i+1,1)=x(i*8+1);%Peak position for 12C
    result(i+1,2)=x(i*8+2);%FWHM for 12C
    result(i+1,3)=x(i*8+3)/scaling;%Intensity for 12C
    result(i+1,4)=x(i*8+4)*100;%Lorentzian percentage for 12C
    result(i+1,5)=x(i*8+1)+x(i*8+5);%Peak position for 13C
    result(i+1,6)=x(i*8+2)*x(i*8+6);%FWHM for 13C
    result(i+1,7)=x(i*8+3)*x(i*8+7)/scaling;%Intensity for 13C
    result(i+1,8)=(x(i*8+4)+x(i*8+8))*100;%Lorentzian percentage for 13C
    if result(i+1,8)<0
        result(i+1,8)=0;
    elseif result(i+1,8)>100
        result(i+1,8)=100;
    end
end
end
result(:,9)=result(:,5)-result(:,1);%frequency shift from 12C to 13C
result(:,10)=result(:,6)./result(:,2);%FWHM ratio
result(:,11)=result(:,7)./result(:,3);%Intensity ratio
result(:,12)=result(:,8)-result(:,4);%change in Lorentzian percentage
result=sortrows(result,1,'descend');

PeakFit=zeros(length(w),pair*2+1);%The matrix that stores the absorbance-
wavenumber curve for each peak component of fitting.
PeakFit(:,1)=w;
for i = 1:pair
    E=result(i,1);
    F=result(i,2);
    h=result(i,3);
    m=result(i,4)/100;
    E2=result(i,5);
    F2=result(i,6);
    h2=result(i,7);
    m2=result(i,8)/100;
    for j=1:length(w)

```

```

    PeakFit(j, (i-1)*2+2)=PeakFit(j, (i-1)*2+2)+h*(1-m)*exp(-4*log(2)*(w(j)-
E)^2/F^2)+h*m/(1+4*(w(j)-E)^2/F^2);
    end
    for j=1:length(w)
        PeakFit(j, (i-1)*2+3)=PeakFit(j, (i-1)*2+3)+h2*(1-m2)*exp(-4*log(2)*(w(j)-
E2)^2/F2^2)+h2*m2/(1+4*(w(j)-E2)^2/F2^2);
    end
end

PeakFitTotal=zeros(length(w),1);%The sum of the absorbance-wavenumber curves
for all peak component of fitting.
for i =1:pair*2
    PeakFitTotal=PeakFitTotal+PeakFit(:,i+1);
end

BaseResult=zeros(SpecNum,8);%the matrix that stores the fitting parameters
for the baselines
for i=0:SpecNum-1
    for j=1:8
        if ismember(j,[3 6 7 8])
            BaseResult(i+1,j)=x(8*pair+i*8+j)/scaling;
        else
            BaseResult(i+1,j)=x(8*pair+i*8+j);
        end
    end
end

Baseline=zeros(length(w),SpecNum);%The matrix that stores the absorbance-
wavenumber curve for each baseline
for i=1:SpecNum
    E=BaseResult(i,1);%peak position for the 1st Gaussian
    F=BaseResult(i,2);%FWHM
    h=BaseResult(i,3);%Intensity
    E2=BaseResult(i,4);%peak position for the 2nd Gaussian
    F2=BaseResult(i,5);%FWHM
    h2=BaseResult(i,6);%Intensity
    slope=BaseResult(i,7);%slope for the linear
    intercept=BaseResult(i,8);%intercept for the linear
    for j=1:length(w)
        Baseline(j,i)=h*exp(-4*log(2)*(w(j)-E)^2/F^2)+h2*exp(-4*log(2)*(w(j)-
E2)^2/F2^2);
    end
    Baseline(:,i)=Baseline(:,i)+slope*w+intercept;
end
Spec_Baselined=Spec_Subtracted-Baseline;
Spec_Averaged=sum(Spec_Baselined,2)/SpecNum;
Residual_Averaged=sum(residual,2)/SpecNum;

figure(1)
plot(w,Baseline,w,Spec_Subtracted,'--')
xlabel('Wavenumber (cm-1)')
ylabel('Difference Absorbance (mOD)')

figure(2)
plot(w,Spec_Baselined,'--',w,Spec_Averaged)
xlabel('Wavenumber (cm-1)')

```

```

ylabel('Difference Absorbance (mOD)')

figure(3)
plot(w,PeakFit(:,2:(pair*2+1)),w,Spec_Averaged,'--')
xlabel('Wavenumber (cm-1)')
ylabel('Difference Absorbance (mOD)')

figure(4)
plot(w,Spec_Averaged,'--',w,PeakFitTotal,w,residual)
xlabel('Wavenumber (cm-1)')
ylabel('Difference Absorbance (mOD)')

Spec_13Scaled=[w,Spec_13Scaled];
Spec_DiffBase=[w,Spec_Subtracted,Baseline,Spec_Baselined];
Fit=[PeakFit,PeakFitTotal,Spec_Averaged,Residual_Averaged,residual];

mkdir new
cd new/
writematrix(Spec_13Scaled);
writematrix(Spec_DiffBase);
writematrix(Fit);
writematrix(result);
writematrix(BaseResult);
cd ..

function Res=ModFun(x,a)
specnum=length(a(1,:))-1;
pairnum=(length(x)-8*specnum)/8;%every positive-negative pair has 8
parameters
Abs=zeros(length(a(:,1)),1);
for i = 0:(pairnum-1)
    E=x(i*8+1);%peak position
    F=x(i*8+2);%FWHM
    h=x(i*8+3);%Intensity
    m=x(i*8+4);%the percentage of Lorentzian
    shift=x(i*8+5);%the frequency shift from 12C to 13C
    widen=x(i*8+6);%the FWHM widening ratio from 12C to 13C
    Amplif=x(i*8+7);%the Intensity amplification ratio from 12C to 13C
    reshape=x(i*8+8);%the change in Lorentzian percentage from 12C to 13C
    E2=E+shift;
    F2=F*widen;
    h2=h*Amplif;
    if reshape<0 %the Lorentzian percentage of 13C should be in the range
of 0-1
        m2=max(m+reshape,0);
    else
        m2=min(m+reshape,1);
    end
    for j=1:length(a(:,1))
        Abs(j)=Abs(j)+h*(1-m)*exp(-4*log(2)*(a(j,1)-E)^2/F^2)+h*m/(1+4*(a(j,1)-
E)^2/F^2);%the Gaussian-Lorentzian sum of 12C peak
        Abs(j)=Abs(j)+h2*(1-m2)*exp(-4*log(2)*(a(j,1)-
E2)^2/F2^2)+h2*m2/(1+4*(a(j,1)-E2)^2/F2^2);%the Gaussian-Lorentzian sum of
13C peak
    end
end

```

```

end

baseline=zeros(length(a(:,1)),specnum);
for i=0:specnum-1
    E=x(pairnum*8+i*8+1);%peak position
    F=x(pairnum*8+i*8+2);%FWHM
    h=x(pairnum*8+i*8+3);%Intensity
    E2=x(pairnum*8+i*8+4);%peak position
    F2=x(pairnum*8+i*8+5);%FWHM
    h2=x(pairnum*8+i*8+6);%Intensity
    slope=x(pairnum*8+i*8+7);
    intercept=x(pairnum*8+i*8+8);
    for j=1:length(a(:,1))
        baseline(j,i+1)=h*exp(-4*log(2)*(a(j,1)-E)^2/F^2)+h2*exp(-
4*log(2)*(a(j,1)-E2)^2/F2^2);
    end
    baseline(:,i+1)=baseline(:,i+1)+slope*a(:,1)+intercept;
end

baselined=a(:,2:specnum+1)-baseline;
Res=Abs-baselined;
end

```

Script 3. Full-time kinetic data fitting to integrated Michaelis-Menten

```
function
[Km, kcat, dS, StErr, y, residual, KMGuess, kcatGuess]=MMLam_v2(Data, E0input)

%-----Description-----
% This script generates Michaelis-Menten constants by fitting full-time
kinetic data

%-----Version Info-----
% The first script was written by Samuel H. Schneider; See ACS Central
Science, 7, 1996-2008
% The 2nd version was written by Zhe Ji, which directly reads the initial
% substrate concentration and makes guesses for kcat and KM.

%-----Input Data-----
% Data is a 2-column matrix of x-values (1st column; time; sec), and y-values
(2nd column; substrate concentration; uM)
% E0input is enzyme concentration (uM)

%-----Output Data-----
% Km (uM) and kcat (s-1) are the Michaelis-Menten constants
% dS is a fitting parameter that adjust any deviation of the final substrate
concentration from 0; it should be a small value
% StErr is the fitting error of Km, kcat, and dS
% y is the fitted substrate concentration as a function of time
% residual is the fitting residual of substrate concentration as a function
of time
% KMGuess is the initial guess for KM
% kcatGuess is the initial guess for kcat

%-----Main-----
E0=E0input;
t=Data(:,1);
St=Data(:,2);
S0=St(1); %Starting substrate concentration (uM)

function St=Lambert(beta,t)
Km=beta(1);
kcat=beta(2);
dS=beta(3);
S0new=S0-dS;
St=Km*lambertw((exp((S0new-kcat*E0*t)./Km)).*(S0new/Km))+dS;
end

%Guess for dS (uM), KM (uM) and kcat (sec-1)
dSGuess=0;
stepmin=20;%the step for sampling slopes
partnum=20;%the number of slopes to be sampled
partleng=fix(length(t)/(partnum+1));
step=min(stepmin,partleng);
slope=zeros(partnum,1);
for i=1:partnum
    start=(i-1)*partleng+1;
    stop=start+step;
```

```

    LinFit=polyfit(t(start:stop),St(start:stop),1);
    slope(i)=LinFit(1);
end
kcatGuess=-slope(1)/E0;
[MinValue,ClosestIndex]=min(abs(slope-slope(1)/2));
KMGuess=St((ClosestIndex-1)*partleng+11);

%Fitting with the closed form of the integrated Michaelis Menten kinetics
fun=@Lambert;
beta0=[KMGuess, kcatGuess, dSGuess];
options=statset('FunValCheck','off');
[beta,R,J,CovB]=nlinfit(t,St,fun,beta0,options);

S0new=S0-beta(3);
y=beta(1)*lambertw((exp((S0new-
beta(2)*E0*t)./beta(1)).*(S0new/beta(1))));%the fitted results
format long
Km=beta(1);
kcat=beta(2);
dS=beta(3);
residual=R;
plot(t,(St-beta(3)),t,y,t,residual);
StErr=(sqrt(diag(CovB)));
end

```

Script 4. Inhibition kinetic data fitting to eq. 13

```
function [Time,Product,V0,Vs,Kobs,ProductFit,D] =
InhibitionFittingPart1(Data,I)

%-----Description-----
% This script fits the inhibition features (v0,vs, and kobs) from
% experimental data (P) using eq. 13
% Author: Zhe Ji

%-----Input Data-----
% Data is a (n+1)-column matrix. The first column is time (s). The rest
% columns are the concentrations of product for each I. n = the number of
% I. The n experiments are allowed to have different length but the time
% column should cover the longest.
% I is a 1-column matrix containing the concentration of the inhibitor (uM)
% for each experiment

%-----Output Data-----
% Time is a 1-column matrix (s)
% Product is a n-column matrix of product concentration (uM) as a function of
% time and I
% V0 is a 1-column matrix of the initial rate of product formation as a
% function of I
% Vs is a 1-column matrix of the final rate of product formation as a
% function of I
% Kobs is a 1-column matrix of the apparent first order rate constant for
% forming E-AVB as a function of I
% ProductFit is a n-column matrix of fitted product concentration
% D is a 1-column matrix of a displacement parameter that adjusts the absolute
% product concentration

%-----Main-----

n=length(Data(1,:))-1; % n is the number of experiments
Time=Data(:,1);
Product=Data(:,2:n+1);
LinLeng1st=7; % the number of data points used for making the guess of the
initial slope
LinLeng2nd=300; % the number of data points used for making the guess of the
final slope
delay=0.058; % the dead time of the stopped-flow apparatus(s)

function P=ModFun(beta,t)
v0=beta(1);
vs=beta(2);
kobs=beta(3);
d=beta(4); % d is a displacement parameter that adjusts the absolute product
concentration
P=vs*(t+delay)+(v0-vs)*(1-exp(-kobs*(t+delay)))/kobs-(vs*delay+(v0-vs)*(1-
exp(-kobs*delay))/kobs)+d; % eq. 13
end

fun=@ModFun;
V0=zeros(n,1);
```

```

Vs=zeros(n,1);
Kobs=zeros(n,1);
D=zeros(n,1);
Residual=zeros(length(Data(:,1)),n);

for i=1:n
    temp=nonzeros(Product(2:end,i)); %remove the "0" artifacts due to the
different length of data
    ProductNew=[0;temp]; %bring back the first data point "0" that was mis-
removed
    TimeNew=Time(1:length(ProductNew)); %cut the time column
    LinFit=polyfit(TimeNew(1:LinLeng1st),ProductNew(1:LinLeng1st),1); %the
initial slope
    v0Guess=LinFit(1);
    LinFit=polyfit(TimeNew((end-LinLeng2nd):end),ProductNew((end-
LinLeng2nd):end),1); %the final slope
    vsGuess=LinFit(1);
    kGuess=(v0Guess-vsGuess)/LinFit(2); % make guess for kobs
    beta0=[v0Guess, vsGuess, kGuess,0];
    options=statset('FunValCheck','off');
    [beta,R]=nlinfit(TimeNew,ProductNew,fun,beta0,options);
    V0(i)=beta(1);
    Vs(i)=beta(2);
    Kobs(i)=beta(3);
    D(i)=beta(4);
    Residual(1:length(R),i)=R;
end

Product(Product==0)=nan;
Product(1,:)=0;
ProductFit=Product-Residual; % fitted product concentration

figure(1)
plot(Time,Product,'--',Time,ProductFit);
xlabel('Time (sec)')
ylabel('[Product] (uM)')

figure(2)
scatter(I,V0);
xlabel('[Inhibitor] (uM)')
ylabel('v0 (s-1)')

figure(3)
scatter(I,Vs);
xlabel('[Inhibitor] (uM)')
ylabel('vs (s-1)')

figure(4)
scatter(I,Kobs);
xlabel('[Inhibitor] (uM)')
ylabel('kobs')

end

```

Script 5. Inhibition kinetic data fitting to eq. 17 and eq. 23

```
function [Ki,StErrKi,k5,StErrk5,V0disp,IFit,V0Fit,xFit,KobsFit] =
InhibitionFittingPart2(V0,Kobs,I,E,S,kcat,KM)
%-----Description-----
% This script is used following InhibitionFittingPart1. It fits the
inhibition parameters (Ki and k5) from inhibition features (v0 and kobs)
using eq. 17 and eq. 23
% Author: Zhe Ji

%-----Input Data-----
% V0 is a 1-column matrix of the initial rate of product formation as a
function of I
% Kobs is a 1-column matrix of the apparent first order rate constant for
forming E-AVB as a function of I
% I is a 1-column matrix containing the concentration of the inhibitor (uM)
% E is the concentration of the enzyme (uM)
% S is the concentration of the substrate (uM)
% kcat and KM are the Michaelis-Menten constants for the substrate

%-----Output Data-----
% Ki is the binding constant of the inhibitor for the non-covalent binding,
StErrKi is the corresponding fitting error
% k5 is the rate constant for forming E-AVB, , StErrk5 is the corresponding
fitting error
% V0disp is a 1-column matrix of a displacement parameter that adjusts the
absolte initial slope
% IFit is a 1-column matrix of x for the fitted trace of eq. 17
% V0Fit is a 1-column matrix of y for the fitted trace of eq. 17
% xFit is a 1-column matrix of x for data and the fitted trace of eq. 23
% KobsFit is a 1-column matrix of y for the fitted trace eq. 23

%-----Main-----

vmax=kcat*E;

%-----Fit Ki from v0 using eq. 17-----
function output=ModFun(beta,I)
    output=zeros(length(I),1); % output is v0
    V0disp=beta(2); % a displacement parameter that adjusts the absolte
initial slope
    for i=1:length(I)
        output(i)=vmax*S/KM/(1+I(i)/beta(1)+S/KM)+V0disp; % eq. 17
    end
end

fun=@ModFun;
beta0=[100,0]; % make guess for Ki (uM) and the displacement parameter (uM)
options=statset('FunValCheck','off');
[beta,R,J,CovB]=nlinfit(I,V0,fun,beta0,options);
Ki=beta(1);
V0disp=beta(2);
StErrKi=sqrt(diag(CovB));
```

```

IFit= (min(I):(max(I)-min(I))/100:max(I)).'; % x for the fitted trace
V0Fit=zeros(length(IFit),1); % y for the fitted trace
for i=1:length(IFit)
    V0Fit(i)=vmax*S/KM/(1+IFit(i)/Ki+S/KM)+V0disp;
end

figure(1)
plot(IFit,V0Fit)
hold on
scatter(I,V0)
xlabel('[Inhibitor] (uM)')
ylabel('v0 (s-1)')
hold off

%-----Linear Fitting of k5 using eq. 23-----

xFit=I/Ki./(1+S/KM+(I/Ki)); % x for the linear fitting
mdl=fitlm(xFit,Kobs);
k5=mdl.Coefficients.Estimate(2);
StErrk5=mdl.Coefficients.SE(2);
KobsFit=mdl.Coefficients.Estimate(1)+k5*xFit; % y for the fitted trace

figure(2)
plot(xFit,KobsFit)
hold on
scatter(xFit,Kobs)
xlabel('I/Ki/(1+S/KM+(I/Ki))')
ylabel('kobs')
hold off

end

```

Script 6. Inhibition kinetic data fitting to eq. 20

```
function [Kii,StErrKii,Vsdisp,k5r,StErrk5r,IFit,VsFit] =
InhibitionFittingPart3(Vs,I,E,S,kcat,KM,Ki,StErrKi,k5,StErrk5)

%-----Description-----
% This script is used following InhibitionFittingPart2. It fits the
inhibition parameters (Ki* and k-5) from inhibition features (vs) using eq.20
% Author: Zhe Ji

%-----Input Data-----
% Vs is a 1-column matrix of the initial rate of product formation as a
function of I
% I is a 1-column matrix containing the concentration of the inhibitor (uM)
% E is the concentration of the enzyme (uM)
% S is the concentration of the substrate (uM)
% kcat and KM are the Michaelis-Menten constants for the substrate
% Ki is the binding constant of the inhibitor, StErrKi is the corresponding
fitting error
% k5 is the rate constant for forming E-AVB, , StErrk5 is the corresponding
fitting error

%-----Output Data-----
% Kii is the binding constant of the inhibitor for both non-covalent and
covalent binding (Ki*), StErrKii is the corresponding fitting error
% Vsdisp is a 1-column matrix of a displacement parameter that adjusts the
absolte final slope
% k5r is the rate constant for the reverse reaction of forming E-AVB, ,
StErrk5r is the corresponding fitting error
% IFit is a 1-column matrix of x for the fitted trace of eq. 20
% VsFit is a 1-column matrix of y for the fitted trace of eq. 20

%-----Main-----

vmax=kcat*E;

%-----Fit Ki* from vs using eq. 20-----
function output=ModFun(beta,I)
    output=zeros(length(I),1);
    d=beta(2);
    for i=1:length(I)
        output(i)=vmax*S/KM/(1+I(i)/beta(1)+S/KM)+d; % eq. 20
    end
end

fun=@ModFun;
beta0=[0.0001,0]; % make guess for Ki* and Vsdisp
options=statset('FunValCheck','off');
[beta,R,J,CovB]=nlinfit(I,Vs,fun,beta0,options);
Kii=beta(1);
Vsdisp=beta(2);
StErr=(sqrt(diag(CovB)));
StErrKii=StErr(1);
```

```

IFit= (min(I):(max(I)-min(I))/100:max(I)).'; % x for the fitted trace
VsFit=zeros(length(IFit),1); % y for the fitted trace
for i=1:length(IFit)
    VsFit(i)=vmax*S/KM/(1+IFit(i)/Kii+S/KM)+Vsdisp;
end

figure(1)
plot(IFit,VsFit)
hold on
scatter(I,Vs)
xlabel('[Inhibitor] (uM)')
ylabel('vs (s-1)')
hold off

%-----Fit k5r from Ki, Ki*, and k5-----
k5r=Kii*k5/(Ki-Kii);
StErrk5r=
k5r*((StErrkii/Kii)^2+(StErrk5/k5)^2+(StErrKi(1)^2+StErrKii^2)/((Ki-
Kii)^2))^0.5;

end

```

Script 7. Simulation of Inhibition from kinetic parameters

```
function [t,P,V0,Vs,Kobs] = InhibitionSimulation(E,S,KM,kcat,I,Ki,k5,k5r)

%-----Description-----
% This script simulates the inhibition data (P) and features (v0, vs, and
kobs) from the kinetic parameters (Ki, k5, k-5)
% Author: Zhe Ji

%-----Input Data-----
% E is a 1-column matrix containing the concentration of the enzyme (uM) for
each experiment
% S is the value of substrate concentration (uM)
% KM (uM) and kcat (s-1) are the Michaelis-Menten constants for the substrate
% I is a 1-column matrix containing the concentration of the inhibitor (uM)
for each experiment
% Ki is the binding constant of the inhibitor for non-covalent binding
% k5 is the rate constant for forming E-AVB
% k5r is the rate constant for the reverse reaction of E-AVB formation (k-5)

%-----Output Data-----
% t is a 1-column matrix of time (s)
% P is a x-column matrix of product concentration (uM) as a function of time
and I, x= number of I
% V0 is a 1-column matrix of the initial rate of product formation as a
function of I
% Vs is a 1-column matrix of the final rate of product formation as a
function of I
% Kobs is a 1-column matrix of the apparent first order rate constant for
forming E-AVB as a function of I

%-----Main-----

t=0:0.1:250; % the range of time
P=[];
V0=[];
Vs=[];
Kobs=[];

for num = 1:length(I)
i=I(num);
V=E(num)*kcat; %Vmax
v0=V*S/(KM*(1+i/Ki)+S);
Kii=Ki*k5r/(k5+k5r);
vs=V*S/(KM*(1+i/Kii)+S);
kobs=k5r+k5*(i/Ki/(1+S/KM+i/Ki));
p=vs*t+(v0-vs)*(1-exp(-kobs*t))/kobs;
P=[P;p];
V0=[V0;v0];
Vs=[Vs;vs];
Kobs=[Kobs;kobs];
end

legendcell=strcat('I=',string(num2cell(I)));
```

```
figure(1)
plot(t,P)
xlabel('Time (sec)')
ylabel('[Product] (uM)')
legend(legendcell)

figure(2)
plot(I,V0./E.*E(1))
xlabel('[Inhibitor] (uM)')
ylabel('V0 (uM s-1)')

figure(3)
plot(I,Vs./E.*E(1))
xlabel('[Inhibitor] (uM)')
ylabel('Vs (uM s-1)')

figure(4)
plot(I,Kobs)
xlabel('[Inhibitor] (uM)')
ylabel('kobs (s-1)')

end
```

References

- 1 Deschuyteneer, G.; Garcia, S.; Michiels, B.; Baudoux, B.; Degand, H.; Morsomme, P.; Soumillion, P. Intein-Mediated Cyclization of Randomized Peptides in the Periplasm of *Escherichia coli* and Their Extracellular Secretion. *ACS Chem. Biol.* **2010**, *5*, 691-700.
- 2 Mathonet, P.; Deherve, J.; Soumillion, P.; Fastrez, J. Active TEM-1 Beta-Lactamase Mutants with Random Peptides Inserted in Three Contiguous Surface Loops. *Protein Sci.* **2006**, *15*, 2323-2334.
- 3 Schneider, S. H.; Kozuch, J.; Boxer, S. G. The Interplay of Electrostatics and Chemical Positioning in the Evolution of Antibiotic Resistance in TEM Beta-Lactamases. *ACS Central. Sci.* **2021**, *7*, 1996-2008.
- 4 Guo, J. T.; Wang, J. Y.; Anderson, J. C.; Schultz, P. G. Addition of an Alpha-Hydroxy Acid to the Genetic Code of Bacteria. *Angew. Chem. Int. Ed.* **2008**, *47*, 722-725.
- 5 Brown, N. G.; Pennington, J. M.; Huang, W.; Ayvaz, T.; Palzkill, T. Multiple Global Suppressors of Protein Stability Defects Facilitate the Evolution of Extended-Spectrum TEM Beta-Lactamases. *J. Mol. Biol.* **2010**, *404*, 832-846.
- 6 Kabsch, W. XDS. *Acta Crystallogr. D Biol. Crystallogr.* **2010**, *66*, 125-132.
- 7 Adams, P. D.; Afonine, P. V.; Bunkoczi, G.; Chen, V. B.; Davis, I. W.; Echols, N.; Headd, J. J.; Hung, L. W.; Kapral, G. J.; Grosse-Kunstleve, R. W.; McCoy, A. J.; Moriarty, N. W.; Oeffner, R.; Read, R. J.; Richardson, D. C.; Richardson, J. S.; Terwilliger, T. C.; Zwart, P. H. PHENIX: A Comprehensive Python-Based System for Macromolecular Structure Solution. *Acta Crystallogr. D Biol. Crystallogr.* **2010**, *66*, 213-221.
- 8 Wang, X. J.; Minasov, G.; Shoichet, B. K. Evolution of An Antibiotic Resistance Enzyme Constrained by Stability and Activity Trade-Offs. *J. Mol. Biol.* **2002**, *320*, 85-95.
- 9 Emsley, P.; Cowtan, K. Coot: Model-Building Tools for Molecular Graphics. *Acta Crystallogr. D Biol. Crystallogr.* **2004**, *60*, 2126-2132.
- 10 Ogg, R. J.; Kingsley, P. B.; Taylor, J. S. WET, a T1- and B1-Insensitive Water-Suppression Method for in vivo Localized ¹H NMR Spectroscopy. *J. Magn. Reson. B* **1994**, *104*, 1-10.
- 11 Hwang, Y. S.; Gu, J.-Q.; Jain, A.; Garad, S.; Sizemore, J. P. Crystalline Form of a β -Lactamase Inhibitor. **2014**, *US9120795B2*.
- 12 Abe, T.; Okue, M.; Sakamaki, Y. Optically Active Diazabicyclooctane Derivatives and Process for Preparing the Same. **2011**, *US2012016533A1*.
- 13 Wang, T.; Du, L. D.; Wan, D. J.; Li, X.; Chen, X. Z.; Wu, G. F. Use of Lipase Catalytic Resolution in the Preparation of Ethyl (2S,5R)-5-((Benzyloxy)amino)piperidine-2-carboxylate, a Key Intermediate of the Beta-Lactamase Inhibitor Avibactam. *Org. Process Res. Dev.* **2018**, *22*, 1738-1744.
- 14 Kozuch, J.; Schneider, S. H.; Zheng, C.; Ji, Z.; Bradshaw, R. T.; Boxer, S. G. Testing the Limitations of MD-Based Local Electric Fields Using the Vibrational Stark Effect in Solution: Penicillin G as a Test Case. *J. Phys. Chem. B* **2021**, *125*, 4415-4427.
- 15 Fried, S. D.; Boxer, S. G. Evaluation of the Energetics of the Concerted Acid-Base Mechanism in Enzymatic Catalysis: the Case of Ketosteroid Isomerase. *J. Phys. Chem. B* **2012**, *116*, 690-697.
- 16 Fried, S. D.; Bagchi, S.; Boxer, S. G. Measuring Electrostatic Fields in Both Hydrogen-Bonding and Non-Hydrogen-Bonding Environments Using Carbonyl Vibrational Probes. *J. Am. Chem. Soc.* **2013**, *135*, 11181-11192.

- 17 Zheng, C.; Mao, Y. Z.; Kozuch, J.; Atsango, A.; Ji, Z.; Markland, T. E.; Boxer, S. G. A Two-Directional Vibrational Probe Reveals Different Electric Field Orientations in Solution and an Enzyme Active Site. *Nat. Chem.* **2022**, *14*, 891-897.
- 18 Frisch, M.; Trucks, G.; Schlegel, H.; Scuseria, G.; Robb, M.; Cheeseman, J.; Scalmani, G.; Barone, V.; Petersson, G.; Nakatsuji, H. Gaussian, Inc., Wallingford CT, 2016.
- 19 Case, D. A.; Betz, R. M.; Cerutti, D. S.; I, T. E. C.; Darden, T. A.; Duke, R. E. AMBER 2016, University of California, San Francisco.
- 20 Caleman, C.; van Maaren, P. J.; Hong, M. Y.; Hub, J. S.; Costa, L. T.; van der Spoel, D. Force Field Benchmark of Organic Liquids: Density, Enthalpy of Vaporization, Heat Capacities, Surface Tension, Isothermal Compressibility, Volumetric Expansion Coefficient, and Dielectric Constant. *J. Chem. Theory Comput.* **2012**, *8*, 61-74.
- 21 Hess, B.; Kutzner, C.; van der Spoel, D.; Lindahl, E. GROMACS 4: Algorithms for Highly Efficient, Load-Balanced, and Scalable Molecular Simulation. *J. Chem. Theory Comput.* **2008**, *4*, 435-447.
- 22 Berendsen, H. J. C.; Postma, J. P. M.; Vangunsteren, W. F.; Dinola, A.; Haak, J. R. Molecular-Dynamics with Coupling to an External Bath. *J. Chem. Phys.* **1984**, *81*, 3684-3690.
- 23 Parrinello, M.; Rahman, A. Polymorphic Transitions in Single Crystals: a New Molecular Dynamics Method. *J. Appl. Phys.* **1981**, *52*, 7182-7190.
- 24 Boxer, S. G. Stark Realities. *J. Phys. Chem. B* **2009**, *113*, 2972-2983.
- 25 Andrews, S. S.; Boxer, S. G. Vibrational Stark Effects of Nitriles I. Methods and Experimental Results. *J. Phys. Chem. A* **2000**, *104*, 11853-11863.
- 26 Andrews, S. S.; Boxer, S. G. A Liquid Nitrogen Immersion Cryostat for Optical Measurements. *Rev. Sci. Instrum.* **2000**, *71*, 3567-3569.
- 27 Kozuch, J.; Schneider, S. H.; Boxer, S. G. Biosynthetic Incorporation of Site-Specific Isotopes in Beta-Lactam Antibiotics Enables Biophysical Studies. *ACS Chem. Biol.* **2020**, *15*, 1148-1153.
- 28 Jain, V.; Biesinger, M. C.; Linford, M. R. The Gaussian-Lorentzian Sum, Product, and Convolution (Voigt) Functions in the Context of Peak Fitting X-Ray Photoelectron Spectroscopy (XPS) Narrow Scans. *Appl. Surf. Sci.* **2018**, *447*, 548-553.
- 29 Schrödinger release 2022-2: Maestro, Schrödinger, LLC, New York, NY, 2021.
- 30 Alkema, W. B.; Hensgens, C. M.; Kroezinga, E. H.; de Vries, E.; Floris, R.; van der Laan, J. M.; Dijkstra, B. W.; Janssen, D. B. Characterization of the Beta-Lactam Binding Site of Penicillin Acylase of Escherichia coli by Structural and Site-Directed Mutagenesis Studies. *Protein Eng.* **2000**, *13*, 857-863.
- 31 Lu, C.; Wu, C. J.; Ghoreishi, D.; Chen, W.; Wang, L. L.; Damm, W.; Ross, G. A.; Dahlgren, M. K.; Russell, E.; Von Bargen, C. D.; Abel, R.; Friesner, R. A.; Harder, E. D. OPLS4: Improving Force Field Accuracy on Challenging Regimes of Chemical Space. *J. Chem. Theory Comput.* **2021**, *17*, 4291-4300.
- 32 Rackers, J. A.; Wang, Z.; Lu, C.; Laury, M. L.; Lagardere, L.; Schnieders, M. J.; Piquemal, J. P.; Ren, P. Y.; Ponder, J. W. Tinker 8: Software Tools for Molecular Design. *J. Chem. Theory Comput.* **2018**, *14*, 5273-5289.
- 33 Shi, Y.; Xia, Z.; Zhang, J. J.; Best, R.; Wu, C. J.; Ponder, J. W.; Ren, P. Y. Polarizable Atomic Multipole-Based AMOEBA Force Field for Proteins. *J. Chem. Theory Comput.* **2013**, *9*, 4046-4063.

- 34 Zhang, C. S.; Lu, C.; Jing, Z. F.; Wu, C. J.; Piquemal, J. P.; Ponder, J. W.; Ren, P. Y. AMOEBA Polarizable Atomic Multipole Force Field for Nucleic Acids. *J. Chem. Theory Comput.* **2018**, *14*, 2084-2108.
- 35 Walker, B.; Liu, C. W.; Wait, E.; Ren, P. Y. Automation of AMOEBA Polarizable Force Field for Small Molecules: Poltype 2. *J. Comput. Chem.* **2022**, *43*, 1530-1542.
- 36 Bezerra, R. M. F.; Dias, A. A. Utilization of Integrated Michaelis-Menten Equation to Determine Kinetic Constants. *Biochem. Mol. Biol. Edu.* **2007**, *35*, 145-150.
- 37 Golcnik, M. Exact and Approximate Solutions for the Decades-Old Michaelis-Menten Equation: Progress-Curve Analysis through Integrated Rate Equations. *Biochem. Mol. Biol. Edu.* **2011**, *39*, 117-125.
- 38 Paar, M.; Schrabmair, W.; Mairold, M.; Oetl, K.; Reibnegger, G. Global Regression Using the Explicit Solution of Michaelis-Menten Kinetics Employing Lambert's W Function: High Robustness of Parameter Estimates. *ChemistrySelect* **2019**, *4*, 1903-1908.
- 39 Banerjee, S.; Pieper, U.; Kapadia, G.; Pannell, L. K.; Herzberg, O. Role of the Omega-Loop in the Activity, Substrate Specificity, and Structure of Class A Beta-Lactamase. *Biochemistry* **1998**, *37*, 3286-3296.
- 40 Saves, I.; Burlletschiltz, O.; Maveyraud, L.; Samama, J. P.; Prome, J. C.; Masson, J. M. Mass-Spectral Kinetic-Study of Acylation and Deacylation During the Hydrolysis of Penicillins and Cefotaxime by Beta-Lactamase TEM-1 and the G238S Mutant. *Biochemistry* **1995**, *34*, 11660-11667.
- 41 Stachyra, T.; Péchereau, M.-C.; Bruneau, J.-M.; Claudon, M.; Frère, J.-M.; Miossec, C.; Coleman, K.; Black, M. T. Mechanistic Studies of the Inactivation of TEM-1 and P99 by NXL104, a Novel Non- β -Lactam β -Lactamase Inhibitor. *Antimicrob. Agents Chemother.* **2010**, *54*, 5132-5138.
- 42 Morrison, J. F.; Walsh, C. T. The Behavior and Significance of Slow-Binding Enzyme-Inhibitors. *Adv. Enzymol. Relat. Areas Mol. Biol.* **1988**, *61*, 201-301.
- 43 Ehmann, D. E.; Jahic, H.; Ross, P. L.; Gu, R. F.; Hu, J.; Kern, G.; Walkup, G. K.; Fisher, S. L. Avibactam is a Covalent, Reversible, Non- β -Lactam Beta-Lactamase Inhibitor. *Proc. Natl. Acad. Sci. USA* **2012**, *109*, 11663-11668.
- 44 Risso, V. A.; Gavira, J. A.; Mejia-Carmona, D. F.; Gaucher, E. A.; Sanchez-Ruiz, J. M. Hyperstability and Substrate Promiscuity in Laboratory Resurrections of Precambrian Beta-Lactamases. *J. Am. Chem. Soc.* **2013**, *135*, 10580-10580.
- 45 Weaver, J. B.; Kozuch, J.; Kirsh, J. M.; Boxer, S. G. Nitrile Infrared Intensities Characterize Electric Fields and Hydrogen Bonding in Protic, Aprotic, and Protein Environments. *J. Am. Chem. Soc.* **2022**, *144*, 7562-7567.
- 46 Pemberton, O. A.; Noor, R. E.; Kumar, M. V. V.; Sanishvili, R.; Kemp, M. T.; Kearns, F. L.; Woodcock, H. L.; Gelis, I.; Chen, Y. Mechanism of Proton Transfer in Class A β -Lactamase Catalysis and Inhibition by Avibactam. *Proc. Natl. Acad. Sci. USA* **2020**, *117*, 5818-5825.
- 47 Bender, A. T.; Gardberg, A.; Pereira, A.; Johnson, T.; Wu, Y.; Grenningloh, R.; Head, J.; Morandi, F.; Haselmayer, P.; Liu-Bujalski, L. Ability of Bruton's Tyrosine Kinase Inhibitors to Sequester Y551 and Prevent Phosphorylation Determines Potency for Inhibition of Fc Ceceptor but Not B-Cell Receptor Signaling. *Mol. Pharmacol.* **2017**, *91*, 208-219.
- 48 Canon, J.; Rex, K.; Saiki, A. Y.; Mohr, C.; Cooke, K.; Bagal, D.; Gaida, K.; Holt, T.; Knutson, C. G.; Koppada, N.; Lanman, B. A.; Werner, J.; Rapaport, A. S.; San Miguel,

- T.; Ortiz, R.; Osgood, T.; Sun, J. R.; Zhu, X.; McCarter, J. D.; Volak, L. P.; Houk, B. E.; Fakhri, M. G.; O'Neil, B. H.; Price, T. J.; Falchook, G. S.; Desai, J.; Kuo, J.; Govindan, R.; Hong, D. S.; Ouyang, W.; Henary, H.; Arvedson, T.; Cee, V. J.; Lipford, J. R. The Clinical KRAS(G12C) Inhibitor AMG 510 Drives Anti-Tumour Immunity. *Nature* **2019**, *575*, 217-223.
- 49 Metzler, W. J.; Yanchunas, J.; Weigelt, C.; Kish, K.; Klei, H. E.; Xie, D.; Zhang, Y.; Corbett, M.; Tamura, J. K.; He, B.; Hamann, L. G.; Kirby, M. S. Involvement of DPP-IV Catalytic Residues in Enzyme-Saxagliptin Complex Formation. *Protein Sci.* **2008**, *17*, 240-250.
- 50 Romano, K. P.; Ali, A.; Aydin, C.; Soumana, D.; Ozen, A.; Deveau, L. M.; Silver, C.; Cao, H.; Newton, A.; Petropoulos, C. J.; Huang, W.; Schiffer, C. A. The Molecular Basis of Drug Resistance Against Hepatitis C Virus NS3/4A Protease Inhibitors. *PLoS Pathog.* **2012**, *8*, e1002832.